

# RESEARCH DEPARTMENT



GPO PRICE \$ \_\_\_\_\_

CFSTI PRICE(S) \$ \_\_\_\_\_

Hard copy (HC) \$ 3.00

Microfiche (MF) .65

ff 653 July 65

## MOBIL OIL CORPORATION

FACILITY FORM 602

N 67-27424

(ACCESSION NUMBER)

120

(PAGES)

CR54447

(NASA CR OR TMX OR AD NUMBER)

(THRU)

1  
(COPY)

(CATEGORY)

Final Report  
NEUTRON DIE-AWAY EXPERIMENT FOR  
LUNAR AND PLANETARY SURFACE ANALYSIS

July 26, 1966 through March 26, 1967

Prepared by

W. R. Mills, Jr.

and

W. W. Givens

of

3, Mobil Oil Corporation  
Field Research Laboratory  
3600 Duncanville Road  
Dallas, Texas 75211

for

Dr. Martin J. Swetnik  
Code SL

National Aeronautics and Space Administration  
Washington, D.C. 20546

1. 10-871-C-Rec. (9-66)

April 26, 1967

FOREWARD

This is the final report under contract No. NASW-1435, entitled "Neutron Die-Away Experiment For Lunar and Planetary Surface Analysis", covering the contract period July 26, 1966 to March 26, 1967.

The following personnel have contributed to the work described in this report: W. R. Mills, Jr., W. W. Givens and L. S. Allen, principal investigators, and J. B. Hickman and J. G. Baker.

Respectfully submitted,

*W. R. Mills, Jr.*

W. R. Mills, Jr.  
Research Associate

*W. W. Givens*

W. W. Givens  
Senior Research Physicist

Approved by:

*R. L. Caldwell*

R. L. Caldwell  
Principal Administrator

## TABLE OF CONTENTS

	<u>Page</u>
FOREWARD	
I. GENERAL INTRODUCTION	1
II. THE NEUTRON DIE-AWAY METHOD	3
III. INSTRUMENTATION FOR DIE-AWAY EXPERIMENTS	13
IV. EXPERIMENTAL DETERMINATION OF NECESSARY MODEL SIZES	15
V. DATA ANALYSIS METHODS	26
VI. PHYSICAL AND CHEMICAL PROPERTIES OF ROCK MODELS	31
VII. RESULTS OF OPTIMUM THERMAL DIE-AWAY MEASUREMENTS	35
VIII. RESULTS OF EPITHERMAL DIE-AWAY MEASUREMENTS	41
IX. LAYERING STUDIES	46
X. MEASUREMENTS ON A SURFACE IRREGULARITY	49
XI. CYCLIC ACTIVATION RESULTS	51
XII. VARIOUS PROBLEMS	56
REFERENCES	
APPENDIX	
TABLES	
FIGURES	

## 1. GENERAL INTRODUCTION

The spectacular photographic successes of Surveyor I and the Lunar Orbiters have given man some unique views of the moon. A similar statement may be made for the Mariner IV flight to Mars. In spite of these successes, very little has been learned about the probable physical or chemical properties of the moon and Mars. Our ignorance is particularly glaring for depths below the surface of greater than a few millimeters. Some scientific questions concerning the moon will be answered when returned samples are available at the successful conclusion of a future manned Apollo mission. It is also of scientific interest to make measurements in situ both before and following the Apollo series. Knowledge of the Martian surface on a small scale should probably be contemplated at present only in terms of unmanned, soft-lander missions.

Several different techniques have been proposed for measuring one or another characteristic of a remote surface. Many of these were discussed and reviewed at the recent meeting at the Goddard Space Flight Center, 3-5 October 1966, on Analytical Systems for Lunar Surface Analysis. Among these are x-ray spectroscopy using alpha-, beta-, or gamma-ray sources to excite the x-rays, alpha scattering, mass spectrometry, and x-ray diffraction. These methods have relatively shallow depth of investigation, varying from a few hundredths of a mm to at most a few cm. They exhibit varying degrees of specificity to individual elements, and each method is worthy of consideration to be incorporated into future soft-lander missions.

In contrast to and complementing the above methods, a neutron analysis experiment has been proposed by Caldwell et al.<sup>1</sup> This experiment would employ a combination of four neutron methods. The use of a combination of neutron reactions for analysis has been previously suggested by Monaghan et al.<sup>2</sup>, and by Trombka and Metzger.<sup>3</sup> The four methods contemplated were inelastic (prompt) gamma-ray, capture gamma-ray, and

activation gamma-ray spectral measurements, and neutron die-away. The paper of Caldwell et al<sup>1</sup> extended the work in the two earlier references by virtue of a detailed consideration of the capabilities of the die-away method and in the suggestion that cyclic (i.e. repetitive) activation was worthy of consideration as an alternative and complement to normal activation.

The present report is concerned with the results of feasibility studies on the neutron die-away method. The studies have involved measurements under a variety of conditions of the die-away of neutrons and gamma rays as produced by a pulsed-neutron source and as measured by suitable detectors. In each case, source and detector were placed on the surface of one of several rock models which are effectively semi-infinite. From the results of the feasibility studies discussed in detail in the succeeding sections, we have reached the following tentative conclusions:

- 1) From either a gamma-ray or thermal-neutron die-away curve for a given geometrical configuration, the macroscopic absorption cross section  $\Sigma_a$  may be determined. If rock type is known from auxiliary data, then rock density  $\rho$  may be deduced, if  $\rho$  is known, rock type may be deduced.
- 2) Epithermal die-away curves respond primarily to hydrogen and they show a proper and very sensitive response to hydrogen in the range of a few hundredths to a few tenths of a weight per cent.
- 3) Gamma-ray and thermal-neutron die-away curves reflect a relatively deep (up to about 2 ft) material averaging capability, resulting in the possibility of obtaining some information about the dependence of material properties as a function of depth.
- 4) From some brief cyclic activation studies, it appears that O, Si, and a combination of Al and Mg can be detected with a low-output neutron source.

## 11. THE NEUTRON DIE-AWAY METHOD

We begin this section with a qualitative discussion of the neutron die-away method. Figure 1 shows a timing diagram for the combination neutron experiment which is useful for this discussion. As may be seen from Fig. 1, a prime requirement for such an experiment is a source of fast neutrons which can be operated in a pulsed mode. Short bursts of fast neutrons are separated by a relatively long time during which the source is off. The process is repeated at rates of the order of hundreds of bursts per second. The prompt gamma rays from inelastic scattering are coincident in time with the fast neutron bursts. The thermalized neutrons, and the gamma rays resulting from neutron capture by nuclei, have a different time behavior. This behavior may be roughly thought of as the result of passing the fast neutron burst shape through an RC filter, with the RC time constant being a function of material properties and of the geometrical configuration of the source and detector. The shape of the decaying portion of the thermal neutron or capture gamma-ray time distribution is of paramount importance in the die-away technique. In particular if the die-away is an exponential  $e^{-\lambda t}$ , the decay constant  $\lambda$  (analogous to  $\frac{1}{RC}$ ) is obtained from the slope of the decay curve plotted semi-logarithmically. The reciprocal of  $\lambda$  is called the mean lifetime  $\tau$ .

If one desires to lay a firm theoretical groundwork for the die-away method, he is faced with a very formidable task. The quantity which must be calculated is the vector neutron density  $N(\vec{r}, \vec{v}, t)$ . This is defined such that  $N d\vec{r} d\vec{v}$  is the number of neutrons in the volume  $\vec{r}$  to  $\vec{r} + d\vec{r}$  and in the velocity range  $\vec{v}$  to  $\vec{v} + d\vec{v}$  at time  $t$ . The vector neutron density changes in  $\vec{r}, \vec{v}, t$  phase space due to nuclear interactions and according to well-defined statistical laws.  $N(\vec{r}, \vec{v}, t)$  satisfies an integro-differential equation called the Boltzmann transport equation. It is much like the equation governing phenomena of gas

molecules, but due to the extremely low probability of neutron-neutron interactions the neutron transport equation is linear in  $N$ . The Boltzmann equation is virtually unsolvable in practice, and approximate theories must be used if one is to obtain numbers with which to compare experimental results.

The subject of theoretical approximations to the Boltzmann equation can and does fill several books today. Since this report is aimed in a very specific direction, it would not be proper to even briefly review the choices which are available and appropriate to some particular problem. Instead we will use one of the approximations, without making any real attempt to justify it, to obtain a solution to the neutron die-away problem for a semi-infinite medium. It must be borne in mind that we have not tried to use the best theory available. Instead, a compromise was sought between physical reality and tractability of solution.

A simple but reasonably good theory of neutron and gamma-ray die-away for a semi-infinite medium is useful in several ways. Calculated die-away curves may be compared with experimental curves to obtain an indication of how adequate the particular theory is. If the theory is good, one may be able to use the expressions in some data fitting scheme to directly obtain best values of material neutron parameters. A theory may allow prediction of experimental results for situations which are difficult to simulate in the laboratory. And finally, the theoretical results to be described here were used to estimate how big our surface models must be in order to appear effectively semi-infinite to within any given amount of error.

We have used a combination of two approximate theories in our study.\* These are steady-state age theory and time-dependent one-energy-

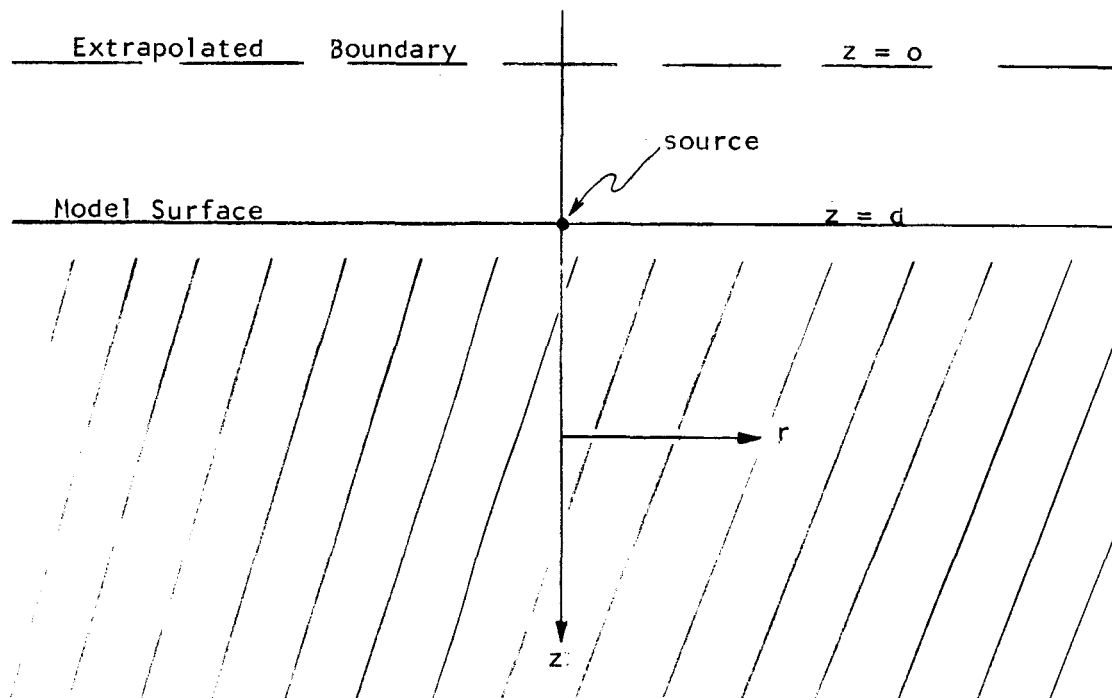
---

\*For detailed discussions of neutron transport theory and the approximations to it, the reader is referred to the book by Beckurts and Wirtz<sup>4</sup> and Chap. 6 of the book by Sneddon.<sup>5</sup>



group diffusion theory. We take the neutron slowing-down density which comes from age theory and use this as the distribution of thermal source neutrons at time zero. This procedure appears to be justified for two reasons. First, age theory should be adequate in describing the slowing-down process in rocks which contain very small amounts of hydrogen. The assumption of continuous energy degradation during slowing down, a central assumption in age theory, is a very poor one for hydrogen. Second, since a burst of  $10 \mu\text{sec}$  would prevent the thermal neutron distribution from even approaching spatial saturation while the epithermal neutron or slowing-down distribution would presumably be saturated (due to the short lifetime of the epithermal neutrons), steady-state age theory should furnish an adequate initial distribution of thermal source neutrons at  $t = 0$ .

The geometry for the die-away experiment is shown below:



The source is placed on the surface. The origin of the cylindrical coordinate system is taken at the extrapolated surface where both the slowing-down and the thermal neutron density are assumed to go to zero. The age equation to be solved is

$$\nabla^2 q + S \frac{\delta(r)\delta(z-d)\delta(\theta)}{2\pi r} = \frac{\partial q}{\partial \theta} \quad (1)$$

where  $q$  is the slowing-down density,  $S$  is the source strength, and  $\theta$  is the Fermi or symbolic age. Boundary conditions on  $q$  are

$$\lim_{(r, z \rightarrow \infty)} q(r, z, \theta) = \lim_{(r \rightarrow \infty)} \frac{\partial q}{\partial r} = \lim_{(z \rightarrow \infty)} \frac{\partial q}{\partial z} = 0 \quad (2)$$

$$q(r, 0, \theta) = 0 \quad (3)$$

$$q(r, z, 0) = 0 \quad (4)$$

The solution to Eq.(1) satisfying these conditions is used as an initial condition in the time-dependent thermal diffusion equation

$$v D \nabla^2 n - v \Sigma_a n = \frac{\partial n}{\partial t} \quad (5)$$

where  $n$  is the thermal neutron density,  $D$  is the thermal diffusion coefficient,  $v$  is the velocity of thermal neutrons, and  $\Sigma_a$  is the macroscopic absorption cross section. Conditions on  $n$  are

$$\lim_{r, z \rightarrow \infty} n(r, z, t) = \lim_{r \rightarrow \infty} \frac{\partial n}{\partial r} = \lim_{z \rightarrow \infty} \frac{\partial n}{\partial z} = 0 \quad (6)$$

$$n(r,0,t) = 0 \quad (7)$$

$$n(r,z,0) = q(r,z,\theta). \quad (8)$$

We assume that  $\theta$  is the age to the upper limit of the thermal energy range. It is shown in the Appendix that the solution to the system of equations (1) through (8) is

$$n(r,z,t) = \frac{Se^{-\left[\frac{v\Sigma_a t + \frac{r^2}{4(\theta+vDt)}}{4\pi(\theta+vDt)}\right]^{3/2}}}{\left\{e^{-\frac{(z-d)^2}{4(\theta+vDt)}} - e^{-\frac{(z+d)^2}{4(\theta+vDt)}}\right\}} \quad (9)$$

Fig. 2 shows two typical die-away curves calculated from Eq.(9). We have taken fixed values for  $\theta$  and  $D$  which would correspond roughly to the case of crushed granite rock with 0.5-weight percent  $H_2O$ . These two parameters do not change greatly with rock type, so they could also be assumed for crushed basalt for the purposes of this semi-quantitative calculation. The values of  $\Sigma_a$  of 0.005 and 0.010  $cm^{-1}$  correspond approximately to crushed granite and basalt, respectively. Values of  $r$  and  $z$  of 25 and 4.7 cm, respectively, are for a detector located on the model surface and 25 cm from the source. The abscissa, which is the time axis, is given as channel number as if the curves had been obtained with a multichannel time analyzer. The scale is 16  $\mu sec/channel$ .

The curves in Fig. 2 reveal several interesting features. The rates of decay are quite different, showing strong sensitivity of Eq.(9) to the values of  $\Sigma_a$ . If this were not true, the die-away method would obviously hold little promise from the start. Both curves are nearly linear on the semi-log plot which would imply that the decay is almost purely exponential. From the form of Eq.(9), one is thus tempted to infer that

$$n(r,z,t) \approx e^{-v\Sigma_a t}. \quad (10)$$

This is not the case, however, as may be seen from the following argument. Assuming that the curves are asymptotically exponential, effective values of  $\Sigma_a$  can be obtained from the slope of each curve. These values are 0.0078 and 0.0127  $\text{cm}^{-1}$ , instead of the correct values of 0.005 and 0.010. The apparently larger values of  $\Sigma_a$  deduced this way reflect the physical fact that neutrons die-away not only due to capture, but also due to leakage out of the surface. This leakage effect is tied up in the part of the expression in Eq.(9) which multiplies  $e^{-v\Sigma_a t}$ . To the extent that Eq.(9) is correct, we might write that

$$n(r,z,t) \approx e^{-v(\Sigma_a + \Sigma_\ell)t} \quad (11)$$

where  $\Sigma_\ell$  is a fictitious effective cross section for leakage. Using the foregoing sets of numbers, we find that  $\Sigma_\ell = 0.0028$  and  $0.0027 \text{ cm}^{-1}$  for granite and basalt. These two should agree since the parameters affecting  $\Sigma_\ell$  are  $\theta$  and  $D$  which have been assumed equal for granite and basalt.

Fig. 3 shows plots of the neutron density versus depth, as predicted by Eq.(9). The physical parameters are the same as for Fig. 2. No values of  $\Sigma_a$  or  $r$  are given, as these are contained in factors which simply scale the neutron density insofar as  $z$ -dependence is concerned. What is plotted in Fig. 3 is the function

$$g(z) = e^{-\frac{(z-d)^2}{4(\theta+vDt)}} - e^{-\frac{(z+d)^2}{4(\theta+vDt)}}.$$

The two curves shown are for 0 and 1000  $\mu\text{sec}$  delay times. Note that the value of  $z$  corresponding to maximum density shifts from about 46 cm at  $t = 0$  to about 57 cm for  $t = 1000 \mu\text{sec}$ . Such a behavior reflects the gradual diffusion with time of the thermal neutrons deeper into the medium. The shape of either curve and the position of the maximum are in

qualitative agreement with the results obtained from a one-dimensional, steady-state, multi-group calculation carried out at the Illinois Institute of Technology Research Institute.<sup>6</sup>

Having discussed theoretical predictions for thermal neutron die-away, we turn to the same problem for capture gamma rays. Assume that a gamma-ray detector, which is biased so that the only gamma rays above some threshold energy  $E$  can be counted, is located at  $(r_o, z_o)$ . The measured die-away will be proportional to  $n_Y(r_o, z_o, t)$ , where

$$n_Y(r_o, z_o, t) = \int n(r, z, t) \sum_i \sum_j \Sigma_{ai}(r, z) f_i(r, z, E_j) F(r, z, r_o, z_o; E_j) dV \quad (12)$$

and

$\Sigma_{ai}$  = space-dependent macroscopic absorption cross section for the  $i$ 'th type nucleus,

$f_i(r, z, E_j)$  = energy spectrum of monoenergetic capture gamma rays  $E_j$  produced from the  $i$ 'th type nucleus capturing a neutron at  $(r, z)$ ,

$F(r, z, r_o, z_o; E_j)$  = relative chance that a gamma ray of energy  $E_j$  which is produced at  $(r, z)$  will get counted by the detector at  $(r_o, z_o)$ .

In Eq. (12) the sum on  $i$  extends over the various nuclear species present, and the sum on  $j$  extends over the discrete capture gamma-ray spectrum characteristic of each nuclear type.

If  $n(r, z, t)$  is separable, i.e.

$$n(r, z, t) = R(r, z) T(t),$$

then we would have that

$$n_Y(r_o, z_o, t) = \text{constant} \times T(t),$$

and the die-away curves as measured by a neutron and a gamma-ray detector at a given location would be equal to within a multiplicative constant. In the case of a semi-infinite medium, if Eq.(9) is even qualitatively correct, we see from the above analysis that identical die-away curves would not be expected from the two types of detector.

The contrast between neutron and gamma-ray die-away curves is illustrated in the paper by Mills et al.<sup>7</sup> Figs. 4 and 5 of that paper compare the two types of die-away in a model consisting of a limestone lattice of 5% porosity with fresh water filling the lattice. A 7-in diameter hole runs through the model parallel to the lattice rods. Data are shown for fresh water and for 9% salt water filling the hole, with the detector in each case coaxial with the hole. The gamma-ray die-away curves for the two fluids are practically identical, whereas the neutron curves are quite different until a time delay of about 1500  $\mu$ sec, following which these curves become equal. This difference in neutron and gamma-ray die-away curves is obviously important and will be referred to subsequently in our discussions of the experimental results of the feasibility studies.

A form of Eq.(12) has been used to estimate what size mock model is needed in order to be effectively semi-infinite to within any given amount of error. We assume that  $\Sigma_{ai}(r,z)$  and  $f_i(r,z,E_j)$  are constant, and that  $F(r,z,r_o,z_o;E_j)$  is proportional to the solid angle at the detector. In neglecting gamma-ray attenuation due to scattering and absorption, we should obtain conservatively large estimates of model sizes. If the detector is assumed to be at some height  $h$  above the extrapolated surface and directly over the source ( $r_o = 0$ ,  $z_o = -h$ ), then apart from a multiplying constant the gamma-ray counting rate will be

$$n_Y = \int \frac{n(r,z,t)}{r^2 + (z+h)^2} dV \quad (13)$$

The limits of integration should be 0 to  $\infty$  on  $r$  and  $d$  to  $\infty$  on  $z$  for the semi-infinite case. We can approximately study the effects of finiteness by writing  $n_Y$  as

$$n_Y \approx \int_{z=d}^H \int_{r=0}^R \frac{n(r,z,t)}{r^2 + (z+h)^2} r dr dz \quad (14)$$

A parametric survey based on Eq.(14) was made. As  $H$  and  $R$  are increased,  $n_Y$  approaches the true semi-infinite value  $n_Y^{\infty}$ . Thus, for any value of the "effective semi-infiniteness" ratio  $n_Y/n_Y^{\infty}$ , we can determine model radius and height. Table 1 shows the results of calculations for a rock type which is basically  $\text{SiO}_2$ . The values of  $h$  and  $t$  were 40 cm and 500  $\mu\text{sec}$ . Three values of density were used. For each of these either  $R$  or  $H$  was set equal to a very large value, and the ratio  $n_Y/n_Y^{\infty}$  calculated as a function of the other variable. From graphs of the ratio, the values of  $R$  and  $H$  which are needed to yield a given value of the ratio may be determined. Table 1 shows the values of model diameter  $D$  and height  $H$  for values of  $n_Y/n_Y^{\infty}$  of 0.90, 0.95, 0.98, and 0.99. It should be emphasized here again that these results are probably in error on the conservatively large side.

The preceding analysis of thermal die-away can be extended to epithermal die-away by redefinition of the physical parameters. The symbolic age  $\theta$  becomes the age to the upper limit of the rather arbitrary epithermal energy range. The diffusion coefficient  $D$  and the velocity  $v$  assume average values over the epithermal range of energies. The thermal-neutron macroscopic absorption cross section  $\Sigma_a$  is replaced by the epithermal removal cross section  $\Sigma_R$  which includes removal of neutrons from the epithermal group by absorption and also by loss to the thermal group by additional slowing down to thermal energies. Practically all absorption cross sections vary as  $v^{-1}$ , therefore, the absorption processes in the epithermal range would

generally remove fewer neutrons than would moderating or slowing down processes. This would be particularly true if hydrogen was present. Since hydrogen dominates the slowing down process, the removal cross section should be very sensitive to the presence of water even in small quantities. Epithermal die-away should then be a very sensitive method for determining the presence of water in a rock matrix. Our epithermal measurements show this to be qualitatively correct and are discussed in a later section.



### III. INSTRUMENTATION FOR DIE-AWAY EXPERIMENTS

A necessary first task which had to be performed before actual die-away experiments could be carried out was the assembly of a suitable combination of fast neutron source, fast neutron attenuator, and either gamma-ray or neutron detector. A Van de Graaff generator is the most suitable source of 14-Mev neutrons because of its relative ease of operation, high reliability, and versatility. An additional consideration which is important for pulsed work is the capability of achieving rise and fall times on the production bursts of about 1  $\mu$ sec or less without any unusual equipment. As a simple calculation based on the results in Table I will show, suitable semi-infinite models would weigh several tons at least. The target tube and experimental area of our 0.5-Mev Van de Graaff are over a pit which is 8 feet deep and covered with thin aluminum flooring which cannot support such a weight. It was, therefore, necessary from the beginning that we work in an area remote from the Van de Graaff, and this dictated the use of a portable neutron source.

The source most convenient for us was a Philips Model 18600 neutron tube with associated controls and supplies. This pulsed source of 14-Mev neutrons has a wide range of burst widths (5  $\mu$ sec minimum) and repetition rates, with a maximum average output of  $10^7$  neutrons/sec. A drawing of the tube is shown in Fig. 4. The length of the grounded housing is 46 cm and its diameter is 7 cm. The large diameter (2.5 cm) high voltage cable prevents close placement of an attenuator and detector in a coaxial configuration at the high voltage end of the tube. Allowing for an attenuator length of 15 cm, the closest target-detector spacing obtainable at the low voltage end of the tube in a coaxial alignment is about 50 cm. Since spacings as close as 25 cm were desirable, we decided to use a "T" configuration with the neutron tube forming the bar and the attenuator and detector forming the stem.

The "T" configuration was used to make the die-away measurement discussed in the paper by Caldwell et al<sup>1</sup>. A problem which exists is that of detector disturbance due to x-rays produced at the low voltage end of the Philips tube, produced by electrons backstreaming in the accelerating field. The source of x-rays is outside the shadow of the fast neutron attenuator, so some extra shielding is required. Several tests were performed related to the x-ray effect. At a target potential of 100 kv, zero replenisher current, and zero ion probe voltage, a pulse height spectrum was obtained. This spectrum exhibits a shape characteristic of Bremsstrahlung radiation with a peak at about 60 kev. A series of runs was taken for different accelerating potentials, with zero replenisher current and probe voltage, and for varying thicknesses of Pb wrapped around the low voltage end of the Philips tube. For each run the area under the pulse height distribution was determined as a measure of the x-ray intensity. From these tests we determined that, for an accelerating potential of 125 kv, a Pb thickness of 5/16" is needed for complete shielding. As a matter of interest, during the above tests we found that the noise level of our detector-amplifier system was below 5 kev.

A second type of study carried out prior to settling on a final probe design for the die-away studies was connected with the choice of the material for the fast neutron attenuator. Pb and Cu were comparatively tested by placing the Philips tube, attenuator, and NaI crystal in the "T" configuration on a concrete surface. Die-away runs were taken under the following conditions: 5- $\mu$ sec beam burst, 400 pulses/sec, 16  $\mu$ sec/channel, 122-kev and 1.33-Mev energy biases, 30-min run time. The average background counts per channel were obtained from the data immediately preceding the burst. This may be seen in Fig. 9 which shows the die-away curve for the case of Cu and the 122-kev bias. This figure will be discussed in more detail in the next section. The average background was calculated from the raw data in

channels 2 through 21. In each case a true average background count per channel was subtracted from the observed average count during a pulsed run. The true background was obtained from runs identical to those described except that no neutrons were produced. For 122-kev bias the corrected counts were 571 and 744 counts/channel/30 min for Pb and Cu, respectively. The count for Cu is possibly greater than than for Pb due to annihilation radiation produced as a result of the  $\text{Cu}^{63}(\text{n}, \text{n})\text{Cu}^{62}$  (9.9 min) reaction. Even though we find that Pb is a better attenuator than Cu for die-away, the difference is not large and we chose to use Cu in our feasibility studies because it is probably preferred for the inelastic scattering part of the combination neutron experiment. However, we will have reason to reconsider the question of a suitable attenuator when the results of preliminary cyclic activation tests are discussed in a later section.

Following these preliminary experiments, a final probe was assembled in an aluminum housing. An exploded view is shown in Fig. 5. A meter stick is attached to the housing near a series of longitudinal slots through which a pointer protrudes when the detector is in the housing. This pointer is attached to the detector system and the position of the pointer along the meter stick gives a direct measurement of the target-detector spacing. An aluminum tripod, shown in Fig. 14, holds the probe in a vertical position when required. Unless otherwise specified, all gamma-ray die-away curves shown in this report were taken with a 3" x 3" NaI (Tl) scintillation crystal on an RCA 8054 photomultiplier in a Harshaw integral line assembly. Shielding from thermal neutrons was provided by a layer of  $\text{B}^{10}$  about  $380 \text{ mg/cm}^2$  thick around the crystal. The measured resolution for  $\text{Cs}^{137}$  gamma rays is 7.5%. All neutron die-away runs were obtained with a 10-atmosphere  $\text{He}^3$  proportional counter, made by Texas Nuclear Corp., of active dimensions 1" x 4".

Energy calibration for the gamma-ray spectrometer was set and frequently checked with  $\text{Co}^{57}$  (122 kev),  $\text{Cs}^{137}$  (662 kev),  $\text{Na}^{22}$  (510 kev and 1.28 Mev), and  $\text{Co}^{60}$  (1.17 and 1.33 Mev). Integral bias levels were determined by adjusting the size of pulses from a pulser fed into the amplifier so that the output pulse from the amplifier fell into the proper channel in the TMC pulse height analyzer, and then setting the integral discriminator to just cut that size of pulse off. With the  $\text{He}^3$  detector, optimum operating conditions were determined by running high voltage plateau curves using thermalized neutrons from a Pu-Be source.

During the feasibility studies reported here, it was not felt necessary to attempt an accurate measurement of the neutron output from the Philips generator for each run. Instead, the output was approximated each time according to the following scheme. The output for any given pulsed run depends on accelerating voltage, size of probe pulse, duty cycle, and target current. The output is not necessarily directly proportional to any of these. It was decided to adopt some standard generator conditions for the die-away studies for all but one of the parameters above, and vary that one to obtain suitable counting rates for each run. After trial and error, some of which will become apparent during the course of this report, the following standard conditions were adopted:

<u>PARAMETER</u>	<u>THERMAL DIE-AWAY</u>	<u>EPITHERMAL DIE-AWAY</u>
Probe pulse (v)	2000	2000
Burst length ( $\mu\text{sec}$ )	100	10
Period ( $\mu\text{sec}$ )	5000	2500
Target current ( $\mu\text{a}$ )	8	1

The accelerating voltage was variable from run to run. Using the above operating parameters, curves of output as a function of voltage were obtained by a silicon activation technique. Quartz discs of

1" dia. and 3/16" thickness were activated at a known distance from the target of the Philips tube in a "3-min bombard - 2-min wait - 5-min count" cycle. The  $\beta$  activity produced by the  $\text{Si}^{28}(\text{n},\text{p})\text{Al}^{28}$  (2.3 min) reaction in the quartz was counted in an end-window Geiger counter using a standard geometry. Calibration of neutrons/ $\beta$  count was obtained from an identical activation run carried out on our 0.5-Mev Van de Graaff which has an absolutely calibrated  $\alpha$ -particle counter viewing the target.

Fig. 6 shows a block diagram of the basic electronic configuration used for the die-away measurements. Some variations from this system were used and these will be pointed out. The operating conditions for the Philips tube were controlled by a console separated from the tube by about 90 feet of cable. The integral mount NaI was plugged into a Victoreen Model PC-3 preamplifier and the signal from this was amplified and discriminated in a Victoreen Model 851A amplifier (DD2 type) and Model 851-25 single channel pulse-height analyzer shown as an integral discriminator in Fig. 6. For the  $\text{He}^3$  runs the PC-3 preamplifier was replaced by a Baird-Atomic Model 205 preamplifier which has pulse shaping more suitable for the slower  $\text{He}^3$  pulses. The discriminator pulses were fed into the Signal input of the TMC time analyzer which consists of a Model CN110 unit with a Model 211 Time-of-Flight plug-in. The time-zero pulse from the Philips pulse generator serves as the input to a phantastron delay generator whose output pulse is fed into the Trigger input of the 211 unit to initiate a time analysis cycle. For optimum die-away results we found it necessary to gate the PM tube off during the burst for the gamma-ray runs. This is achieved by applying a suitable signal to the focusing grid in the tube. The signal was generated in a PM-tube gating circuit triggered at zero time.

Fig. 7 shows a generalized timing diagram for the die-away experiments. Time zero trigger pulses are separated by a period P. Due to the nature of operation of the Philips tube, a built-in delay of 12  $\mu\text{sec}$  precedes the fast neutron burst of duration B. The photomultiplier tube is gated off at zero time and held off for a duration G. In all cases

$$G > 12 + B .$$

-18-

The trigger input pulse to the time analyzer is generated after a delay  $D$ . Total analysis time is  $A$ , which is the product of the channel width  $\Delta t$  and the number of channels used. For all die-away runs shown subsequently, values of the timing parameters will be given in the form  $(B, P, G, D, \Delta t)$ . We prefer to give channel width rather than total analysis time, since the former quantity is more useful.

#### IV. EXPERIMENTAL DETERMINATION OF NECESSARY MODEL SIZES

In order to carry out laboratory die-away measurements which are applicable to remote surface analysis on the moon or planets, it must be demonstrated that the physical model being used is effectively a semi-infinite surface, to within the accuracy of the method. There are at least two practical ways to determine experimentally how big the models must be. In the first, which might be called the incremental method, measurements are first made on a model which is known to be undersize. The size of the model is incrementally increased and the measurement repeated for each size. A suitable parameter is extracted from the data for each case and plotted against a second parameter related to the size. Whatever the shape of such a plot may be, the measured parameter must asymptotically approach the value for a semi-infinite medium. Thus, a model size may be determined when a choice is made of an acceptable discrepancy between the measured parameter and its asymptotic value. This procedure has the disadvantage of being rather tedious since the model is built up step by step.

The second method, and the one used in the die-away studies, might be called the traverse method. A model is constructed which is known to be oversize. Conservative estimates of the necessary size may be obtained from approximate calculations like those in Section II. A traverse is run on the surface along a line cutting the model in half. At each position along the traverse where the instrument is placed, a measurement is made and a mappable parameter is extracted from the data. When values of this parameter are plotted as a function of location along the traverse, one should observe a flat interior portion with deviations toward both ends of the plot. The existence of a flat region in the plot is evidence that the model is effectively semi-infinite. The length of the flat part compared to the lateral physical dimensions of the model gives an indication of the minimum size model required.

An oversize model should be made up of a material which is as free of hydrogen as possible. This is due to the fact that hydrogen tends to

make the spatial neutron distribution relatively narrow, resulting in an unfairly small sensitivity to the model edge. It was decided to use dry bricks as the building material for the model. These were readily available to us and could be easily stacked to form the desired size.

From data given in reference tables, we estimated that dry clay bricks would have a density somewhere between 1.4 and 2 gm/cm<sup>3</sup>. Since it is desirable to have the brick assembly on the safely large size, we assumed a density of 1.40. We used the results shown in Table 1 as a guide in determining how big to make the brick model. A value of  $n_Y/n_Y^{oo}$  of 0.95 was arbitrarily assumed, which gives a diameter of 320 cm and a height of 153 cm. Since we planned to assemble a parallelepiped rather than a cylinder, the lateral dimensions of the model would be about 320 cm. Thus, a brick parallelepiped, approximately 10 feet on each side by 5 feet high, should adequately represent our oversize surface model.

A parallelepiped of dry clay bricks was assembled which measured 116" x 116" x 65". Each brick was about 2.25" x 3.5" x 7.5" and the assembly contained some 13,950 bricks. The bricks, obtained from the Ferris Brick Company at Ferris, Texas, were removed from the kiln only a few hours before delivery to us by truck, thus assuring that the bricks were dry. The parallelepiped was then assembled by laying alternate layers with the long dimension of each brick oriented north-south, and alternate layers with east-west orientation. Since the dimensions of a brick were not simple multiples of each other, this method of stacking insures that there were no long gaps running vertically through the assembly. We estimate the average bulk density of the assembly as 1.71 gm/cm<sup>3</sup>. This is based on the weight of an average brick, the total number of bricks, and the total volume of the model.

A photograph of the model is shown in Figure 8. A moisture seal was formed by an envelope of 6-mil polyethylene sheeting. The top and bottom of the parallelepiped were covered by double thicknesses. Visible in the photograph is the access scaffold suspended over the assem-



bly to allow adjustment and positioning of the probe on the top surface without having to climb or walk on the model itself. We have made an estimate of how much hydrogen is represented by the moisture seal assuming the hydrogen content of the polyethelene to be distributed throughout the stack. This is 0.005 weight percent of hydrogen, a value low enough to be acceptable to us.

One of the first curves obtained with the die-away probe is shown in Fig. 9. . . A small NaI detector was used because the standard 3" x 3" detector had not yet been received from the supplier. The probe was placed on a large concrete slab. Timing conditions were (5,2500,0,2180, 16) in the convention of Section III. The closed circles show the raw data, and the open circles show the raw data minus an average background determined from channels 2 through 21. The multiplying factor of 5 for the corrected data is merely to normalize the corrected counts to a convenient plotting scale. Channels 22, 23, and 24 are distorted due to the effects of the prompt radiation during the burst, and have been omitted. The corrected curve appears to be purely exponential from about channel 45 on. Our standard data analysis procedure for previous die-away experiments has been to fit data of this type to the form  $Ae^{-\lambda t}$  by using a statistically weighted least-squares method given by Behrens.<sup>8</sup> Fitting the data from channel 45 through 80 can be done with very small uncertainty and gives a mean lifetime  $\tau$  of 243  $\mu$ sec. Measurement of a parameter, the asymptotic mean lifetime, in this case is easily accomplished because the die-away is virtually exponential, and the data over the die-away portion of the curve is much higher than the background.

The traverse measurements on the brick assembly will be discussed first for the case of the  $\text{He}^3$  neutron detector. If the sole purpose of such measurements is to determine how big the models should be, then to a first approximation the same results should be obtained with either neutron or gamma-ray detection.

A typical neutron die-away curve obtained on the brick model is shown in Fig. 10. For this run the target of the Philips tube was 62 in. from the reference edge of the assembly, and the center of the active length of the  $\text{He}^3$  detector was 72 in. from the edge. The solid circles show the data obtained with the detector bare, and the open circles show the data taken with the detector covered by  $1/32''$  of Cd. In both cases the raw data are plotted and normalized at channel 23. Background is 5 counts/channel for the bare counter run and essentially zero for the Cd-covered run. The timing conditions were (10,2500,0,2180,16) for both. It is clear that the assumption of pure exponential decay is not valid for channels earlier than about channel 60. Beyond this point the scatter in the data is sufficiently bad that the assumption of exponential decay may be correct but difficult to substantiate. If exponential decay is assumed for channels beyond 60, and a decay constant  $\lambda$  or mean lifetime  $\tau$  is determined by the method of Behrens<sup>8</sup>, the relative error on the parameter would be large due to the scatter. We did in fact try this, but the results were clearly unmeaningful.

The Cd-covered  $\text{He}^3$  data in Fig. 10 indicate a substantial epithermal contribution to the bare counter die-away curve from channel 23 to about 35. Analysis of the bare counter curve over the region from channel 23 to about 60 must therefore include at least two decay components. We will discuss the problem of data analysis in the next section and will leave it here by stating that a successful data smoothing technique has been developed which allows empirical interpretation of the thermal neutron and gamma-ray die-away data.

Fig. 11 shows a traverse made across the brick assembly with the  $\text{He}^3$  detector in the die-away probe. For all runs the timing conditions were (10,2500,0,2180,16). In all cases the source-detector orientation was opposite to that shown in the inset in Fig. 10, i.e. the detector was always toward the reference edge of the model from the source. The source-detector spacing was 22.5 cm. The solid circles in Fig. 11 represent runs

where the target of the Philips tube was located at the plotted distance from the reference edge. The crosses are runs where the detector was located at the plotted distance. The ordinate is the ratio  $y(30)/y(60)$  which is the ratio at channels 30 and 60 of the smooth approximation to the data. This ratio was one of three parameters calculated and plotted, the other two being

$$-\frac{d \log y(40)}{dt} \quad \text{and} \quad -\frac{d \log y(t \rightarrow \infty)}{dt} .$$

The first of the above two gave a plot somewhat inferior to that of Fig. 11, and the second gave an unreasonable plot. It is perhaps not unexpected that some trial and error is necessary in finding a suitable parameter to plot. The exact shape of the die-away curve will undergo subtle changes as a model edge is approached, and in ways which are difficult to predict theoretically.

The errors on the points in Fig. 11 were obtained from the expression

$$\sigma_R^2 = \sigma_{30}^2 + \sigma_{60}^2$$

where the  $\sigma$ 's are the relative statistical errors in the ratio  $R$ , the counts per channel at 30, and the counts per channel at 60. The value of  $\sigma_R$  so obtained is presumably an upper limit since  $R$  is obtained from a smooth approximation to the data points. From the data in Fig. 11 we have estimated that the edge effect extends inward about 25 in. from each side. Thus, if we include the source-detector spacing of about 10 in., we conclude that for dry brick a lateral dimension of 25" + 25" + 10", or 60 in. would be necessary for an effectively semi-infinite model if the probe is placed in the center.

A set of gamma-ray die-away runs was taken on a traverse across the brick assembly, and analyzed like the  $\text{He}^3$  runs. The best traverse plot did not indicate the expected shape as was obtained in Fig. 11, due to

excessive scatter of the points. We did not understand at the time why these results should be so bad and in fact, it was only after obtaining gamma-ray die-away data on the other models that the reason became clear. Looking forward a bit, we can understand this situation on the basis of Fig. 29. Shown here are die-away curves taken with 122-kev bias on crushed basalt, solid granite, the brick assembly, crushed granite, and carbonate. The data have been corrected for dead-time losses in the time analyzer but not for background, the amount of which can be judged by the points around channel 120. The statistical quality of any parameter extracted from the data is determined by the signal-to-noise ratio S/N for the channel or channels at which the parameter is calculated. The S/N at any channel m is

$$S/N = \frac{\text{Count}(m) - \text{Background}}{\text{Background}} .$$

We have taken channel 60 as representative and have calculated the S/N for the data in Fig. 29 which is listed below:

<u>Model</u>	<u>(S/N)<sub>60</sub></u>
Crushed basalt	1.17
Carbonate	0.681
Solid granite	0.458
Crushed granite	0.365
Brick	0.153

The S/N is determined primarily by two physical phenomena: 1) the number and energy of gamma-rays produced per neutron capture and 2) the die-away rate. Note that the S/N for the brick is less than half of the next highest value. From these results it is perhaps not unreasonable that we were not successful in obtaining a good gamma-ray traverse on the brick model.

Fig. 12 shows the results of  $\text{He}^3$  traverse on a solid granite block. This model is 84" x 84" x 48". The source-detector spacing was 25 cm and the timing conditions were (100,5000,0,4680,16). The circles and crosses have the same meaning as in Fig. 11, and the errors have been calculated in the same way. The behavior of this plot is unusual in that the deviation as the edge is approached is more drastic for the source near the edge than for the detector. We estimate from Fig. 12 that the edge effect extends in about 16 in. for either case, including a 10-in. source-detector spacing, we conclude that a lateral dimension of about 42-in. would be effectively semi-infinite for dense granite.

In Fig. 13 we have plotted the minimum lateral dimensions obtained from the traverse measurements on the brick assembly and the dense granite versus the respective densities of 1.71 and 2.63 gm/cm<sup>3</sup>. Plotting as a function of density is somewhat arbitrary, but it is probably the single physical parameter which most influences the model size needed. This two-point plot is regarded as only an empirical guide in determining necessary model sizes.

## V. DATA ANALYSIS METHODS

Die-away data obtained with the TMC CN110 computer and Model 211 Time-of-Flight logic must be corrected for dead-time losses in the system. The dead time mechanism in the time analyzer is such that the dead time is not constant but has an average value of  $(16 + \frac{1}{2} \Delta t)$   $\mu\text{sec}$  when a channel width of  $\Delta t$   $\mu\text{sec}$  is used. A statistical treatment of the loss problem has yielded the following correction formula<sup>7</sup>:

$$CA_n = -T \log_e \left\{ 1 - \frac{c_n}{T - \sum_{k=n-\frac{16}{\Delta t}}^{n-1} c_k} \right\} \quad (15)$$

where

- $CA_n$  = loss-corrected count in channel  $n$ ,
- $T$  = number of analysis cycles in a run,
- $c_n$  = raw count in channel  $n$ .

For the case of 16- $\mu\text{sec}$  channels, with which most of the data in this report were taken, the correction formula becomes

$$CA_n = -T \log_e \left( 1 - \frac{c_n}{T - c_{n-1}} \right) \quad (16)$$

The dead time of both the NaI and  $\text{He}^3$  detectors is less than that of the time analyzer so that the  $CA_n$  represent the counts which would be obtained with a system having zero dead time.

We now discuss analysis of loss-corrected data such as that shown in Figs. 9 and 10. These data include a background which is independent of time when compared to the analysis cycle time. This background is measured in the early channels preceding the burst. An average background  $\bar{A}_0$  is obtained from these channels by

$$\bar{A}_0 = \frac{1}{Q-P+1} \sum_{n=P}^Q CA_n$$

where P and Q are suitable early channels. The loss- and background-corrected counts  $CC_n$  are given by

$$CC_n = CA_n - \bar{A}_0 \quad (17)$$

The ideal data analysis scheme should proceed as follows. A theoretical expression is obtained for the response of either the NaI crystal, or the bare or Cd-covered  $He^3$  detector. For a given case let this be  $y_n$ , where

$$y_n = f_n(\Sigma_a, D, p_1, p_2, \dots, p_m). \quad (18)$$

$\Sigma_a$  and D are the thermal-neutron macroscopic absorption cross section and diffusion coefficient, and  $p_1$  through  $p_m$  are m epithermal-neutron and fast-neutron parameters. In writing Eq.(18) in this functional form, we are assuming that Eq.(5) is basically correct, the only problem being that of a correct source condition. A best fit is sought over a suitable portion of the die-away curve of  $y_n$  to the data  $CC_n$ . Thus we might form the sum

$$S = \sum_{n=x}^y (y_n - CC_n)^2 w_n \quad (19)$$

where the  $w_n$  are weighting factors. Then the values of the neutron parameters which yield the best fit in a least squares sense would be obtained from the solution of the following set of equations:

$$\frac{\partial S}{\partial \Sigma_a} = \frac{\partial S}{\partial D} = \frac{\partial S}{\partial p_1} = \dots = \frac{\partial S}{\partial p_m} = 0.$$

From a comparison of the shape of the theoretical curves in Fig. 2 and the

data in Fig. 10, it seems clear that the functional form given in Eq.(9) would not give a suitable fit to the neutron die-away. Therefore some method other than the ideal analysis scheme must be used.

An alternative to the scheme above is to construct an empirical calibration curve for the die-away method by using the experimental results from several models. This is the procedure followed in the work reported here. In such an empirical approach, two problems must be solved. First, some data smoothing or averaging procedure is needed to reduce the statistical scatter in the point-by-point decay curve. Second, some suitable parameter must be found which can be extracted from the smooth approximation and plotted in a calibration curve. The second problem has already been touched upon in the discussion on the traverse results. We now discuss the first problem.

The problem of data smoothing, or correctly speaking interpolation, has many solutions. One can do local fitting to a few points or overall fitting to almost all data points. Furthermore the choices of functional form are literally infinite in number. We decided to attempt smoothing over essentially all of the usable die-away. The choice of functional form was guided somewhat by the data in Fig. 10. Since the bare  $\text{He}^3$  counter sees at least what the same counter sees when it is Cd covered, the bare counter decay curve must include a component for epithermal die-away. When this component, which is proportional to the open-circle data in Fig. 10, is approximately stripped from the solid-circle data, at least two decay components appear to remain. Therefore, a reasonable trial choice of the functional form is

$$y_n = A_1 e^{-\lambda_1 n} + A_2 e^{-\lambda_2 n} + A_3 e^{-\lambda_3 n}, \quad (21)$$

where the decay constants have units of inverse channels rather than inverse time. It should be stated that the use of this functional form does not imply either that it is the  $f_n$  of Eq.(18), or that three spatial modes exist in the neutron distribution. This form is to be regarded



only as convenient and hopefully adequate. Little physical significance is attached to the parameters in Eq.(21).

In order to determine values of the parameters which give a best fit to the data in the least squares sense, we form the sum  $S$  in Eq.(19), and try to minimize  $S$  with respect to  $A_1, A_2, A_3, \lambda_1, \lambda_2, \lambda_3$ . The first minimizing technique which we tried was based on an IBM Share program called "Non-Linear Least Squares Parameter Estimation Program". In this routine a set of input guesses for the six parameters is used to calculate a beginning value for  $S$ . From this value a local minimum of the surface  $S$  in the six-parameter space is sought by changing the values of the parameters and calculating  $S$  at each step. The iteration process stops when a preset convergence criterion is satisfied. Results of fitting with this routine are not shown because it soon became apparent that some serious difficulties existed. In several cases, some reasonable input guesses resulted in a smooth curve fit which was quite unreasonable. Also in several cases the convergence criterion, which was not strict, was not met. Calculations stopped only after an allowed run time had elapsed, and more than a hundred iterations had been performed.

A second fitting method tried was based on a paper by Aigner and Flamm<sup>9</sup>. The method is non-iterative, so no input guesses are required. The function  $S$  is minimized in a unique way by performing successively two linear least squares fits. The first involves only  $x_1, x_2$ , and  $x_3$ , where  $x_i = e^{-\lambda_i t}$ , and the second involves only  $A_1, A_2$ , and  $A_3$ . The only restriction on the method is that the data points be equally spaced in time, which is the case for data from a multichannel time analyzer. In order to test the method, an exact test case was prepared and the method applied to it. It was found that the values of  $x_1, x_2$ , and  $x_3$  were unusually sensitive to the accuracy of the arithmetic operations performed during the calculation. When the method was applied to several real cases, in each instance one of the set  $x_1, x_2, x_3$  came out negative. This is physically unreal in terms of the value of  $\lambda$  it would imply.

This negative value of  $x$  also caused the corresponding coefficient  $A$  to be zero, thus completely eliminating one of the terms in  $y_n$ .

A third method we tried was that of Cornell<sup>10</sup>. This method, like that of Aigner and Flamm, is non-iterative. Sums over successive data points are set equal to their theoretical expectation values based on a given number of exponentials. This gives a determined set of equations which can be solved for the quantities  $x_1, x_2, x_3$  and  $A_1, A_2, A_3$  for the case of three exponentials. Here,  $x_i = e^{-K\lambda_i}$ , where  $K$  is a positive integer depending on the total number of data points to be fit. When Cornell's method was applied to the prepared exact test case, it gave the correct values for all the parameters without any indication of undue sensitivity to arithmetic accuracy. However, when the method was applied to several real cases, we again obtained one negative value among the set  $x_1, x_2, x_3$ , and thus a meaningless value for the corresponding  $\lambda$ .

Apparently the difficulty lies in the fact that these non-iterative methods are quite capable of giving unusable values of  $e^{-\lambda_i}$  or  $e^{-K\lambda_i}$  when the data cannot truly be represented by a sum of exponentials. In iterative methods where one begins with a form consisting of a sum of exponentials, it is not possible for the parameter values to ever get into unphysical domains.

The method which we have used for analysis of all data shown in this report is an iterative scheme called GAUSHAUS.<sup>11</sup> It is like the IBM Share program in that input guesses for the function parameters are required to obtain the initial value of  $S$ . In GAUSHAUS, one of two convergence criteria can be selected, the first based on the relative change in  $S$  from the  $i$ 'th to the  $(i + 1)$  iteration, and the second based on the relative change of each parameter from the  $i$ 'th to the  $(i + 1)$  iteration. We have so far used only the criterion based on  $S$ . Throughout our use of GAUSHAUS, the weighting factors  $w_n$  were set equal to unity. Several examples of the application of GAUSHAUS to die-away data are given in this report. We have found the program to be satisfactory as a data smoothing technique. Good fits were obtained in all cases after a reasonable number of iterations, and the average run time per case on a CDC 1604 computer was just over one minute.

## VI. PHYSICAL AND CHEMICAL PROPERTIES OF ROCK MODELS

In this section we will summarize the pertinent properties of all the rock models which were used in the die-away studies. This separate summary avoids the necessity of interrupting the subsequent discussions on the results of the die-away experiment. We list below some of the data on the five models:

### Brick Assembly:

Source: Ferris Brick Company  
Ferris, Texas  
Type: Ferris Common Pink  
Dimensions: 116" x 116" x 65"  
Gross density: 1.71 gm/cm<sup>3</sup>

### Solid Granite:

Source: Texas Granite Corporation  
P.O. Box Q  
Marble Falls, Texas 78654  
Type: Texas Rockville  
Dimensions: 84" x 84" x 48"  
Gross density: 2.63 gm/cm<sup>3</sup>

### Crushed Granite:

Source: Bilbrough Marble Company  
Burnet, Texas  
Type: Burnet Red, Grade No. 1  
Dimensions: 117" dia. x 69" height  
Gross density: 1.42 gm/cm<sup>3</sup>

### Crushed Basalt:

Source: Trap Rock Plant  
Knippa, Texas  
c/o Trinity Concrete Products  
P.O. Box 21025  
Dallas, Texas  
Type: Knippa,  $\frac{1}{4}$  inch - 20 mesh  
Dimensions: 117" dia. x 69" height  
Gross density: 1.62 gm/cm<sup>3</sup>

Crushed Carbonate:

Source: Bilbrough Marble Co.  
Burnet, Texas

Type: Demarco Black, Grade No. 1

Dimensions: 117" dia. x 69" height

Gross Density: 1.31 gm/cm<sup>3</sup>

The density of the brick assembly was determined by obtaining an average weight per brick from several bricks, multiplying this average by the total number of bricks and dividing by the overall volume of the assembly. The density of Texas Rockville has been measured several times by various people and is a well-established property. The density of the three crushed rock models was determined by repeated measurements of weight and volume of small samples (~ 5 gal) of regular geometric shape.

We have already discussed the brick model shown in Fig. 8. Fig. 14 shows the solid granite model with the die-away probe placed on it in the vertical orientation. Fig. 15 shows one of the crushed rock models, each of which looks the same. The crushed rock is completely enclosed by 6-mil polyethelene sheet and is contained in a thin corrugated steel tank. Fig. 16 shows the layered model which consists of crushed granite rock contained inside a thin corrugated steel band which has no bottom, and which is placed on the solid granite model. No polyethelene is used around the crushed rock in this case. Fig. 17 shows the crushed basalt model where the polyethelene has been slit open and laid back so that an irregular surface feature - in this case a crater - could be formed. The arrangement shown, wherein the die-away probe spans the crater and is parallel to the undisturbed surface, is called irregularity "A".

Chemical analyses were performed on all rock samples by two commercial analytical laboratories. These are Spectrochemical Laboratories, Inc., 8350 Frankstown Ave., Pittsburgh, Pennsylvania 15221,

and Metallurgical Laboratories, Inc., 1142 Howard St., San Francisco, California 94103. A comparison of the results is shown in Table 2, where the upper set of figures is the weight percent reported by Spectrochemical and the lower set is from Metallurgical. The methods of reporting are the same except that Metallurgical treats all Fe as  $\text{Fe}_2\text{O}_3$ . Agreement between the two is fairly good with the exception of  $\text{Li}_2\text{O}$ , where differences of two orders of magnitude exist. If we were concerned with fast neutron phenomena, this difference would be annoying but not so important. However, since we measure thermal neutron die-away, and Li has a relatively large thermal neutron capture cross section, the amount of this element present is vitally important. In fact, at the Li level reported by Spectrochemical, the die-away rate would depend rather weakly on the amounts of all other elements in Table 2 which are present. It is the opinion of several geologists that lithium oxide concentrations in the range of a few tenths of weight percent are unreasonably high. These results, obtained by wet chemistry, are now presumed to be in error. The  $\text{Li}_2\text{O}$  concentrations reported by Metallurgical Laboratories were obtained by atomic absorption which is a more reliable method. Both laboratories reported that other strongly absorbing elements (e.g. Cl, Gd, and other rare earths) are not present at sufficiently high levels to appreciably affect the thermal neutron die-away.

Table 3 shows the elemental weight percents deduced from the results in Table 2. Only the data of Metallurgical Laboratories were used since we feel they may be more trustworthy. Except for the discrepancy in Li, it would make little difference which set we used in calculating macroscopic cross sections. Oxygen is not shown since its thermal neutron capture cross section is practically zero, and it will not affect thermal die-away rates.

For reference we have listed in Table 4 the thermal neutron absorption parameter  $\sigma_a/A$  scaled up by 1000. The quantities  $\sigma_a$  and A

are the elemental microscopic thermal neutron absorption cross section and atomic weight, respectively. Values of  $\sigma_a$  for Fe and Ca were taken from the Chart of the Nuclides<sup>12</sup>, while the others are from the Brookhaven compilation<sup>13</sup>. From the table it is evident that Li and B will dominate in the thermal neutron die-away process unless their concentrations are about three to four orders of magnitude less than the other elements in Table 4.

The macroscopic absorption cross section  $\Sigma_a$  is defined by

$$\Sigma_a = 0.602 \rho \sum_i \frac{w_i \sigma_{ai}}{A_i} \quad (22)$$

where

- $\rho$  = gross density (gm/cm<sup>3</sup>)
- $w_i$  = weight fraction of i'th type element
- $\sigma_{ai}$  = microscopic thermal absorption cross section for i'th type element (barns)
- $A_i$  = atomic weight of i'th type element.

The parameter  $\Sigma_a/\rho$  may be calculated for each rock model by using the data in Tables 3 and 4. The parameter  $\Sigma_a$  can then be obtained from the known densities. Table 5 shows values of  $\rho$ ,  $\Sigma_a/\rho$ , and  $\Sigma_a$  for each model. Note that the values of  $\Sigma_a/\rho$  for the crushed and solid granite differ by only about 5%, and these differ from that for basalt by about 34%. The values of  $\Sigma_a$  given in Table 5 will be the quantities which will be plotted in empirical calibration curves against a parameter which will be obtained from the smooth approximation to the die-away data resulting from the GAUSHAUS program.

## VII. RESULTS OF OPTIMUM THERMAL DIE-AWAY MEASUREMENTS

We will now discuss the experimental results of optimum thermal die-away measurements on the crushed basalt, crushed granite, solid granite, and crushed carbonate models. These measurements are optimum only in a certain sense and within a limited definition. For example, whereas the combination neutron experiment will probably use a 5- or 10- $\mu$ sec source burst, a longer burst of 100  $\mu$ sec was used in the studies to be discussed in order to reduce run times so that statistically good data could be obtained in 30 min. Also, for the gamma-ray die-away runs, the photomultiplier tube was gated off during the 100- $\mu$ sec burst. This was necessary to eliminate distortions in the data which develop if the tube is not gated and the neutron output is sufficiently high to give good statistics on the data points in a 30-min run. This point will be taken up in Section XII.

For all cases discussed in this section, the die-away probe was oriented horizontally, the source-detector spacing was 25 cm, and the center of the spacing was placed at the center of the model surface. The probe was that shown in Fig. 5, which places the axis of the target-detector line 2 in. above the model surface.

Representative runs on each of the four models obtained with the bare  $\text{He}^3$  detector are shown in Figs. 18-21. The run time for each was 30 min., and the neutron output per burst was about  $2 \times 10^4$ . The timing combination for each was (100,5000,0,4680,16). With a period of 5000  $\mu$ sec, and a resulting repetition rate of 200 pulses/sec, the average neutron output was about  $4 \times 10^6$  neutrons/sec, and the total output per run was about  $7 \times 10^9$  neutrons. The data in Figs. 18-21 include background which is less than 10 counts/channel in each case. The channels up to channel 23 which contain only background could not be plotted on the ordinate scale used. The data points have not been corrected for dead-time losses in the time analyzer. Thus, the quantity  $C_n$  [see Eq.(16)] is shown.

The lss- and background-corrected counts  $CC_n$  for the four runs in Figs. 18-21 are shown together in Fig. 22. Note that the data points do not suggest even qualitative agreement with the theoretical curves in Fig. 2. The smooth curves through the points are the result of fits using GAUSHAUS. The beginning point for each fit is about 100  $\mu$ sec after the end of the burst. The counts at the beginning of the analyzed curve for each model show an interesting and explainable trend, viz, an increase with increasing density. For small  $t$ , the neutron density is given approximately by [see Eq.(9)] .

$$n(r,z) \approx \frac{Se^{-\frac{r^2}{4\theta}}}{(4\pi\theta)^{3/2}} \left\{ e^{-\frac{(z-d)^2}{4\theta}} - e^{-\frac{(z+d)^2}{4\theta}} \right\} \quad (23)$$

The Fermi or symbolic age  $\theta$  is defined by

$$\theta = \int_0^u \frac{1}{3\xi\Sigma_s^2(1-\langle\cos\theta\rangle_{av})} du' \quad (24)$$

where

$$u = \ln E/E_0 = \text{lethargy from source energy } E_0 \text{ to energy } E,$$

$$\xi = \text{average logarithmic energy decrement per collision,}$$

$$\Sigma_s(u) = \text{lethargy-dependent macroscopic neutron scattering cross section,}$$

$$\langle\cos\theta\rangle_{av} = \text{average cosine of the angle of scattering.}$$

Note that since  $\Sigma_s \approx \rho$ , then  $\theta \approx \rho^{-2}$ , and the age decreases as the density increases. It is easy to show that if  $r$  and  $z$  are small compared to  $\theta^{1/2}$ , the age-dependence of Eq.(23) is given approximately by  $n \sim \theta^{-5/2}$ , and therefore  $n \sim \rho^5$ . A value of 25 cm for  $r$  is not small compared to  $\theta^{1/2}$ , so the fifth-power dependence on  $\rho$  is probably much too strong. Nevertheless, the foregoing argument makes plausible the observed early magnitude of the die-away curves.



The later portion of the curves in Fig. 22 must be used to obtain an empirical calibration curve for the die-away as measured by the  $\text{He}^3$  detector. Two experimental parameters were tried. These were ratios of the ordinates at various time delays, and the negative logarithmic slope of the curve at various delays. The later quantity must approach  $v\Sigma_a$  asymptotically, but the statistical uncertainty on the slope will clearly get rather large the farther out in time one goes. A good compromise seems to be to calculate the slope at some intermediate delay, and this was done to give the calibration curve shown in Fig. 23. A delay of 770  $\mu\text{sec}$  was chosen. The trend of the points gives a smooth curve, and interpolation between points should be trustworthy. Extrapolation of the curve probably is not safe, especially at the low end. This is because the behavior in this region suggests that the abscissa will be intercepted to the left of the  $\Sigma_a$  axis. In other words, for a material with zero absorption, a die-away curve of positive slope would be observed, which is clearly a physical impossibility. In fact, for  $\Sigma_a = 0$ , the abscissa intercept must be to the right of the  $\Sigma_a$  axis because die-away still occurs due to leakage. In this respect note that from Eq.(11) if  $\Sigma_a = 0$ ,  $n \sim e^{-v\Sigma_l t}$ . We must conclude that the calibration curve in Fig. 23 is not valid beyond the end points on the curve.

In preparation for discussion of gamma-ray die-away as measured by the  $3'' \times 3'' \text{ NaI/B}^{10}$  detector, we show in Fig. 24 a relevant pulse height spectrum taken on the crushed basalt model. Note that a 500- $\mu\text{sec}$  coincidence counting gate was used which was delayed 100  $\mu\text{sec}$  from the end of the burst, and that a 140- $\mu\text{sec}$  PM gate was used. Although this is labelled a capture spectrum, it is actually a mixture of capture and activation gamma rays, plus background. Both spectra were stored for 60 min, the repetition rate was 200 pulses/sec, and the neutron output for the raw spectrum was about  $1 \times 10^4$  neutrons/burst. The background consists primarily of 1.46-Mev gamma rays from  $\text{K}^{40}$ . The most prominent feature in the raw spectrum is the 0.478-Mev line, presumably due to

thermal neutron capture by  $B^{10}$  around the NaI crystal. This line probably has a small admixture of 0.511-Mev annihilation radiation, although it is not sufficiently intense to cause a significant shift from the energy of the gamma ray from the  $B^{10}(n, \alpha)Li^7$  reaction. The high intensity of this line led us to speculate that if the gamma-ray die-away were measured with a differential pulse-height window enveloping the 0.478-Mev peak, then the results would be a mixture of the neutron die-away and that of the capture gamma rays produced in the models. For this reason we took NaI/ $B^{10}$  die-away runs in pairs - one with an integral bias at 122 kev (channel 12), and one with a 300- to 510-kev window.

The pairs of gamma-ray runs are shown in Figs. 25-28. The run time for each was 30 min, and the neutron output per burst was about  $1 \times 10^4$ . The timing combination for each run was (100,5000,140,4680,16). The repetition rate of 200 pulses/sec yielded an average output of about  $2 \times 10^6$  neutrons/sec and a total output per run of about  $4 \times 10^9$  neutrons. The raw data have been plotted. For this detector the background is sufficiently large that it can be plotted on the scale used. An alternate presentation of the gamma-ray data is shown in Fig. 29. These data are the 122-kev runs shown in Figs. 25-28, plus a similar run on the brick model, corrected for dead-time losses. Background has not been subtracted for any case. The S/N ratios for these curves were discussed in Section IV in connection with the difficulty encountered in obtaining a meaningful gamma-ray traverse on the brick assembly. It is now of interest to calculate the S/N for the two types of gamma-ray curves. Again using channel 60 as a reference, the table below shows the ratios for the data in Figs. 25-28.

<u>Model</u>	<u>(S/N)<sub>122 kev</sub></u>	<u>(S/N)<sub>300-510 kev</sub></u>
Crushed basalt	1.17	1.30
Crushed granite	0.365	0.635
Solid granite	0.458	0.553
Carbonate	0.681	1.16

It is interesting that the increase in S/N is not to the same extent for all four cases. The basalt and solid granite, which show an intense die-away component, are helped relatively little by use of the pulse height window. The crushed granite and carbonate, whose die-away intensities are not so great, are helped considerably. Even though the S/N ratio is increased by the use of a differential window enveloping the  $B^{10}$  capture line, this does not necessarily mean that empirical parameters obtained from such runs will be statistically better than those obtained from the integral bias runs. The total count in a run also will enter the statistical considerations.

Fig. 30 shows two examples of analyzed gamma-ray runs. These are the solid granite and carbonate runs taken at 122-kev integral bias and are the upper sets of data shown in Figs. 27 and 28. The data points are the  $CA_n$ , i.e. they have been corrected for dead-time losses. The solid curve in each case is  $y_n + \bar{A}_0$ , where  $y_n$  is given by Eq.(21), except that only two exponentials were required. The background was left in these plots to give an indication of how well the curve fitting procedure does over the entire die-away. The use of only two terms in  $y_n$  is characteristic of all the gamma-ray runs. Fitting tests using two and three terms in  $y_n$  showed no essential difference between these as evidenced by the final values of the sum  $S$  in Eq.(19). The use of two terms is preferable since it leads to a shorter calculation time per fit.

Figure 31 shows a set of analyzed gamma-ray runs with  $\bar{A}_0$  subtracted; thus, the quantity plotted is  $CC_n$ . These data are the 122-kev bias runs in Figs. 25-28, and the smooth curves are the  $y_n$  functions resulting from GAUSHAUS. Although they are not shown, the corresponding runs for the 300-510 kev window show no significant deviations from the 122-kev data. Apparently the number of counts in the window due to gamma rays originating from the model is at least comparable to the number produced by neutron capture in the  $B^{10}$ . The data of the Fig. 24 are consistent with this conclusion. The data and curves in Fig. 31 have been normalized at the beginning of the

measured decay so that the rather bad statistical scatter in the region 1000-1500  $\mu\text{sec}$  does not appear too confusing. The same two methods, i.e., ratios and negative logarithmic slopes, were tried on the smooth curve approximations in Fig. 31 in order to obtain an empirical parameter for a calibration plot. The slope of the curves appeared to be most suitable, and Fig. 32 shows a calibration curve obtained by calculating this quantity at a delay of 610  $\mu\text{sec}$ . The delay for the gamma-ray curves is 160  $\mu\text{sec}$  less than for the neutron curves, but the certainty of fit on the data in Fig. 31 is not as good at a comparable delay as in Fig. 22. The calibration points in Fig. 32 suggest nothing better than a straight line fit, which has been drawn. At least this calibration curve has the virtue that for  $\Sigma_a = 0$ , the abscissa is intercepted on the positive side. Without additional knowledge, however, we can only say that for the gamma-ray calibration curve, as for the neutron curve, interpolation is legitimate but extrapolation would be questionable.

#### VIII. RESULTS OF EPITHERMAL DIE-AWAY MEASUREMENTS

The experimental results of epithermal die-away measurements on crushed basalt, crushed granite, and solid granite models will be discussed in this section. For all cases the die-away probe was oriented horizontally, the source-detector spacing was 25 cm, and the center of the spacing was placed at the center of the model surface. The probe was that shown in Fig. 5, which places the axis of the target-detector line 2 in. above the model surface.

Representative runs on each of the three models obtained with a Cd-covered  $\text{He}^3$  detector are shown in Fig. 33. Also shown in Fig. 33 is the time distribution of the source neutrons in the burst from the Philips neutron tube. The run time for each  $\text{He}^3/\text{Cd}$  run was 30 min., and the neutron output was about  $2 \times 10^3$  neutrons per burst. The timing combination for each run was (10,2500,0,0,0.5). With a period of 2500  $\mu\text{sec}$  and a resulting repetition rate of 400 pulses/sec, the average neutron output was about  $8 \times 10^5$  neutrons/sec, and the total output per run was about  $7 \times 10^8$  neutrons.

The experimental arrangement for measuring the time distribution of neutrons in the burst was a modification of that used for the die-away measurements as shown in Fig. 6. In making the neutron burst measurement, a Dumont 6292 PM tube and a 1.5" dia. by 0.375" thick Pilot B plastic scintillator made up the fast neutron detector. The PM tube was, of course, not gated. Pulses from the PM tube were fed into an amplifier with integral discriminator. Pulse discrimination allowed only pulses with amplitudes greater than those from 9-Mev recoil protons to be time analyzed. The run time for measuring the time distribution of fast neutrons in the neutron burst was 30 min., and the neutron output was about  $2 \times 10^2$  neutrons per burst. The timing combination for this measurement was (10,2500,0,4,0.5). With a period of 2500  $\mu\text{sec}$  and a resulting 400 per/sec repetition rate, the average neutron output was about  $8 \times 10^4$  neutrons/sec, and the total output for the run was about  $7 \times 10^7$  neutrons. The beginning of the burst of fast

neutrons occurs approximately 7  $\mu$ sec before the build-up of epithermal neutrons. However, in Fig. 33 the neutron burst has plotted, i.e., shifted 7  $\mu$ sec later in time, to coincide with the beginning of the epithermal die-away curves. Such a plot shows more clearly the effect of the long and irregular shape of the fall time of the fast neutron burst on the epithermal die-away curves.

The approximately 7  $\mu$ sec difference in the fast neutron build-up and the epithermal neutron build-up is, we believe, a real effect, namely the slowing down time of the 14 Mev neutrons to epithermal energies. It is immediately evident that if this is truly the cause of the difference in time between the fast and the epithermal neutron build-up, then rock matrices containing different amounts of hydrogen should show a shorter time difference for the rock containing the greater amount of hydrogen. Our crushed basalt, crushed granite, and solid granite models contain different amounts of water per unit volume of model. However, under the conditions of our measurements, there appears to be no significant difference in the time of the fast and epithermal neutron build-up for these models. When our epithermal die-away and fast neutron burst measurements were made; the object was not to measure any such time differences. Furthermore, our existing timing electronics is not adequate for measurements of this type. We do, however, plan further investigation of this phenomenon using suitable timing circuitry.

The failure of the Philips neutron tube to produce a well defined 10- $\mu$ sec burst of fast neutrons introduces a very significant distortion into the epithermal neutron die-away measurements. The long tailing of the fast neutron burst distorted the epithermal capture gamma-ray die-away measurements to the extent that no epithermal information could be extracted from the die-away curves. Examples of epithermal neutron-capture gamma-ray measurements are shown in Fig. 34 and will be discussed in detail later in this section.

The fast neutron burst has a rise time of about 7  $\mu$ sec, and the fall time is irregular and lasts approximately 40  $\mu$ sec. This long and irregular

fall time of the fast neutron burst distorts the first 60  $\mu$ sec or so of the epithermal neutron die-away curves and therefore, all information contained in the first 60  $\mu$ sec of the die-away is virtually destroyed. Fast neutrons, which attain thermal energies prior to the final termination of 14 Mev neutron production, do not affect the epithermal neutron die-away measurements made with a Cd-covered  $\text{He}^3$  counter because the thermal neutrons are captured by Cd surrounding the  $\text{He}^3$  detector. Consequently, the epithermal neutron die-away attains a die-away characteristic of the moderating properties of the rock matrix soon after the last 14 Mev neutrons in the burst are produced. The die-away curves shown in Fig. 33 for the three rock models show easily identifiable die-away character in about 60 to 70  $\mu$ sec following the beginning of the fast neutron burst. The rate of die-away is smallest for the crushed granite ( $\rho = 1.42$ ), greater for the solid granite ( $\rho = 2.63$ ), and greatest for the crushed basalt ( $\rho = 1.62$ ). Since hydrogen in the matrix should dominate the epithermal die-away, these die-away measurements indicate that the hydrogen per unit volume of these models is least in the crushed granite, greater in the solid granite, and the greatest in the crushed basalt.

The NMR (nuclear magnetic resonance) Section of our laboratory has developed an NMR technique of measuring water content in rock samples. We prevailed upon our NMR group to analyze samples from our crushed granite, solid granite, and crushed basalt models for water content and their results are shown in the table below.

<u>Model</u>	<u>Density-gms/cm<sup>3</sup></u>	<u>Wt.% H<sub>2</sub>O</u>	<u>H<sub>2</sub>O - gm/cm<sup>3</sup></u>
Crushed basalt	1.62	.92	.015
Solid granite	2.63	.37	.0097
Crushed granite	1.42	.36	.0051

The qualitative agreement between the epithermal neutron die-away measurements and the corresponding NMR measurements of the water content in the rock samples from the models show epithermal neutron die-away to be quite sensitive to very small quantities of water in the rock. Inherent within our particular NMR equipment, however, is an as yet undetermined uncertainty for values of water content in rocks that contain so little water. The best that can be stated at this time is that the NMR values represent lower limits for the water content of these rock samples. Therefore, although one would like to make a calibration curve from the present data, a calibration curve formulated from these data could not be considered absolutely reliable. These data do show conclusively, however, that the epithermal die-away method is very sensitive to small amounts of water in rock samples. Therefore, at the time that the water content (of rock samples) can be measured with both upper and lower limits, a calibration curve of the water content versus an epithermal die-away parameter can be made.

Representative runs on the solid granite and crushed granite models obtained with a 3" dia. x 3" long NaI detector integrally biased at 122-keV gamma-ray energy are shown in Fig. 34. The run time for each epithermal neutron-capture gamma-ray die-away run was 30 min., and the neutron output was about  $2 \times 10^2$  n/burst. The timing combination of each NaI run was (10,2500,20,0,0.5). With a period of 2500  $\mu$ sec and the resulting repetition rate of 400 pulses/sec, the average neutron output was about  $8 \times 10^4$  neutron/sec and the total output per run was about  $7 \times 10^7$  neutrons. The die-away curves for the crushed granite and solid granite exhibit no features that suggest a difference in the water content of the two models. The reason there is no indication of the difference in hydrogen content of these two models is that the epithermal capture gamma-rays have been obscured by thermal neutron-capture gamma-rays. Thermal neutron-capture gamma rays begin to occur in great abundance in 20 to 40  $\mu$ sec following the beginning of fast neutron production. Therefore, the least obscured epithermal capture gamma-ray die-away information is contained in the die-away that occurs during



this 20 to 40  $\mu$ sec period. This is also true if epithermal die-away measurements are obtained with a bare  $\text{He}^3$  detector. Since this is the case, the requirements on the fast neutron burst shape and duration are rather stringent. A satisfactory neutron burst for epithermal die-away measurements should have a total duration of not more than 10  $\mu$ sec, and the fall time should be 2  $\mu$ sec or less. The rise time of the burst is not so critical but should be as fast as possible. The neutron burst shape and duration are not so critical when making epithermal neutron die-away measurements with a Cd-covered  $\text{He}^3$  detector because the thermal neutrons are absorbed in the Cd and therefore, never produce detectable effect on the epithermal die-away. Unfortunately, there is no similar way to discriminate between thermal and epithermal neutron-capture gamma rays since the gamma rays have the same energies.

The neutron burst from our Philips neutron generator does not meet these strict requirements as is evident from the source neutron time distribution of the burst shown in Fig. 33. We plan to modify our pulsing system in order to be able to obtain the hydrogen information contained in the epithermal die-away as measured with a NaI detector or a bare  $\text{He}^3$  detector.

In conclusion, our epithermal neutron die-away measurements obtained with a Cd-covered  $\text{He}^3$  detector show a definite and very sensitive response to very small quantities of water in a rock matrix. This information will also be contained in epithermal die-away curves obtained with either a NaI or a bare  $\text{He}^3$  detector. We believe this information can be extracted provided the fast neutron burst meets certain minimum specifications of fall time, duration, and rise time.

## IX. LAYERING STUDIES

The model on which the layering studies were carried out is shown in Fig. 16. This consisted of a thin (20 gage) corrugated steel band placed on the solid granite model. Layers of crushed granite (Burnet Red) were successively built up by adding rock to the small tank which the band formed. The dimensions of the band are 76" dia. x 26" height.

An early set of layering experiments was carried out in which the crushed rock was contained not by the steel band but by a plywood tray made of 3/4 in. thick wood. When the results of these first studies were analyzed, it was apparent that an inconsistency existed. After much trial and error, the trouble was discovered and is illustrated in Fig. 35. Two  $\text{He}^3$  die-away runs are shown, one for the wooden tray and one for the steel band. In each case the thickness of crushed granite was zero, so the observed die-away should be the same as for the bare block, providing that the retaining trays are not influencing the die-away. The die-away curve obtained with neither tray in position overlays the open circle data in Fig. 35 to within expected statistical uncertainties, indicating no effect on the neutron die-away from the thin steel. Note, however, the large containing effect due to the wooden tray. The magnitude of the effect is surprisingly large and is an example of the rather unusual phenomena which can arise in pulsed neutron experiments. Containment by the wooden tray would hardly be observed in the steady-state case. The layering results reported below were all obtained with the thin steel band retaining the crushed granite.

Gamma ray, thermal neutron, and epithermal neutron die-away runs were taken on the layered model for layer thicknesses of 0, 3, 6, 12, 18, and 24 in. The gamma-ray runs included both integral and differential energy biases, and source-detector spacings of 25 and 50 cm were used for all runs. Horizontal orientation was used throughout.

Fig. 36 shows some of the runs obtained with the bare  $\text{He}^3$  counter at 25-cm spacing. The curves have been normalized at the beginning of

the die-away. The 3-in. layer has a large effect on the die-away rate as evidenced by a comparison of the set of curves. This is not unexpected since thermal neutrons have such a relatively short mean free path in matter. The curve for the 24-in. layer is close to that for an infinitely thick crushed layer. The curve for the latter is that obtained on the full crushed granite model.

Fig. 37 shows the  $\text{NaI/B}^{10}$  runs for the two extreme cases of solid and crushed granite, and 3 layer thicknesses. Again the curves have been normalized at the beginning of the measured decay. The curves for the 6- and 18-in. layers fall properly in the set but have been omitted for the sake of clarity. The smooth curves here, as well as in the previous figure, are the results of curve fitting by GAUSHAUS. Data points are shown for the extreme cases for illustrative purposes. The 3-in. layer here does not have such a large effect on the die-away as the  $\text{He}^3$  case, presumably due to the longer mean free path of the capture gamma rays in matter.

The results of either neutron or gamma-ray die-away clearly indicate that the presence of a layer of material on top of a different material (different here by virtue of a contrast in density) is reflected in the die-away curves. The important question is the following. Can one distinguish between the case of true layering and that of a homogeneous medium whose physical properties are intermediate between those of the two layered media? Early theoretical calculations, the results of which were quoted in the paper by Caldwell et al<sup>1</sup>, indicated there was a possibility of distinguishing these cases on the basis of a detailed analysis of the entire thermal neutron die-away curve. However, the theory used was comparable to that developed in Section II of this report. In view of the failure of the theory in Section II to predict the correct shape of the neutron die-away curves as discussed previously, doubt must be cast on any detailed predictions of these rather simple theories.

The  $\text{He}^3$  curve for the case of a 24-in. layer gives some indication of an early decay characteristic of the upper layer and an asymptotic decay between those of the upper and lower media. This effect is of such small magnitude, however, that it is doubtful if it could be used practically. The gamma-ray curves show no such early behavior. We are forced to conclude, therefore, that on the basis of a die-away measurement alone, it is not possible to distinguish between the case of a two-layered medium and that of a homogeneous medium with properties intermediate between those of the two layers. The above results and conclusion are a consequence of the fact that the die-away technique, involving rather deeply penetrating fast neutrons and gamma rays, averages over a considerable amount of material. This deep averaging capability could be an asset if some auxiliary experiment leads to a determination of the properties of a very shallow layer. If this were true, the die-away expected for a homogeneous medium of that type would be known. Any deviation in the measured die-away would then be due to inhomogeneities in material properties.

#### X. MEASUREMENTS ON A SURFACE IRREGULARITY

It is of interest and importance to find out to what extent an uneven surface will affect the die-away measurement. In practically all remote surface measurements involving a soft-lander, it will be virtually impossible to insure emplacement of the neutron probe on an absolutely level surface.

In order to study this phase of the problem from the standpoint of the die-away technique, we formed a crater in the large tank of crushed granite. The crater was about 45 in. in diameter from rim to rim, 9 in. in height from rim to crater floor, and  $4\frac{1}{2}$  in. in height from rim to surrounding level surface. Two orientations of the neutron probe were used. The first of these, which we call irregularity "A", was such that the probe spanned across the crater with the probe horizontal. Fig. 17 shows the crater and the probe in the "A" position. In irregularity "B", the source-end of the "T" was placed in the bottom of the crater and the stem of the "T" rested on the crater rim.

Figs. 38 and 39 show some of the experimental results. In the  $\text{He}^3$  runs in Fig. 38, a reference run taken on the undisturbed level surface is shown, both as data points and as a fitted smooth curve. The dashed curve obtained with orientation "B" is close to the undisturbed run, but still somewhat different. The dashed and dotted curve for orientation "A" differs from the reference run more than "B". It would seem that any experimental parameter extracted from the  $\text{He}^3$  die-away curves after about channel 50 or 60 would not be sensitive to the presence of the crater, at least for these orientations.

The gamma-ray runs shown in Fig. 39 for the same conditions as the neutron runs show even less sensitivity to probe orientation and surface relief. Considering the statistical uncertainties in the three fitted curves, which may be judged from the set of data points, the three runs may almost be assumed identical.

The fact that the neutron curves show more sensitivity to a surface irregularity and associated probe orientation than do the gamma-ray curves is quite logical. Since the most probable velocity of thermal neutrons at average temperatures is  $0.22 \text{ cm}/\mu\text{sec}$ , any significant air gap which the neutrons must cross to reach the detector will be felt as a disturbing influence. For example, if the detector is 10 cm above the surface at the nearest point, then a minimum time lag of about  $45 \mu\text{sec}$  occurs between the emergence through the surface of a thermal neutron and its subsequent detection. The exact effect of this time lag on the die-away curve is difficult to predict but results generally in a raising of the die-away curve toward later delay times, as observed in Fig. 38. No such time lag exists when gamma rays are being measured since their flight times from originating points to the detector are practically zero on the time scale we are using.

## XI. CYCLIC ACTIVATION RESULTS

At the meeting held at the Sandia Laboratories, 7, 8 February 1967, recommendations to perform specific studies were made to each of the investigating groups. In particular, R. L. Heath recommended that the Mobil Oil Corporation group studying neutron die-away and the Illinois Institute of Technology Research Institute group studying neutron capture gamma rays both perform activation analysis experiments by the cyclic or repetitive activation method described in the paper by Caldwell et al<sup>1</sup>. In this section we discuss the results of the very limited but also very promising cyclic activation studies that time allowed us to make during this contract period.

Calibration, cyclic activation, and natural background gamma-ray spectra are shown in Figs. 40-46. The experimental arrangement was a modification of that used for the die-away experiments shown in Fig. 6. The TMC time analyzer was replaced by a TMC 256-channel pulse-height analyzer which consists of a Model CN110 unit with a Model 210 Pulse-Height plug-in. A further modification of the arrangement shown in Fig. 6 was to feed the delay generator pulse into a Model 531 Tektronix oscilloscope which then generated a 2500  $\mu$ sec gate pulse. This gate pulse was delayed 2000  $\mu$ sec from time zero and was used to gate on the TMC pulse-height analyzer. The timing combination for each cyclic activation run was (100,5000,140,2000,2500) i.e., the fast neutron pulse had a duration of 100  $\mu$ sec, the time zero pulses were separated by 5000  $\mu$ sec, the PM tube was gated off for a 140  $\mu$ sec period encompassing the neutron burst, and there was a delay of 2000  $\mu$ sec following each time zero pulse before the pulse-height analyzer was gated on for 2500  $\mu$ sec. The cyclic activation spectra were obtained then by bombarding the model with fast neutrons for 100  $\mu$ sec, allowing 2000  $\mu$ sec for the die-away of neutron capture gamma rays, and then analyzing the induced plus natural activity for 2500  $\mu$ sec. This cycle was repeated 200 times per sec and for a total time of 30 min. for each run.

The neutron output was about  $1 \times 10^4$  n/burst, which for a 200 pps repetition rate gives an average neutron output of  $2 \times 10^6$  n/sec and about  $4 \times 10^9$  total neutrons per run. These neutron outputs are quite low compared to the neutron outputs required for the more conventional neutron activation techniques.

The following sequence of calibration, measuring natural background activity, and cyclic activation was followed: Calibrate - natural background - calibrate - cyclic activation - calibrate. The timing combination for the calibration and natural background was (0,5000,140,2000,2500) i.e., the same as for the cyclic activation but with no neutron burst. The background runs were 30 min. and the calibration runs were taken for a time sufficient to obtain a good calibration. Both high-energy and low-energy cyclic activation measurements, i.e., measurements where either high-energy or low-energy gamma-rays were of prime interest, were made on the crushed granite and the crushed basalt models. Low-energy runs were made on the models one day and high-energy runs the following day. This procedure allowed adequate time for all induced activities from the low-energy runs to decay before making the high-energy measurements. The high-energy calibration spectrum and calibration curve are shown in Fig. 40 and the low-energy calibration spectrum and calibration curve are shown in Fig. 41. Calibration sources for the high-energy measurements were  $\text{Co}^{60}$  (1.17 and 1.33 Mev) and a Pu-Be neutron source imbedded in a paraffin block. The Pu-Be neutron source imbedded in paraffin gave calibration points at 4.43 Mev, 3.92 Mev, 3.41 Mev (4.43 Mev gamma ray), and 2.23 Mev (hydrogen capture gamma ray). Calibration sources for the low-energy calibration were  $\text{Co}^{60}$  (1.33 Mev and 1.17 Mev),  $\text{Cs}^{137}$  (.662 Mev), and  $\text{Na}^{22}$  (.511 Mev and 1.28 Mev). The high-energy cyclic activation and background spectra for the crushed basalt model are shown in Fig. 42, and the corresponding high-energy spectra for the crushed granite model are shown in Fig. 43. A 6.13 Mev gamma ray which is very intense in the cyclic activation spectrum from both the



crushed basalt and crushed granite models is attributed to the 7.2 sec half-life  $N^{16}$  activity produced by the  $O^{16}(n,p)N^{16}$  reaction. Also rather prominent in both the basalt and granite activation spectra is a 1.78 Mev gamma ray. This gamma ray is attributed to the 2.3 min. half-life  $Al^{28}$  activity produced by the  $Si^{28}(n,p)Al^{28}$  reaction. The 1.78 Mev gamma-ray appears to be more intense in the granite spectrum than in the basalt spectrum. This is in qualitative agreement with the chemical analysis of these rock which showed 33.28 wt. percent Si for the granite and 17.99 wt. percent Si for the basalt. The natural background radioactivity shows gamma rays from Th, U-Ra, and  $K^{40}$ . The 1.46 Mev gamma ray attributed to  $K^{40}$  activity appears to be more intense in the granite background than in the basalt. This, too, is in qualitative agreement with the chemical analysis which showed 2.66 wt. percent K for the granite and 1.61 wt. percent K for the basalt. The low-energy cyclic activation and background spectra for the crushed basalt are shown in Fig. 44 and the corresponding spectra for the crushed granite are shown in Fig. 45. In the natural background spectrum from each model, gamma rays attributable to Th, U-Ra, and  $K^{40}$  activities are present. The 1.46 Mev  $K^{40}$  gamma rays are clearly more abundant in the granite background than in the basalt background.

There are two pronounced gamma ray peaks in the cyclic activation spectra which are from induced activity. These can be more clearly seen in the background-subtracted cyclic activation spectra shown in Fig. 46. The two prominent gamma-ray peaks occur at 0.473 Mev and 1.78 Mev. The 1.78 Mev gamma ray is attributed to the 2.3 min. half-life  $Al^{28}$  activity. We had hoped to see a 0.473 Mev gamma ray from the 0.473 Mev, 19 millisec half-life, isomeric activity of  $Na^{24}$ . Conventional activation methods use the 15.4 hour half-life  $Na^{24}$  activity in analysis for Na, Al, and Mg. Using 14 Mev neutrons both  $Al^{27}$  and  $Mg^{24}$  give a  $Na^{24}$  activity via the  $Al^{27}(n,\alpha)Na^{24}$  and the  $Mg^{24}(n,p)Na^{24}$  reactions.

Our first attempts at looking for the 19 millisecon  $\text{Na}^{24}$  isomeric activity showed a very intense .511 Mev gamma ray with only a bump on the low-energy side. The annihilation radiation was attributed to  $\text{Cu}^{62}$  activity induced via the  $\text{Cu}^{63}(\text{n},2\text{n})\text{Cu}^{62}$  reaction, in the copper neutron attenuator which shields the NaI detector from direct bombardment by 14 Mev neutrons. The copper attenuator was replaced with a Mallory 1000 (tungsten alloy) attenuator and this change eliminated the .511 Mev annihilation gamma rays from the cyclic activation spectra.

Qualitatively the 0.473 Mev gamma ray is more intense in the cyclic activation spectrum from basalt than in the spectrum from granite. Chemical analysis shows .118 gms/cm<sup>3</sup> of Al and .141 gms/cm<sup>3</sup> of Mg in the crushed basalt model and .105 gms/cm<sup>3</sup> of Al and .0012 gms/cm<sup>3</sup> of Mg in the crushed granite model. Clearly the Mg in the granite contributes very little to the 0.473-Mev isomeric activity from  $\text{Na}^{24}$ . Assuming the Mg contribution in the granite as negligible, the intensity of the gamma ray should be about 12% greater from the basalt; however, a very rough analysis shows the 0.473-Mev gamma ray to be about 30% more intense from the basalt model. The ratio of the 1.73 Mev gamma-ray intensity from the crushed basalt model to that from the crushed granite is .60. Chemical analysis gave a value of 0.62 for the ratio of the Si per cm<sup>3</sup> in the crushed basalt to that in the crushed granite. The intensity ratio of the 0.473 Mev gamma rays is believed to be almost equally as good. Hence, the additional intensity of the 0.473-Mev gamma ray over that expected from the greater amount of Al is believed to be a real effect and is attributed to  $\text{Na}^{24}$  produced in the  $\text{Mg}^{24}(\text{n},\text{p})\text{Na}^{24}$  reaction. In future cyclic activation studies, the cyclic activation period is to be followed by a counting period of the residual activity after the  $\text{N}^{16}$  activity has decayed. It is hoped that during this counting period the 0.84-Mev and 1.01-Mev gamma rays

from the 9.5 min. half-life  $\text{Mg}^{27}$  activity produced by the  $\text{A}^{27}(\text{n,p}) \text{Mg}^{27}$  reaction will appear in sufficient intensity to make separate determination of the relative Al, therefore, being able to correct for the Al contribution to the 19 millisecc  $\text{Na}^{24}$  isomeric activity.

These limited cyclic activation studies show that  $\text{O}^{16}$ ,  $\text{Si}^{28}$ , and  $\text{Al}^{27}$  and  $\text{Mg}^{24}$  in combination can be detected by the cyclic activation technique using a low-output neutron source. It is also believed to be very probable that by counting after the cyclic activation period, the separate contributions of  $\text{Al}^{27}$  and  $\text{Mg}^{24}$  to the 0.473 Mev  $\text{Na}^{24}$  isomeric activity can be determined. If this separation is realized, then any combination of  $\text{Si}^{28}$ ,  $\text{O}^{16}$ ,  $\text{Al}^{27}$ , and  $\text{Mg}^{24}$  ratios can be measured in a much shorter period of time and with a much lower output neutron source than is required by conventional activation analysis methods.

## XII. VARIOUS PROBLEMS

In this section we discuss several problems which have arisen during the course of the feasibility studies on the die-away technique. Although all of these have been considered from the standpoint of neutron die-away, most of the problems have a direct and important bearing on other phases of the combination neutron experiment.

With the exception of one test run obtained on concrete (Fig. 9), all gamma-ray die-away runs discussed in the preceding sections were obtained by gating the photomultiplier off during the fast neutron burst. We now discuss why this was necessary. Fig. 47 shows two die-away runs on the solid granite obtained with the NaI/B<sup>10</sup> detector. The solid circles show a run taken with the PM tube gated, whereas the open circles are the data for a corresponding ungated run. The timing conditions were (100,5000,140,4680,16) and (100,5000,0,4680,16), respectively. The data points for the ungated run during the burst are non-zero but have been omitted because they are not valid. Both runs were for 30 min. and the neutron output was about  $1 \times 10^4$  neutrons/burst for the ungated run and somewhat higher for the gated run. The striking thing about the data is the fact that the decay for the gated run is smooth with apparently only minor statistical variations. The decay for the ungated run, however, is not absolutely smooth, there being definite indications of wave-like distortions in at least two regions of the data. It would clearly be difficult, if even possible, to extract correct experimental parameters from such a distorted curve.

The effect illustrated in Fig. 47 was obtained on other models and with a completely different detector, type of PM tube, preamplifier, amplifier, and discriminator. Since the difficulty disappears upon gating the PM tube off during the burst, we tentatively conclude that the trouble lies in some kind of temporary overload paralysis produced in the PM tube by the very intense radiation existing during the burst.

Fig. 48 shows a comparison of two neutron die-away runs taken on the brick model, for burst lengths of 10 and 100  $\mu$ sec. The timing combinations were (100,5000,0,4680,16) for the upper curve and (10,2500,0,2180,16) for the lower curve. Both runs were for 30 min. and for the same instantaneous neutron output during the burst. When account is taken of the fact that half as many bursts are in the upper run as the lower, the gain in counting rate in going to the longer burst is about a factor of 10, the ratio of the burst lengths. The increase in counting rate is linear because the saturation point has still not been reached even for the 100- $\mu$ sec burst. Use of a much longer burst than 100  $\mu$ sec would not result in a proportionate increase in count rate because the saturation value would soon be reached. Even though it is unlikely that the neutron source in the combination neutron experiment package will have a 100- $\mu$ sec burst available, it was decided to use this burst length in the feasibility studies to aid in optimizing the data taking. From the standpoint of only the die-away and capture gamma-ray spectrum measurements, a burst length of 100  $\mu$ sec is probably about optimum.

The next two problems to be discussed are directly related to the capture gamma-ray spectrum portion of the combination experiment. The first of these is the matter of what thermal neutron absorber should be used around the NaI. For these feasibility studies we used  $B^{10}$ . This allowed us to obtain gamma-ray die-away data which we had thought might be somewhat different from those obtained with an integral bias. As stated in a previous section, there seems to be very little difference between the two types of gamma-ray curves. With an integral bias set low, i.e., below the energy of the 478-keV line from the  $B^{10}(n, \alpha) Li^7$  reaction, the gamma-ray die-away benefits by virtue of a somewhat greater counting rate from this contribution. The gain is not great, however. The presence of the 478-keV line in the capture gamma-ray

spectrum does constitute an interference for that measurement. Since there is no particular advantage to the die-away if  $B^{10}$  is used, we have decided that future experiments will be carried out with  $Li^6$ , in the form of lithium fluoride, as the neutron absorber. No interfering gamma rays are produced when a thermal neutron is absorbed by  $Li^6$ .

The second of the two problems mentioned above is much more serious and cannot be immediately solved. Early in the feasibility studies at IIT Research Institute, it became apparent that the capture gamma-ray spectrum measurement would be difficult to carry out without some neutron moderator partially surrounding the source. We subsequently made some tests to determine how much effect a small amount of moderator would have on the neutron die-away measurement. Two paraffin slabs were formed, each of thickness 7.5 cm. One slab was 24 cm x 24 cm, and the other was 24 cm x 10 cm. The slabs were joined at right angles to form an "L", and this was inverted and placed over the Philips neutron tube such that the large slab was over the target, and the small slab was on the side of the target opposite to the detector. Comparison runs were taken on the crushed granite model with and without the moderator in place. Fig. 49 shows such a comparison for the bare  $He^3$  detector. The curves have been normalized in the asymptotic region around channel 110-120. Clearly, 7.5 cm of paraffin has a very large effect on the die-away for about 70 channels, or about 1100  $\mu$ sec. Following this time, the two die-away curves seem to be on the same kind of die-away. It is probably not feasible to extract good parameters from the die-away curve after a delay of the order of 1000  $\mu$ sec. We, therefore, conclude on the basis of this test that 7.5 cm of paraffin would be too much to allow the thermal die-away measurements to be made.

A similar test was performed with the  $He^3/Cd$  detector, and these results are shown in Fig. 50. The channel length was 0.5  $\mu$ sec, and data from trios of successive channels have been combined for plotting.

The curves have been normalized in the asymptotic region. As in the thermal case the moderator influences the die-away until the asymptotic region is reached. With 7.5 cm of paraffin it would be difficult to get good epithermal parameters from the data.

A final problem which bears on the entire combination experiment is that of probe orientation. We have performed many of the die-away studies with both horizontal and vertical orientation, and Figs. 51 and 52 show two examples. In Fig. 51,  $\text{He}^3$  die-away curves are shown which were obtained on the granite block. The data have been normalized during the burst. The die-away rate with vertical positioning is much slower than with horizontal. The explanation for this is the same as for the difference observed in the surface irregularity experiment. Lag flight times for thermal neutrons cause the data for vertical orientation to be held up at long delay times. The minimum flight time in this case is about 120  $\mu\text{sec}$ . Fig. 52 shows a similar comparison for gamma-ray die-away on crushed basalt. The difference between the two orientations is much smaller for gamma rays, but still some residual effect remains. This may be due to a real difference in the gamma-ray die-away rates for these two configurations and may be at least partly due to the fact that at 122-kev bias, some thermal neutron component is present from the  $\text{B}^{10}$  capture contribution.

Both sets of curves in Figs. 51 and 52 have been normalized, so relative counting rates for the two orientations are not apparent. From the run data in both cases the counting rates for horizontal orientation are about 2 to 3 times higher than those for vertical. Thus, from the standpoint of both counting rate and interfering effects due to flight time delays, it would seem that horizontal orientation is preferred over vertical orientation for the neutron die-away measurement.

## REFERENCES

1. R. L. Caldwell, W. R. Mills, L. S. Allen, P. R. Bell, R. L. Heath, "Combination Neutron Experiment for Remote Analysis", *Science* 152, 457-65 (1966).
2. R. Monaghan, A. H. Youmans, R. A. Bergan, E. C. Hopkinson, "Instrumentation for Nuclear Analysis of the Lunar Surface", *IEEE Trans. Nucl. Sci.* 10, 183-9 (1963).
3. J. I. Trombka and E. A. Metzger, "Neutron Methods for Lunar and Planetary Surface Compositional Studies", *Analysis Instrumentation 1963*, 237-50, Plenum Press, N.Y. (1963).
4. K. H. Beckurts and K. Wirtz, Neutron Physics, Springer-Verlog New York Inc. (1964).
5. I. N. Sneddon, Fourier Transforms, McGraw-Hill (1951).
6. J. H. Reed, "Compositional Analysis of Lunar and Planetary Surfaces Using Neutron Capture Gamma Rays", Report No. IITRI - A6155-2, June 1 - Nov. 1, 1966.
7. W. R. Mills, L. S. Allen, F. Selig, R. L. Caldwell, "Neutron and Gamma-Ray Die-Away in a Heterogeneous System", *Nuclear Applications* 1, 312-21 (1965).
8. D. J. Behrens, "Some Notes on the Nature of Experiments, on the Statistics of Counting, and on the Fitting of Exponential Decay to the Results of Counting Experiments", AERE T/R 629 (Atomic Energy Research Establishment, Harwell, Berks., England, 1951).
9. F. Aigner and L. Flamm, "Analyse von Abklingungskurven", *Physik. Zeitschr.* XIII, 1151-5 (1912).
10. R. G. Cornell, "A New Estimation Procedure for Linear Combinations of Exponentials", ORNL-2120 (1956).
11. CO-OP Class/Index Code E2 WISC GAUSHAUS, "Non-linear Least Squares (GAUSHAUS)", contributed by University of Wisconsin Computing Center.
12. Chart of the Nuclides, KAPL, Seventh Ed. (June, 1964).
13. "Neutron Cross Sections", Supp. No. 2 to BNL-325, Second Edition, Vol. 1, Z = 1 to 20 (May, 1964).



## APPENDIX

The steady-state age equation to be solved is

$$\frac{1}{r} \frac{\partial}{\partial r} \left( r \frac{\partial q}{\partial r} \right) + \frac{\partial^2 q}{\partial z^2} + \frac{s \delta(r) \delta(z-d) \delta(\theta)}{2 \pi r} = \frac{\partial q}{\partial \theta} \quad (A1)$$

The method used to solve Eq (A1) is to take the Laplace transform with respect to  $\theta$ , the Hankel transform with respect to  $r$ , and the Fourier sine transform with respect to  $z$ . Define the multiple transform of  $q$  as

$$q^{\text{LHF}} = \sqrt{\frac{2}{\pi}} \int_0^{\infty} \sin k z \, dz \int_0^{\infty} r J_0(\xi r) \, dr \int_0^{\infty} e^{-p\theta} q(r, z, \theta) \, d\theta$$

When an inverse transform is taken, this will be indicated by the absence of that particular superscript on  $q$ .

Taking the LHF transform of Eq(A1) and using well known properties of the Laplace, Hankel, and Fourier transforms, we obtain the transformed equation

$$(k^2 + \xi^2 + p) q^{\text{LHF}} = \frac{s}{2\pi} \sqrt{\frac{2}{\pi}} \sin k d \quad (A2)$$

so that

$$q^{\text{LHF}} = \frac{s}{2\pi} \sqrt{\frac{2}{\pi}} \frac{\sin k d}{k^2 + \xi^2 + p} \quad (A3)$$

From an elementary table of Laplace transforms we have that

$$q^{\text{HF}} = \frac{s}{2\pi} \sqrt{\frac{2}{\pi}} e^{-(k^2 + \xi^2)\theta} \sin k d \quad (A4)$$

The inverse Hankel transform is

$$q^{\text{F}} = \frac{s}{2\pi} \sqrt{\frac{2}{\pi}} e^{-k^2\theta} \sin k d \int_0^{\infty} \xi e^{-\theta\xi^2} J_0(r\xi) \, d\xi \quad (A5)$$

From an advanced table of integrals, one can find that

$$\int_0^{\infty} \xi e^{-\theta\xi^2} J_0(r\xi) \, d\xi = \frac{1}{2\theta} e^{-\frac{r^2}{4\theta}}$$

Thus

$$q^F = \frac{S}{4\pi\theta} \sqrt{\frac{2}{\pi}} e^{-\frac{r^2}{4\theta}} e^{-\theta k^2} \sin kd \quad (A6)$$

and

$$q = \frac{S}{4\pi\theta} \sqrt{\frac{2}{\pi}} e^{-\frac{r^2}{4\theta}} \sqrt{\frac{2}{\pi}} \int_0^\infty e^{-\theta k^2} \sin kz \sin kd \, dk \quad (A7)$$

The advanced table of integrals gives

$$\int_0^\infty e^{-\theta k^2} \sin kz \sin kd \, dk = \frac{1}{4} \sqrt{\frac{\pi}{\theta}} \left[ e^{-\frac{(z-d)^2}{4\theta}} - e^{-\frac{(z+d)^2}{4\theta}} \right]$$

so that we finally have

$$q(r, z, \theta) = \frac{S}{(4\pi\theta)^{3/2}} e^{-\frac{r^2}{4\theta}} \left[ e^{-\frac{(z-d)^2}{4\theta}} - e^{-\frac{(z+d)^2}{4\theta}} \right] \quad (A8)$$

The equation for the thermal neutron density is

$$vD \left[ \frac{1}{r} \frac{\partial}{\partial r} \left( r \frac{\partial n}{\partial r} \right) + \frac{\partial^2 n}{\partial z^2} \right] - v\Sigma_a n = \frac{\partial n}{\partial t} \quad (A9)$$

Taking the Laplace transform with respect to  $t$ , the Hankel transform with respect to  $r$ , the Fourier sine transform with respect to  $z$ , and making use of the properties of these transforms and the boundary and initial conditions Eq(6)-(8), we obtain the transformed equation

$$\left[ vD (k^2 + \xi^2) + p + v\Sigma_a \right] n^{LHF} = \frac{S}{2\pi} \sqrt{\frac{2}{\pi}} e^{-(k^2 + \xi^2)\theta} \sin kd \quad (A10)$$

so

$$n^{LHF} = \frac{S}{2\pi} \sqrt{\frac{2}{\pi}} \frac{e^{-(k^2 + \xi^2)\theta} \sin kd}{v \left[ \Sigma_a + D(k^2 + \xi^2) \right] + p} \quad (A11)$$

Taking the inverse Laplace transform we get

$$\begin{aligned} n^{HF} &= \frac{S}{2\pi} \sqrt{\frac{2}{\pi}} e^{-(k^2 + \xi^2)\theta} e^{-v \left[ \Sigma_a + D(k^2 + \xi^2) \right] t} \sin kd \quad (A12) \\ &= \frac{S}{2\pi} \sqrt{\frac{2}{\pi}} e^{-v \Sigma_a t} e^{-(k^2 + \xi^2)(\theta + vDt)} \sin kd \end{aligned}$$

This is exactly Eq.(A4) with  $\theta$  replaced by  $\theta + vDt$ .

Therefore, the steps which led up to Eq.(A8) may be repeated, which allows us to immediately write the inverse of  $n^{HF}$ , namely the solution we seek:

$$n(r, z, t) = \frac{S e^{-\left[ v \Sigma_a t + \frac{r^2}{4(\theta + vDt)} \right]}}{\left[ 4 \pi (\theta + vDt) \right]^{3/2}} \left\{ e^{-\frac{(z-d)^2}{4(\theta + vDt)}} - e^{-\frac{(z+d)^2}{4(\theta + vDt)}} \right\} \quad (A13)$$

TABLE 1 - RESULTS OF THEORETICAL  
CALCULATIONS ON MODEL SIZES

Density (gm/cm <sup>3</sup> )	$n_Y/n_Y^{\infty}$	D (cm)	H (cm)
1.40	0.90	272	127
	0.95	320	153
	0.98	370	178
	0.99	400	195
2.00	0.90	200	96
	0.95	232	113
	0.98	265	133
	0.99	296	144
2.65	0.90	152	68
	0.95	176	82
	0.98	202	100
	0.99	218	110

TABLE 2 - COMPARISON OF CHEMICAL ANALYSES

	Brick	Carbonate Rock (Demarco Black)	Crushed Granite (Burnet Red)	Solid Granite (Texas Rockville)	Crushed Basalt (Knippa)
$\text{SiO}_2$	59.45 56.26	26.78 23.88	72.68 71.18	68.25 69.84	44.10 38.48
$\text{Al}_2\text{O}_3$	15.02 16.48	0.12 0.65	13.62 13.94	15.90 14.69	9.90 13.72
$\text{Fe}_2\text{O}_3$	6.32 6.73	0.62 0.23	0.69 3.74	0.93 4.63	4.08 14.08
$\text{FeO}$	0.06 -	0.19 -	1.91 -	2.80 -	7.14 -
$\text{CaO}$	12.86 11.25	40.72 40.57	1.45 1.16	2.09 1.38	12.92 12.44
$\text{MgO}$	1.24 2.65	0.43 0.72	0.09 0.13	0.01 0.07	13.52 14.39
$\text{Na}_2\text{O}$	1.43 1.92	0.51 0.12	3.60 4.84	3.60 4.94	3.03 2.72
$\text{K}_2\text{O}$	2.10 2.40	0.07 0.04	4.80 3.20	5.33 3.30	1.39 1.94
$\text{Li}_2\text{O}$	0.20 0.0042	0.18 0.0006	0.28 0.0029	0.29 0.0021	0.22 0.0037
$\text{B}_2\text{O}_3$	0.005 0.012	0.001 0.003	0.001 0.0010	0.001 0.0012	0.001 0.002

Note: Upper number from Spectrochemical Laboratories, Inc.; lower number from Metallurgical Laboratories, Inc.

TABLE 3 - ELEMENTAL WEIGHT PERCENT FROM  
ANALYSES OF METALLURGICAL LABORATORIES, INC.

	Brick	Carbonate Rock (Demarco Black)	Crushed Granite (Burnet Red)	Solid Granite (Texas Rockville)	Crushed Basalt (Knippa)
Si	26.30	11.16	33.28	32.65	17.99
Al	8.72	0.344	7.38	7.77	7.26
Fe	4.71	0.161	2.62	3.24	9.85
Ca	8.04	29.00	0.829	0.986	8.89
Mg	1.60	0.434	0.0784	0.0422	8.68
Na	1.42	0.0890	3.59	3.66	2.02
K	1.99	0.0332	2.66	2.74	1.61
Li	0.00195	0.000279	0.00135	0.000975	0.00172
B	0.00373	0.000932	0.000310	0.000373	0.000621

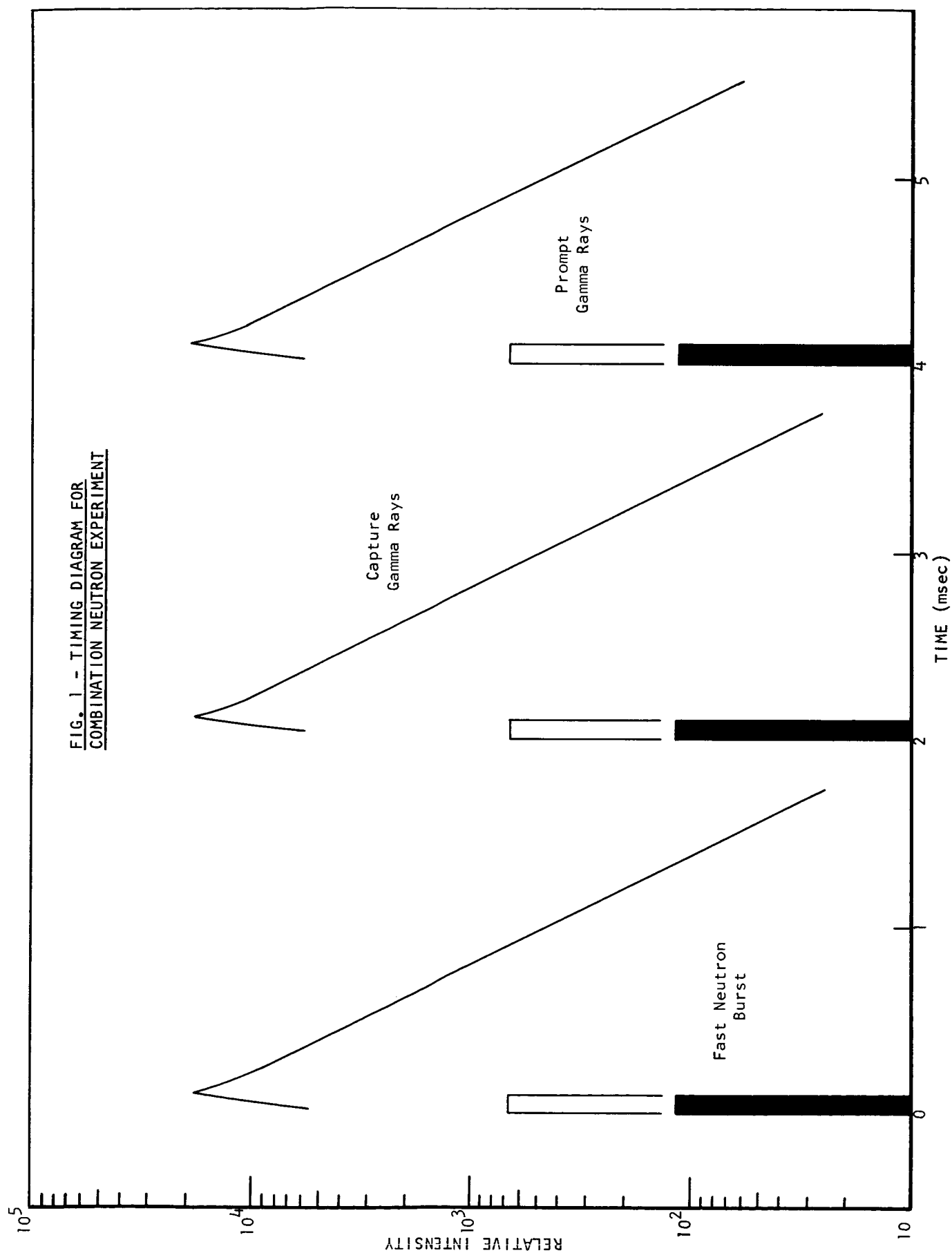
TABLE 4 - ELEMENTAL THERMAL NEUTRON  
ABSORPTION PARAMETER

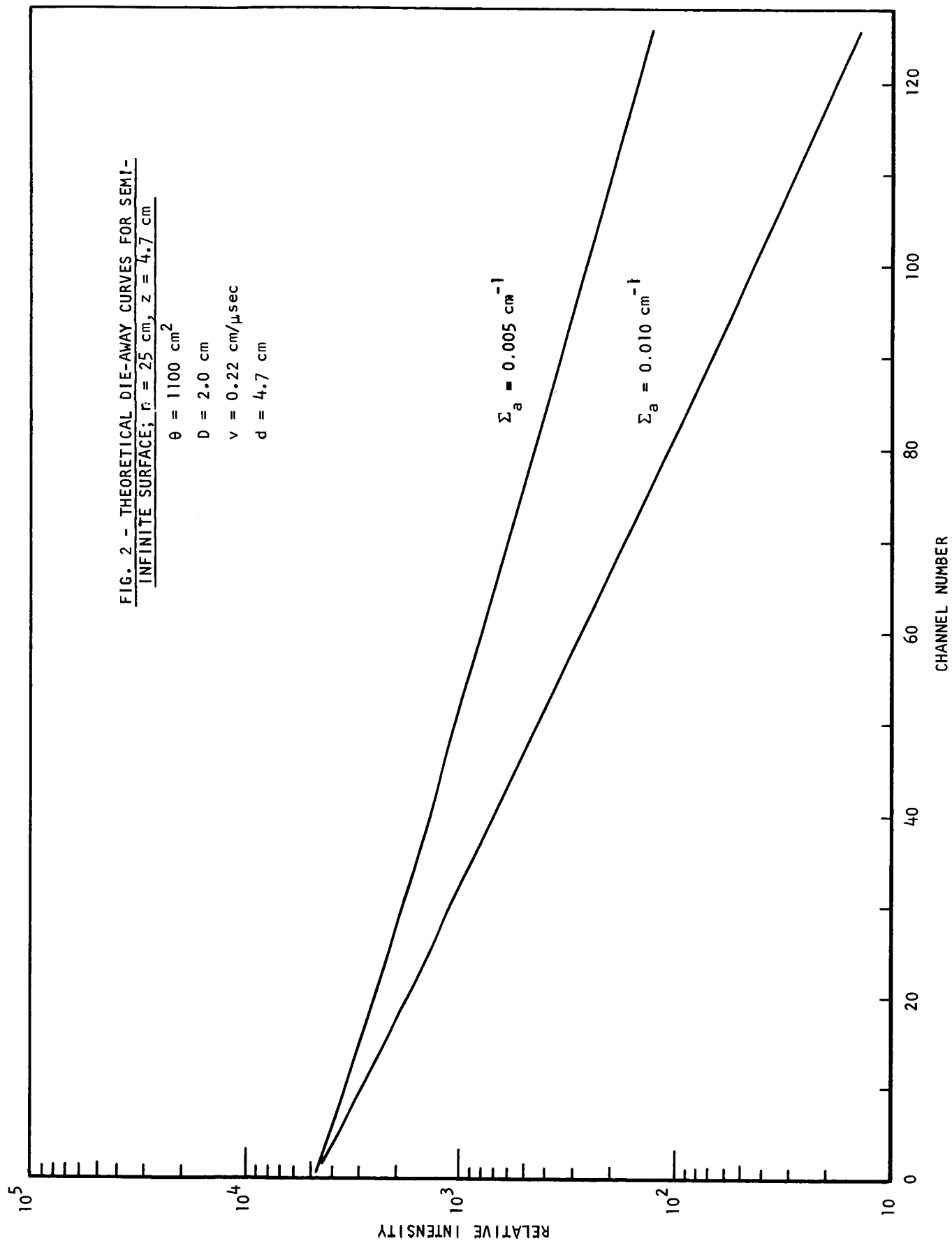
<u>Element</u>	<u><math>(\sigma_a/A) \times 10^3</math></u>
Si	5.70
Al	8.71
Fe	46.5
Ca	10.7
Mg	2.59
Na	23.2
K	53.7
Li	10200
B	70200

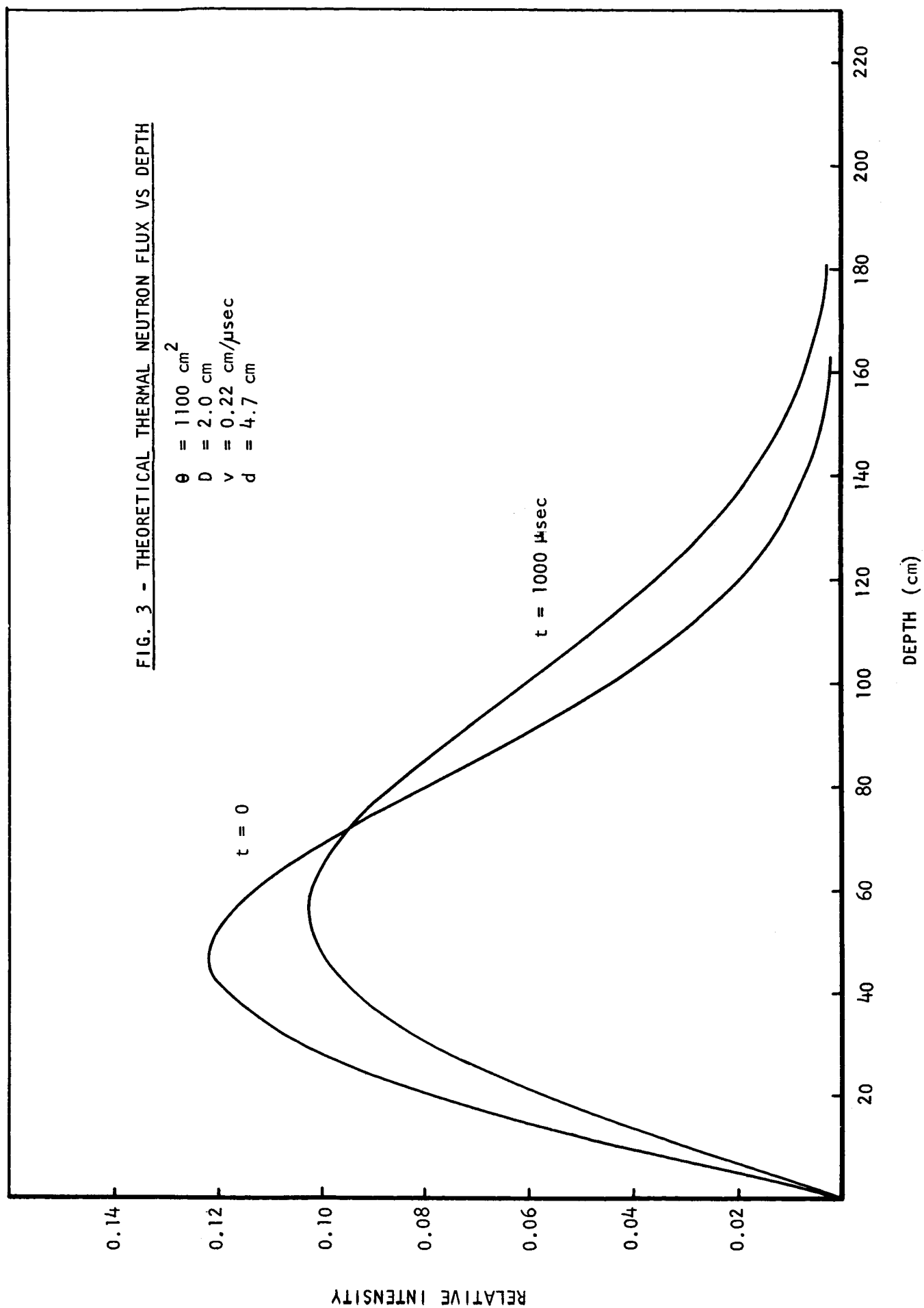
TABLE 5 - THERMAL NEUTRON PARAMETERS  
FOR ROCK MODELS

Rock Type	$\rho$ (gm/cm <sup>3</sup> )	$\Sigma a/\rho$	$\Sigma a$
Brick	1.71	0.00576	0.00985
Carbonate	1.31	0.00276	0.00362
Crushed Granite	1.42	0.00389	0.00552
Solid Granite	2.63	0.00411	0.01081
Crushed Basalt	1.62	0.00564	0.00913









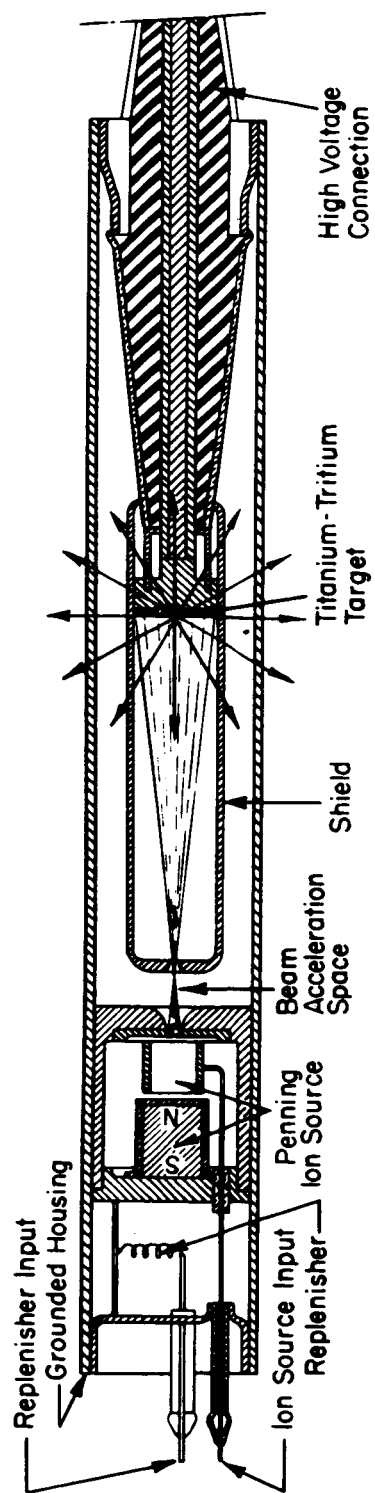


FIG. 4 - PHILIPS NEUTRON TUBE

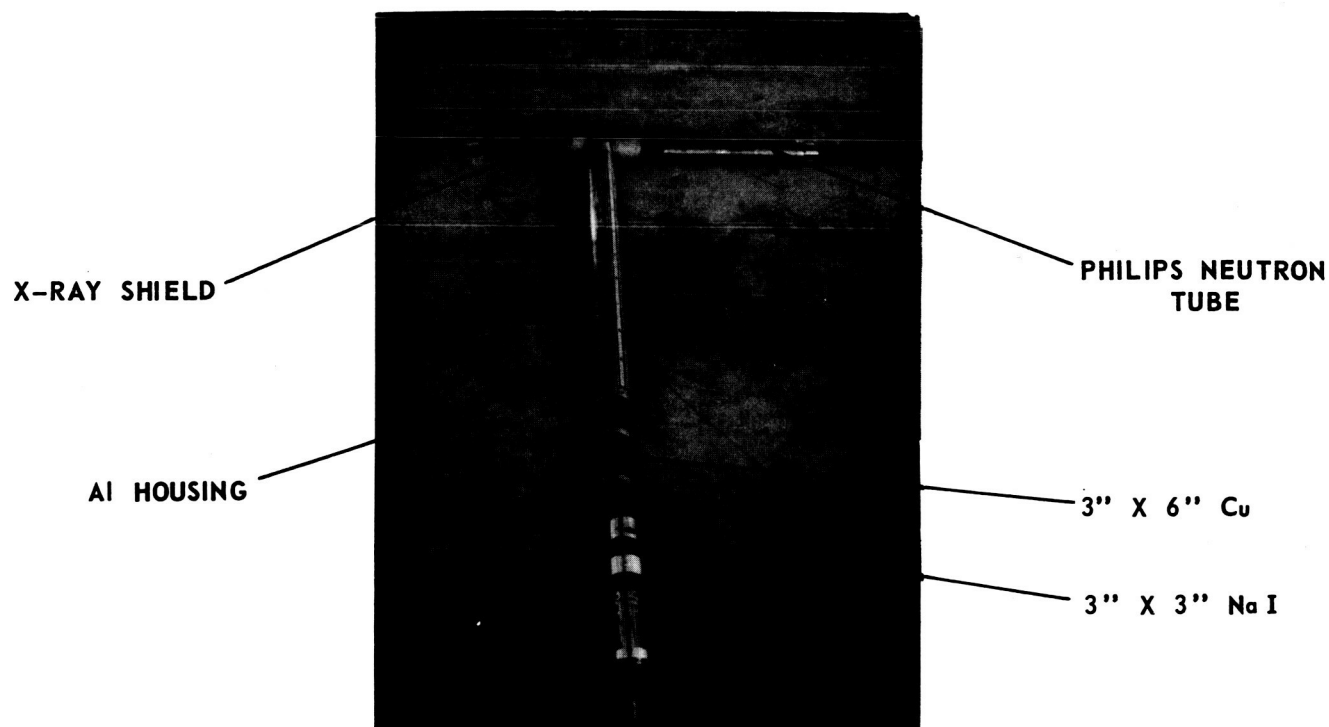


FIG. 5 - EXPLODED VIEW OF  
DIE-AWAY PROBE

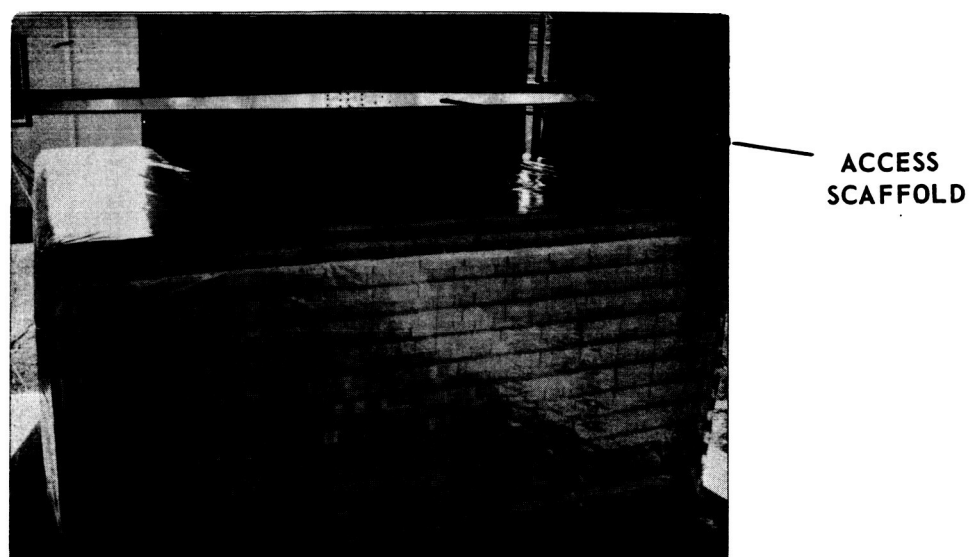


FIG. 8 - DRY CLAY BRICK ASSEMBLY

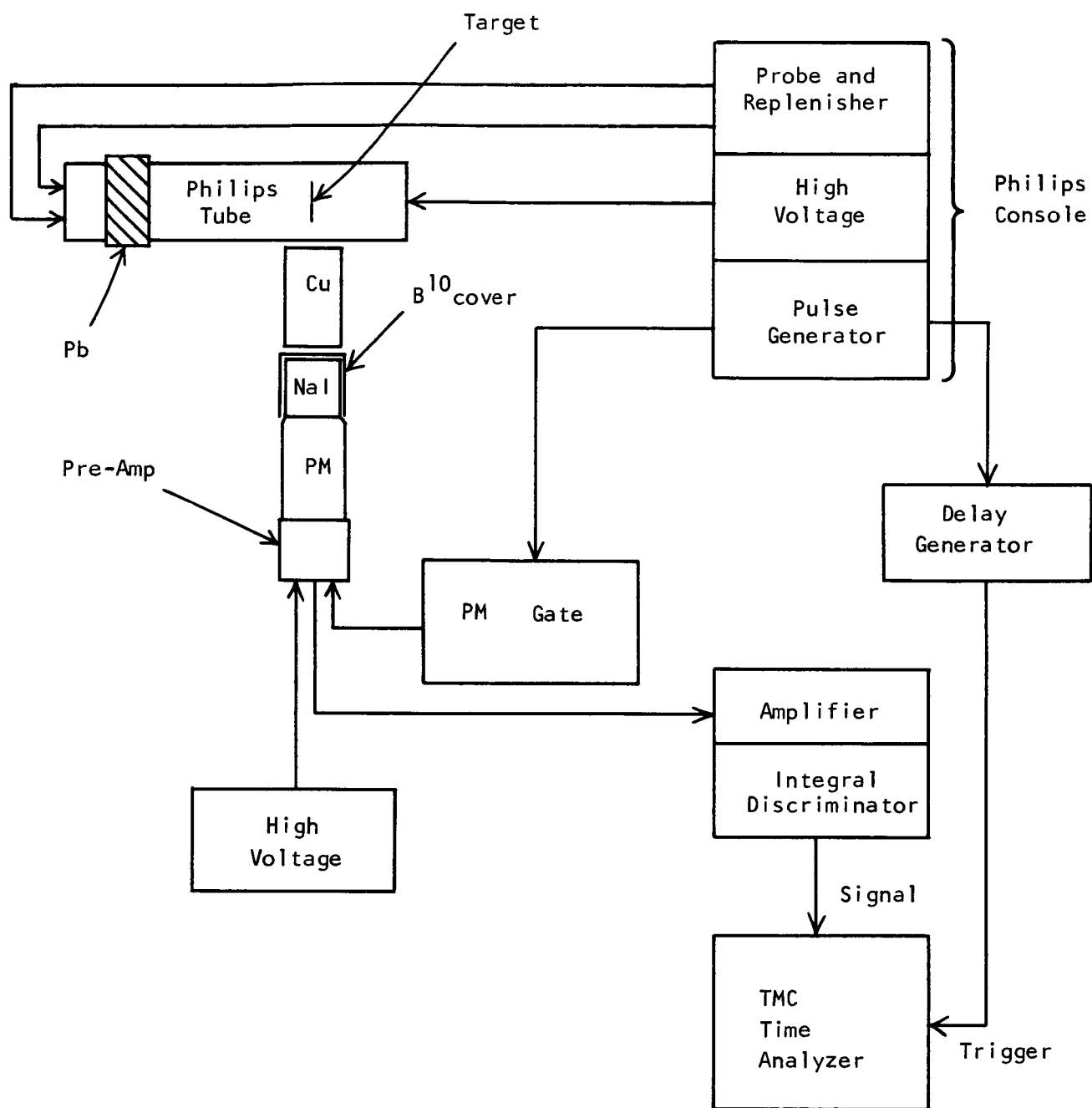


FIG. 6 - BLOCK DIAGRAM OF DIE-AWAY EXPERIMENT

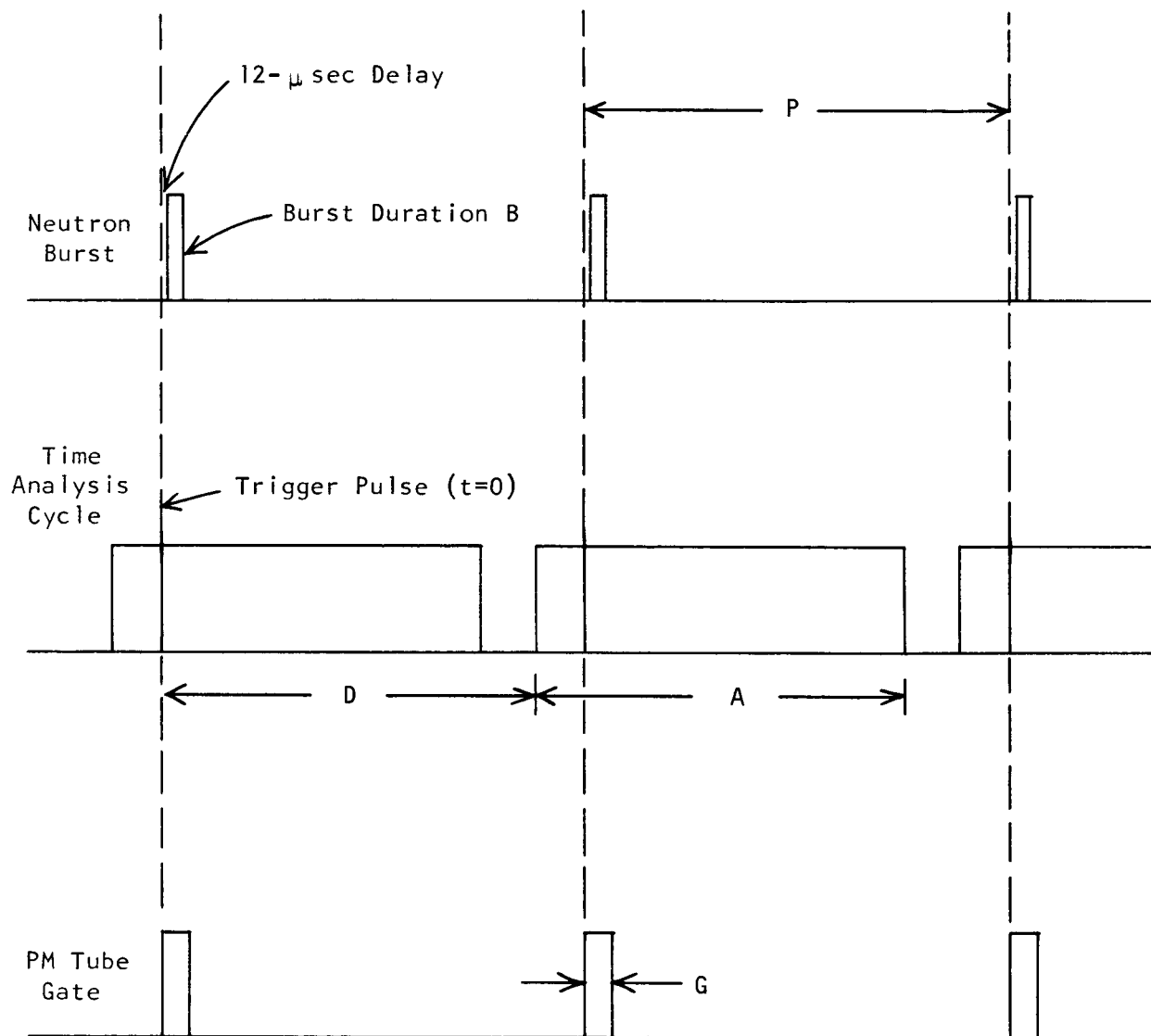
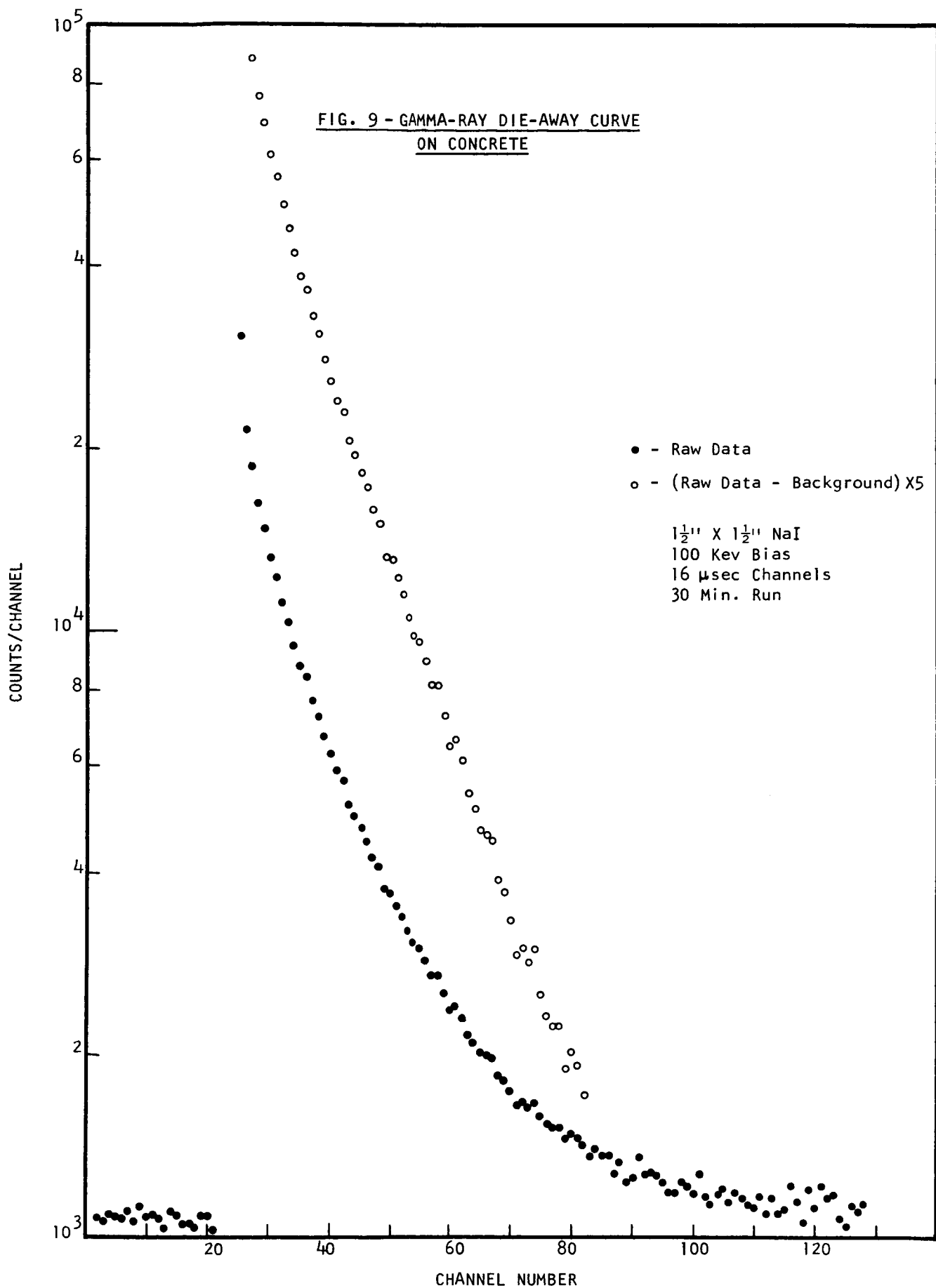
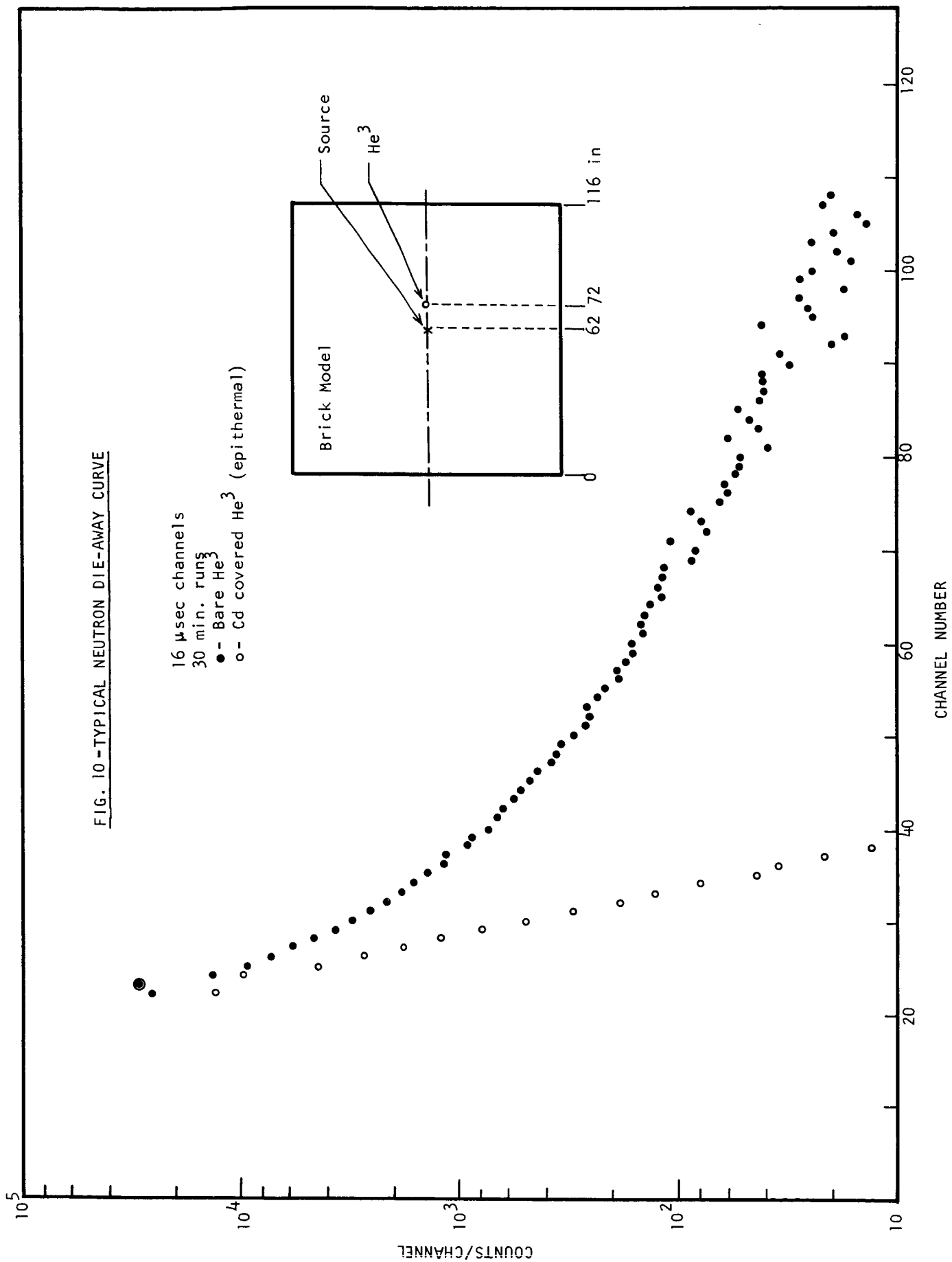
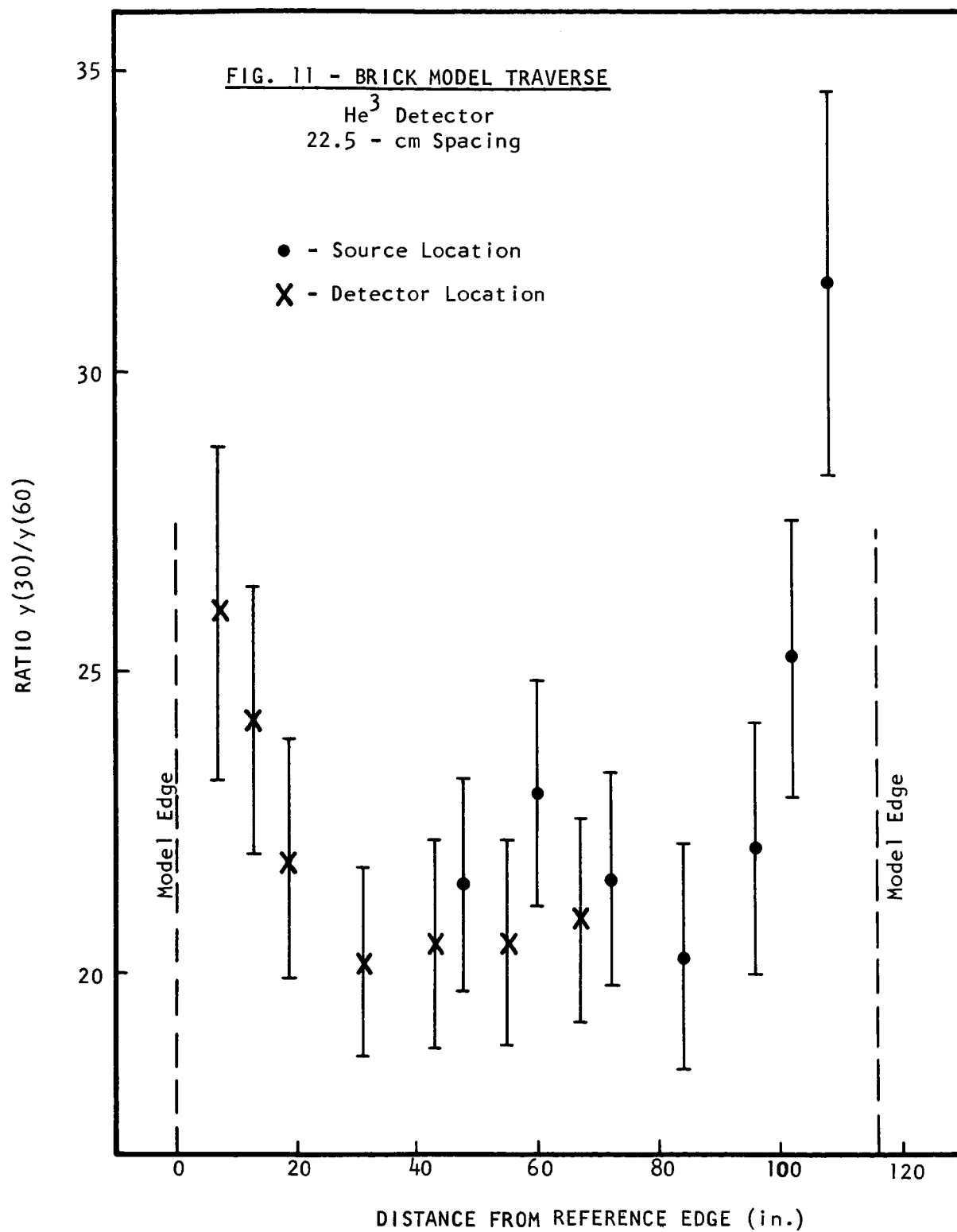


FIG. 7 - TIMING SEQUENCE FOR  
DIE-AWAY EXPERIMENTS









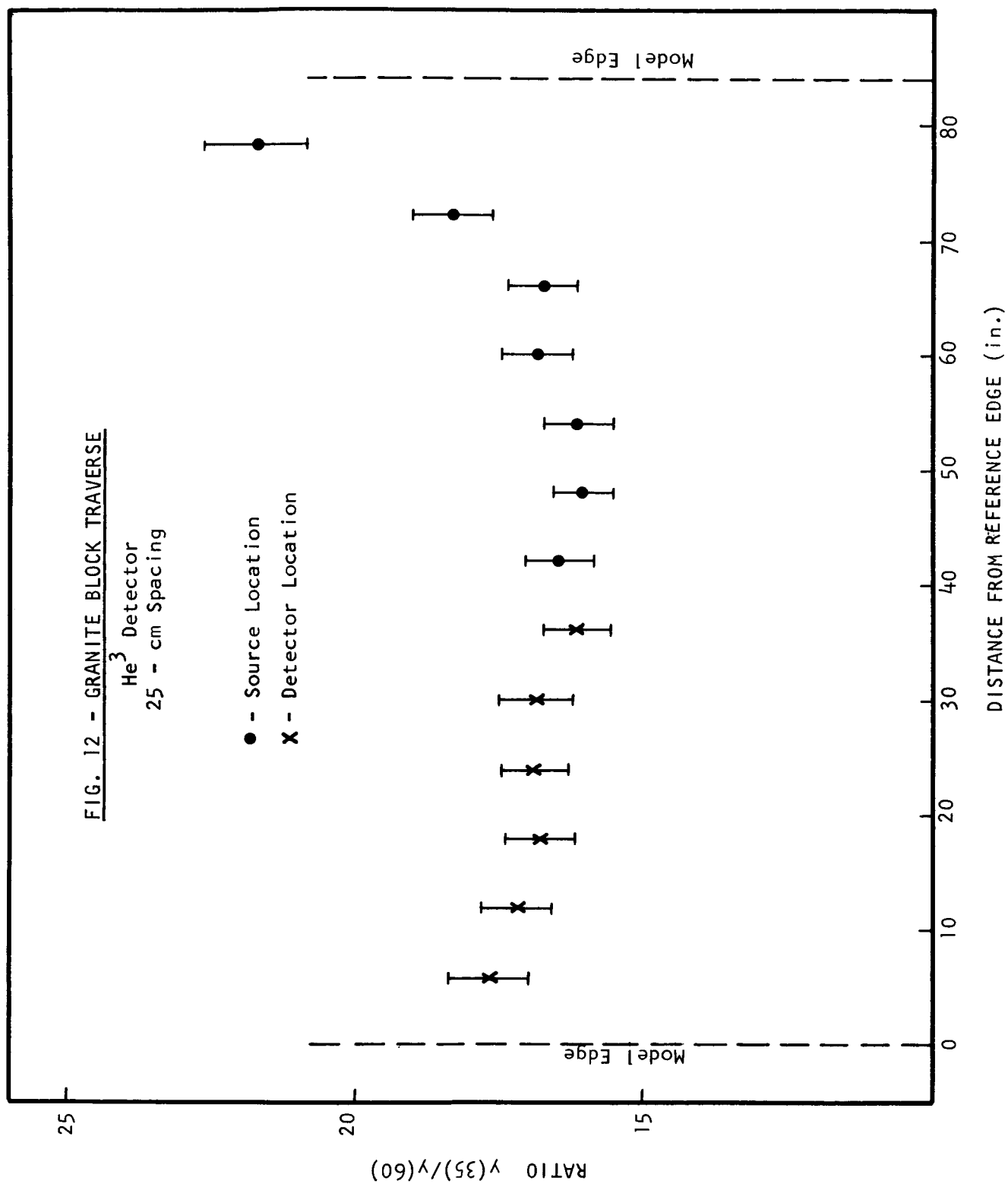
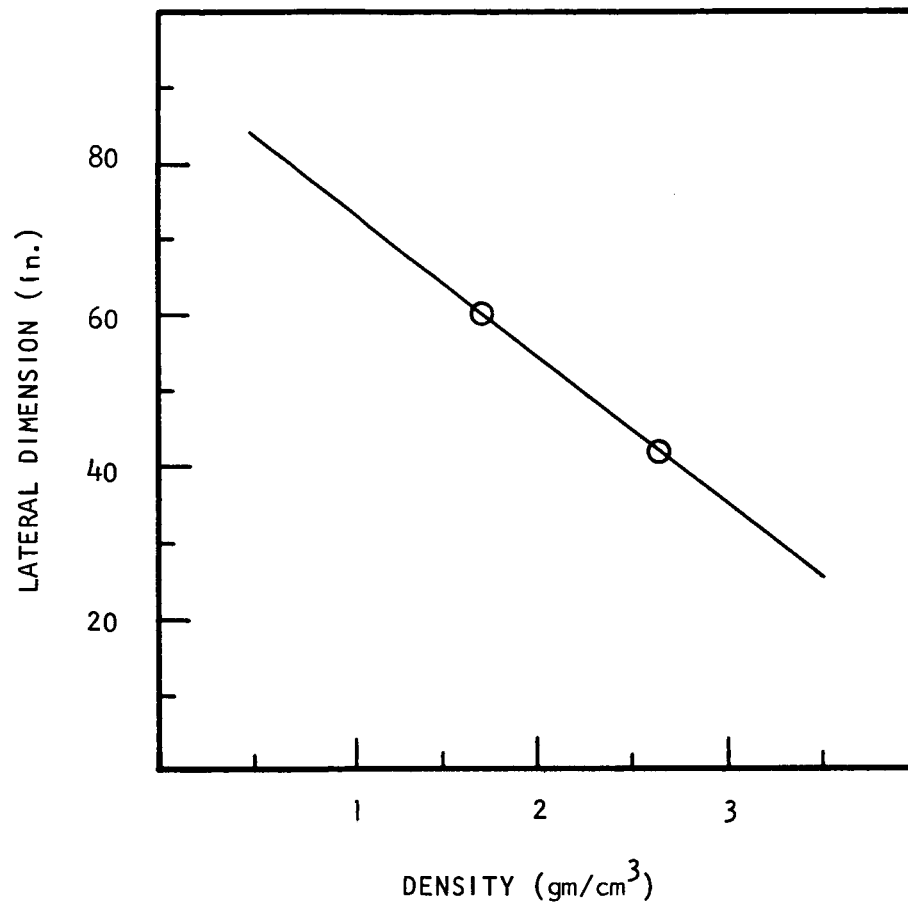


FIG. 13 - REQUIRED LATERAL DIMENSIONS  
FOR "SEMI-INFINITE" MODELS  
FOR 25-cm SOURCE-DETECTOR SPACING



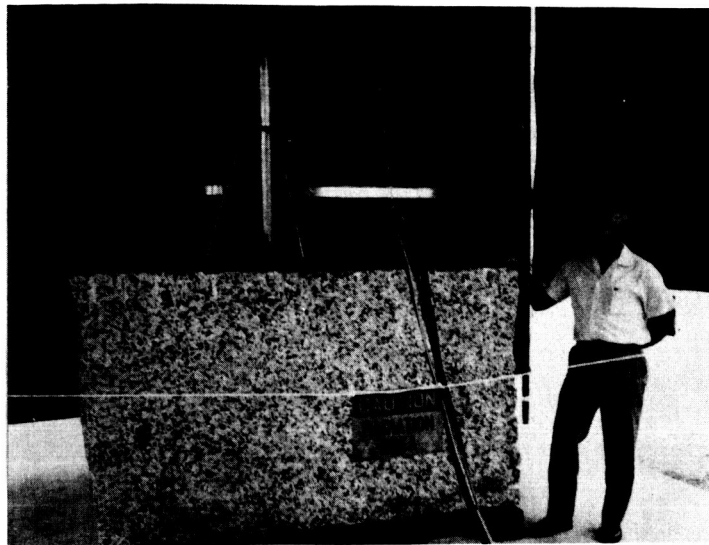


FIG. 14 - DENSE GRANITE MODEL

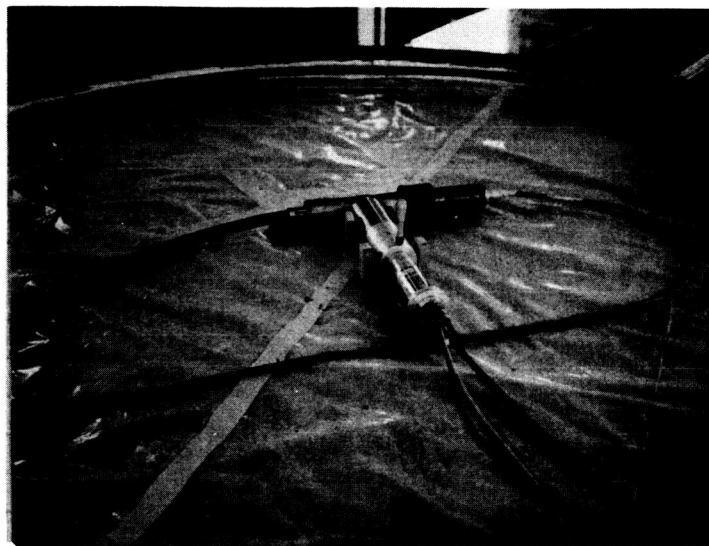


FIG. 15 - CRUSHED ROCK MODEL



FIG. 16 - LAYERED MODEL

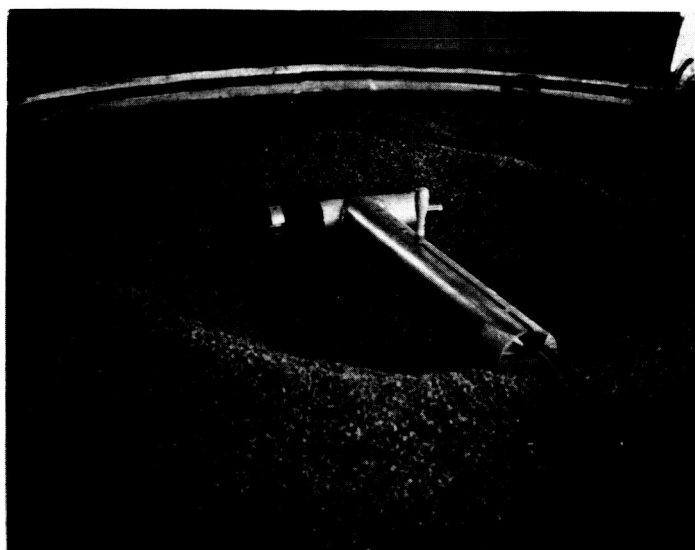


FIG. 17 - SURFACE IRREGULARITY "A"

FIG. 18 - THERMAL NEUTRON DIE-AWAY

Crushed Basalt

He<sup>3</sup> Detector

25-cm Spacing

Raw Data

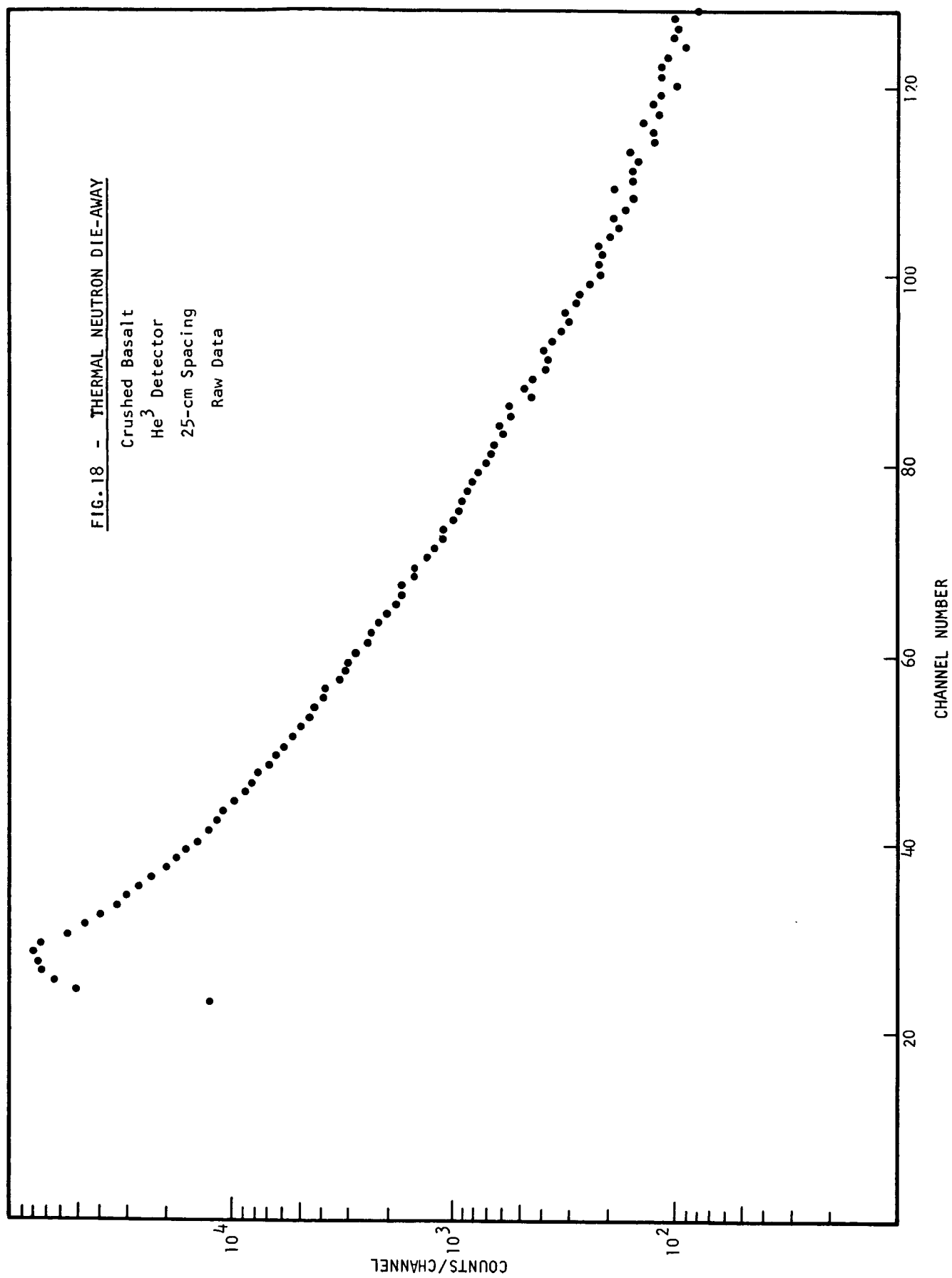


FIG. 19 - THERMAL NEUTRON DIE-AWAY

Crushed Granite

He<sup>3</sup> Detector

25-cm Spacing

Raw Data

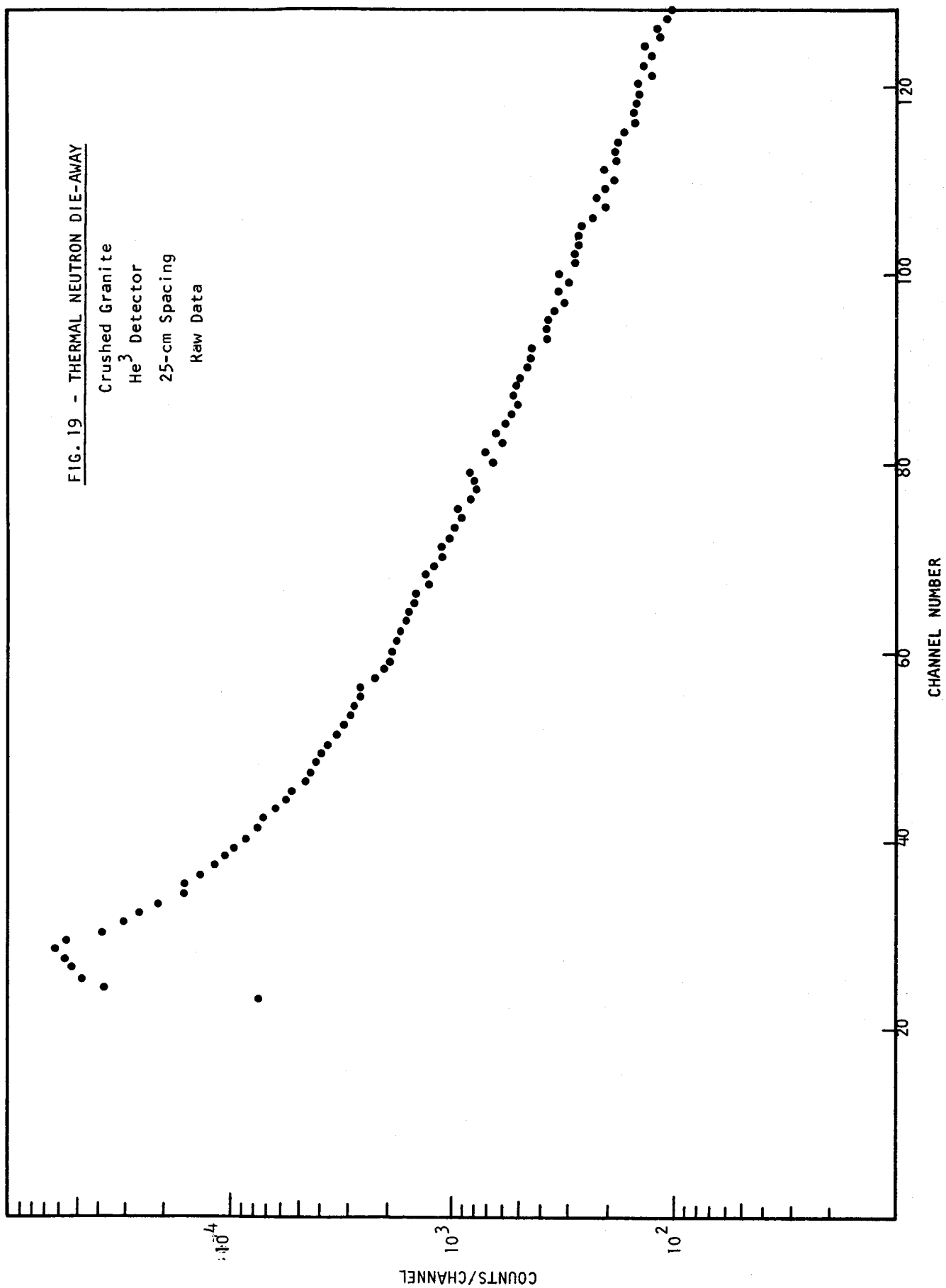




FIG. 20 - THERMAL NEUTRON DIE-AWAY

Solid Granite  
 $\text{He}^3$  Detector  
25-cm Spacing  
Raw Data

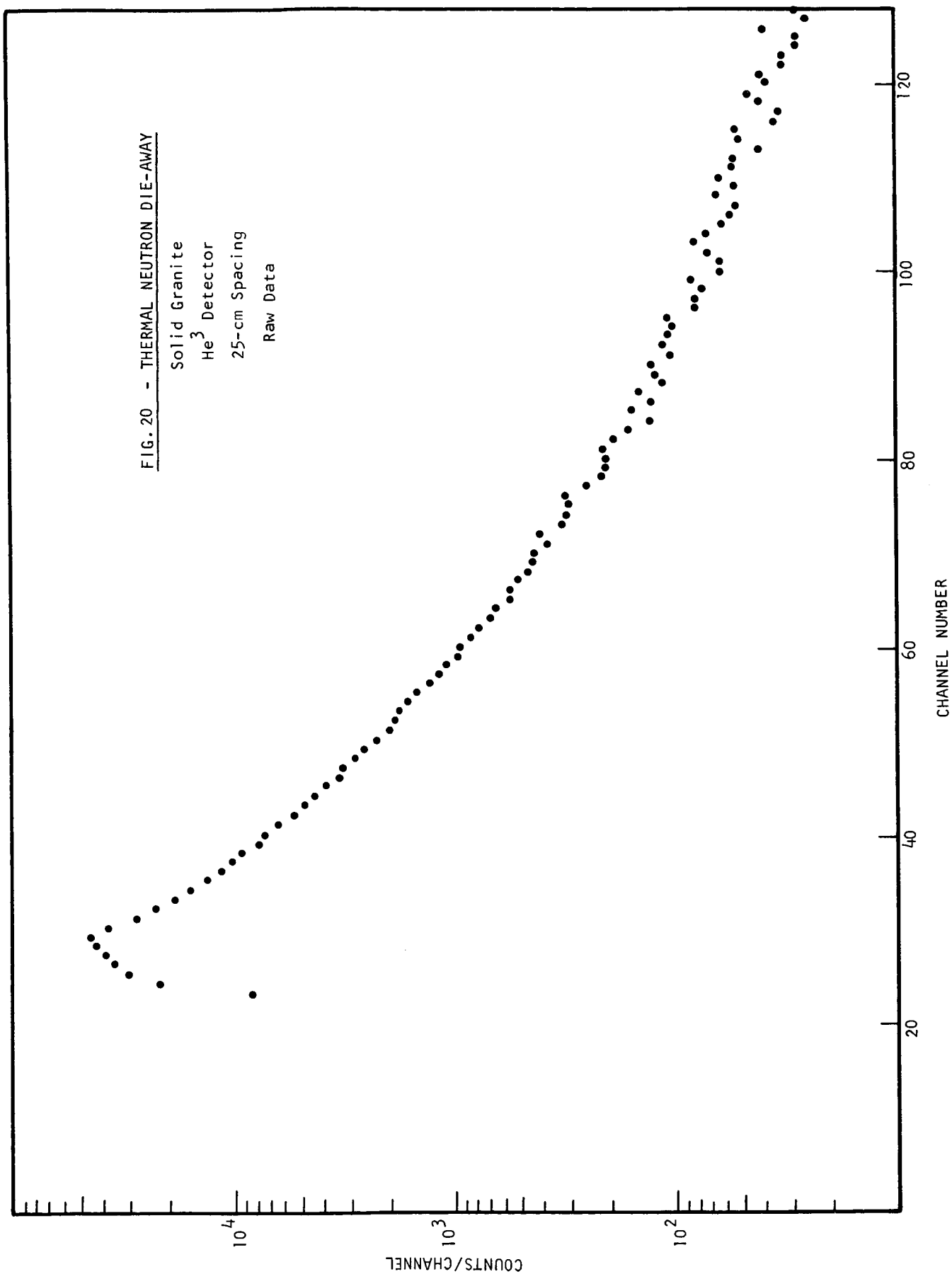


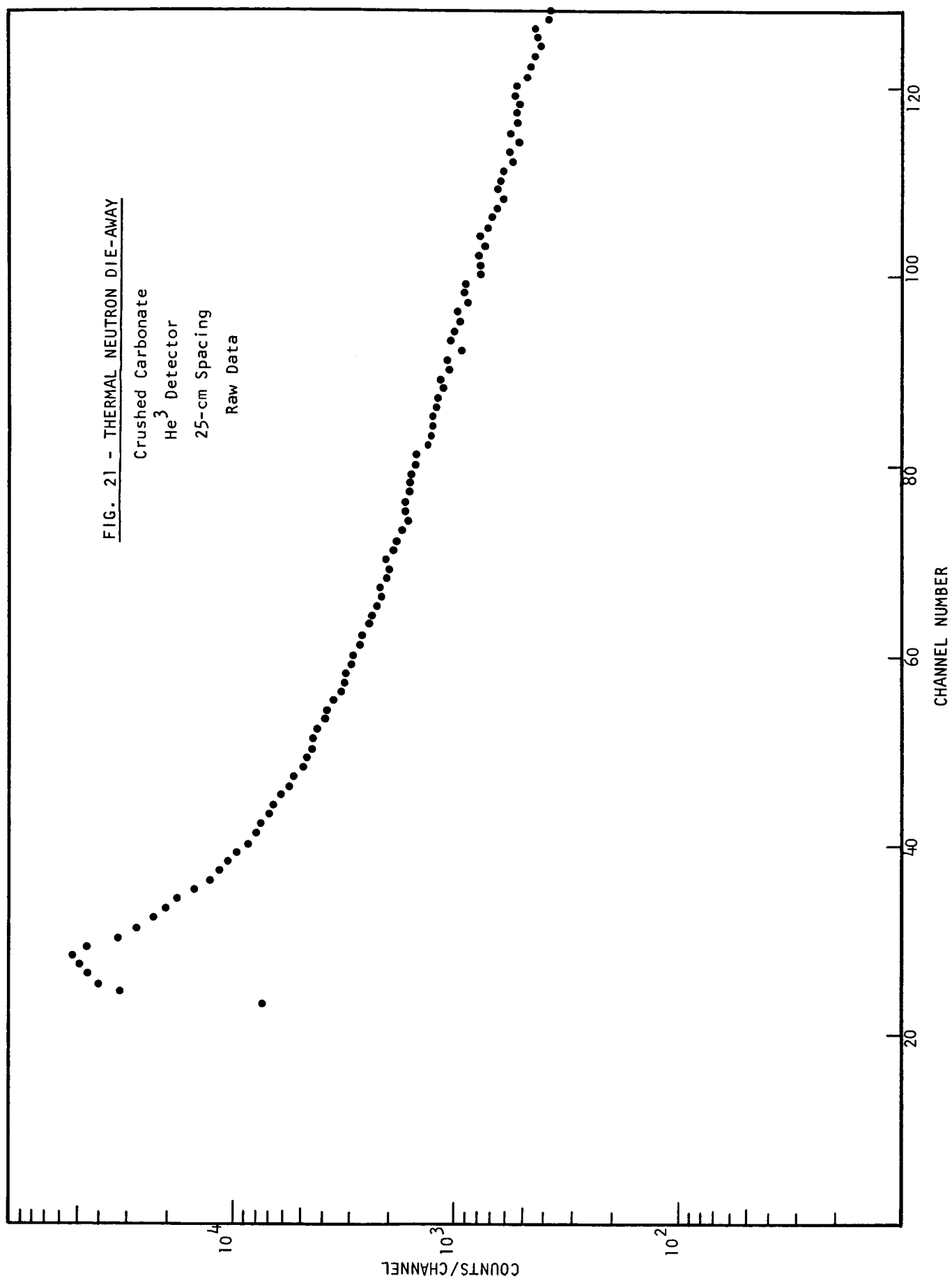
FIG. 21 - THERMAL NEUTRON DIE-AWAY

Crushed Carbonate

He<sup>3</sup> Detector

25-cm Spacing

Raw Data



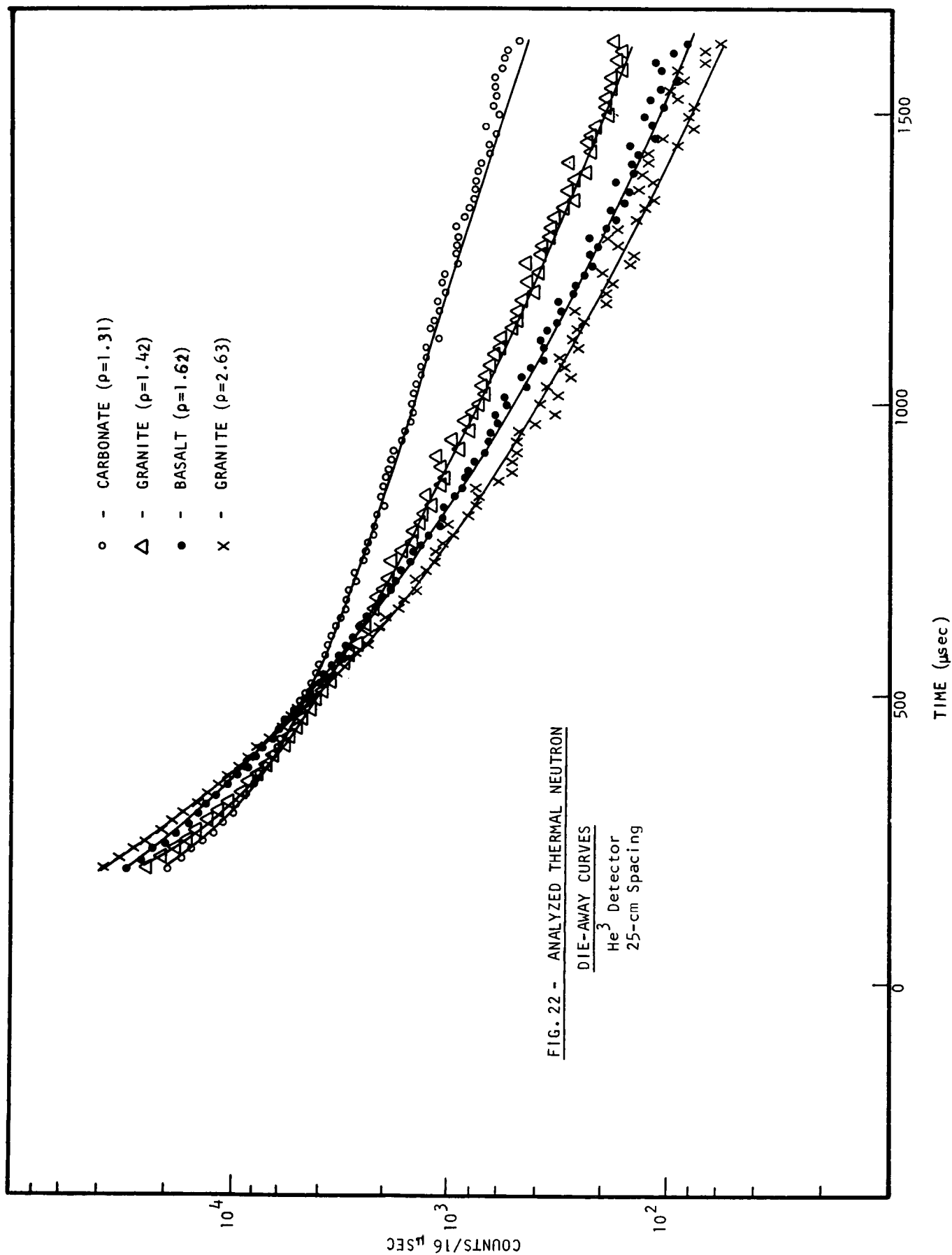
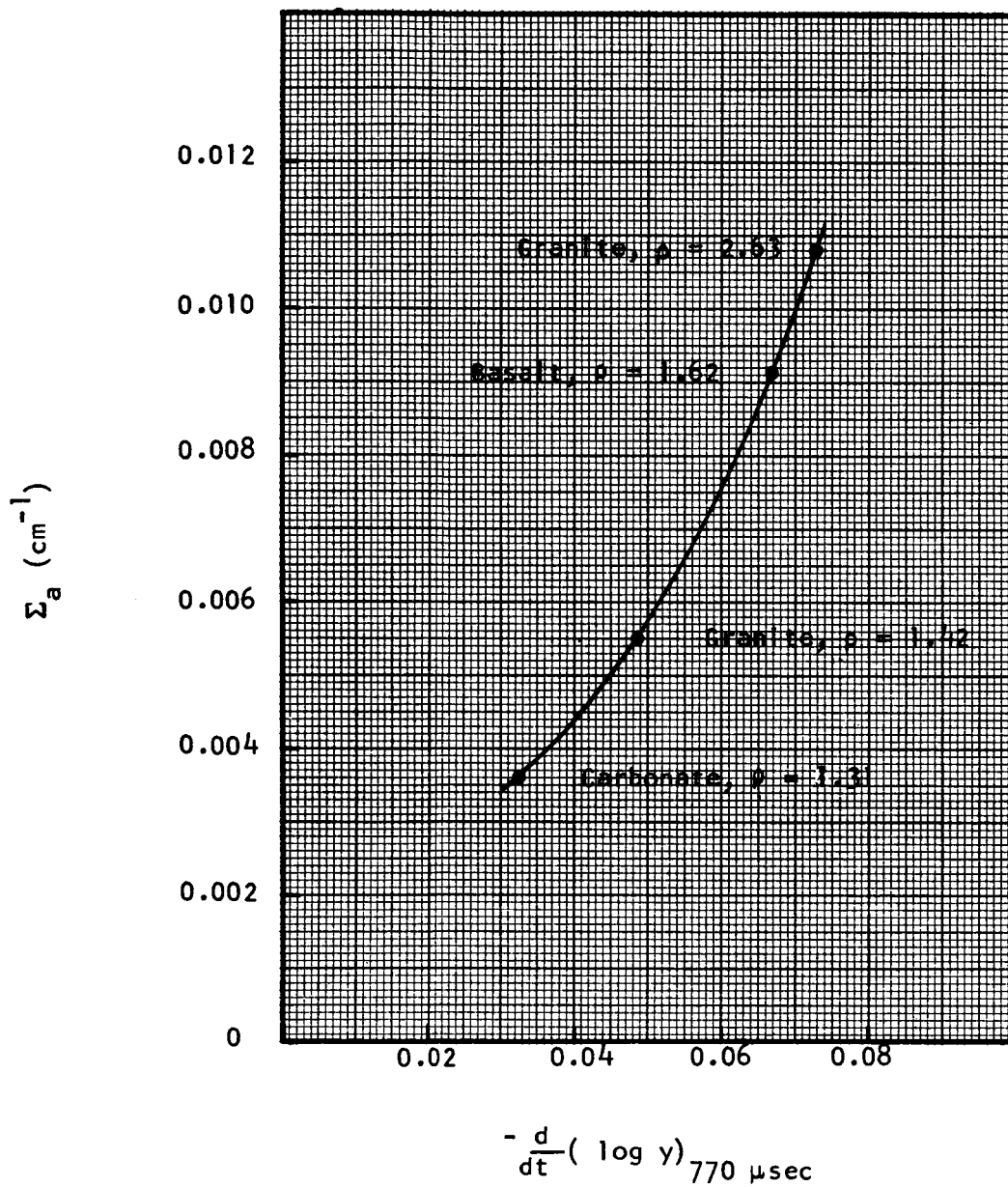


FIG. 23 - CALIBRATION CURVE FOR  
 $\text{He}^3$  DIE-AWAY MEASUREMENTS



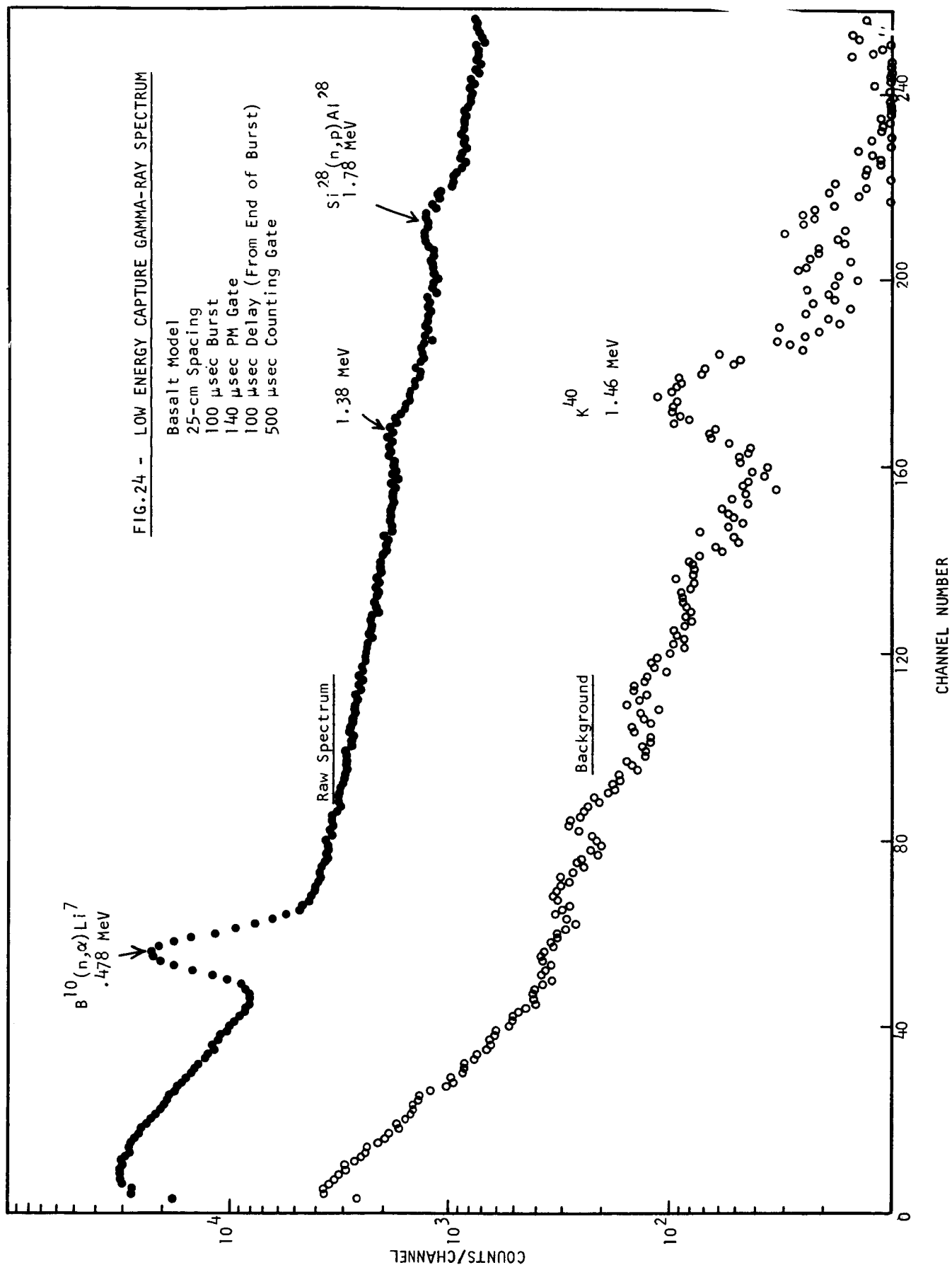


FIG. 25 - GAMMA-RAY DIE-AWAY

Crushed Basalt  
NaI/B<sup>10</sup> Detector  
25-cm Spacing  
Raw Data  
● - 122 Kev Integral Bias  
○ - 300-510 Kev Differential Bias

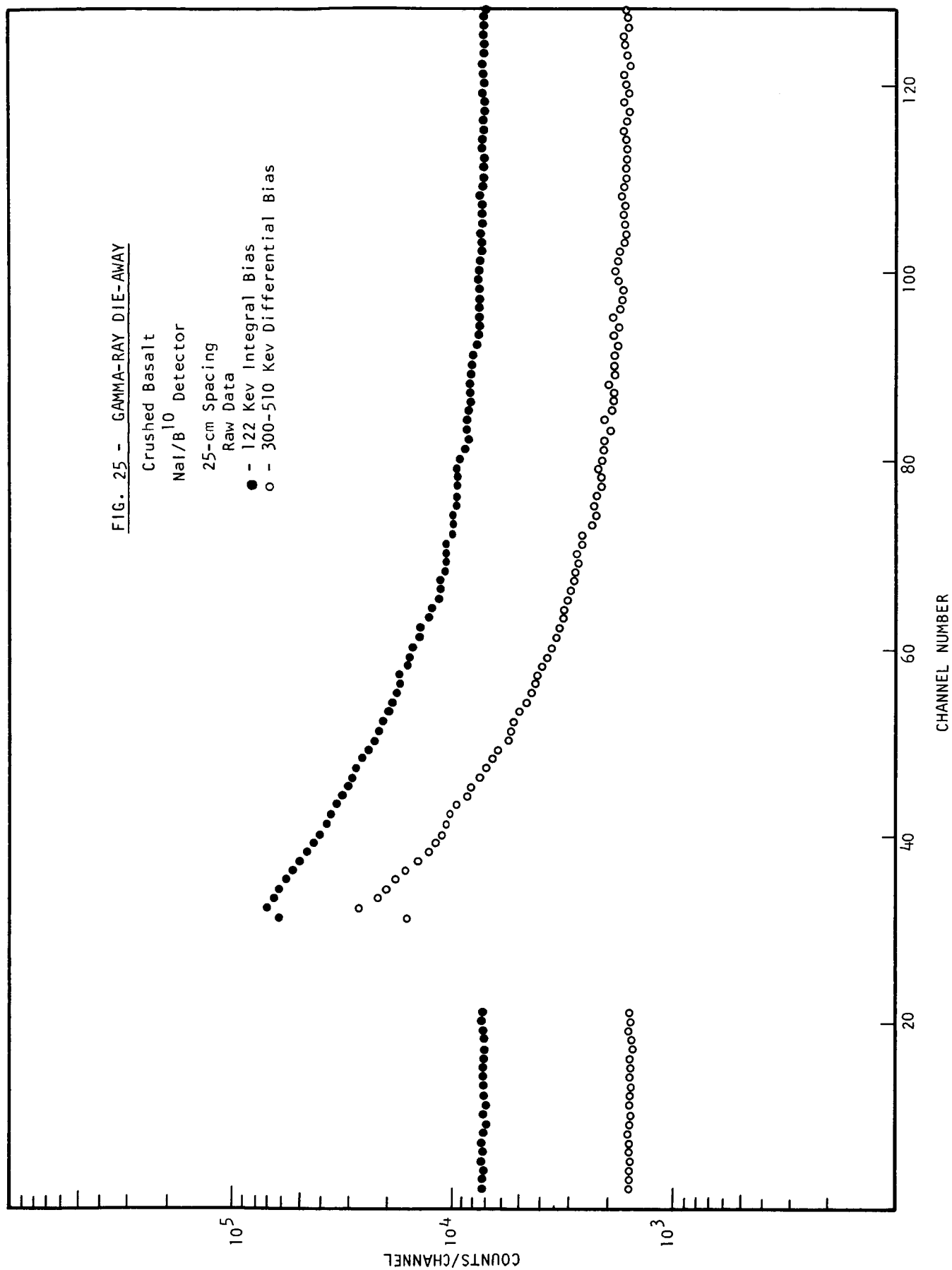


FIG. 26 - GAMMA-RAY DIE-AWAY

Crushed Granite  
NaI/B<sup>10</sup> Detector  
25-cm Spacing  
Raw Data

● - 122 Kev Integral Bias  
○ - 300-510 Kev Differential Bias

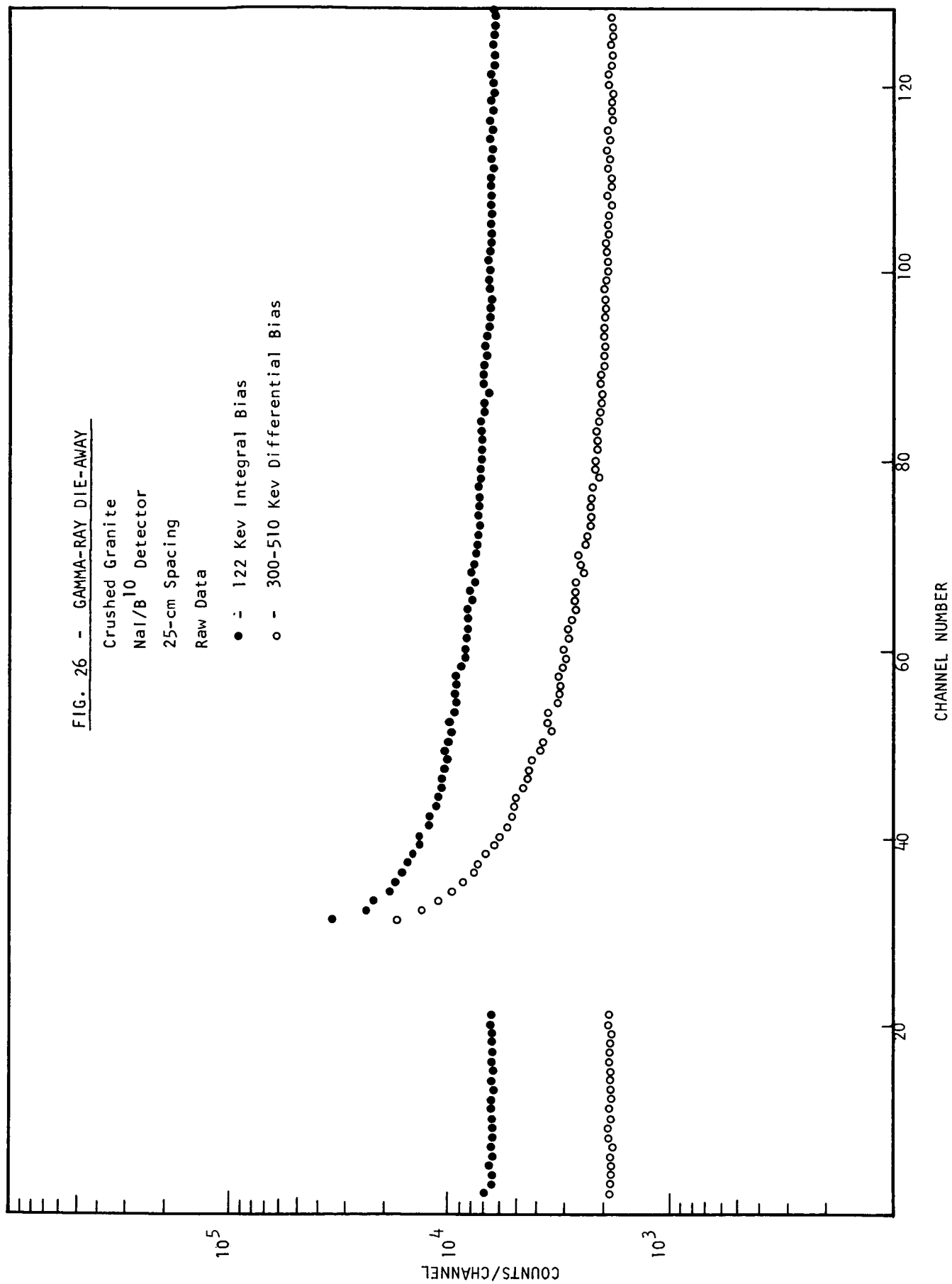


FIG. 27 - GAMMA-RAY DIE-AWAY

Solid Granite  
NaI/B<sup>10</sup> Detector  
25-cm Spacing  
Raw Data  
● - 122 Kev Integral Bias  
○ - 300-510 Kev Differential Bias

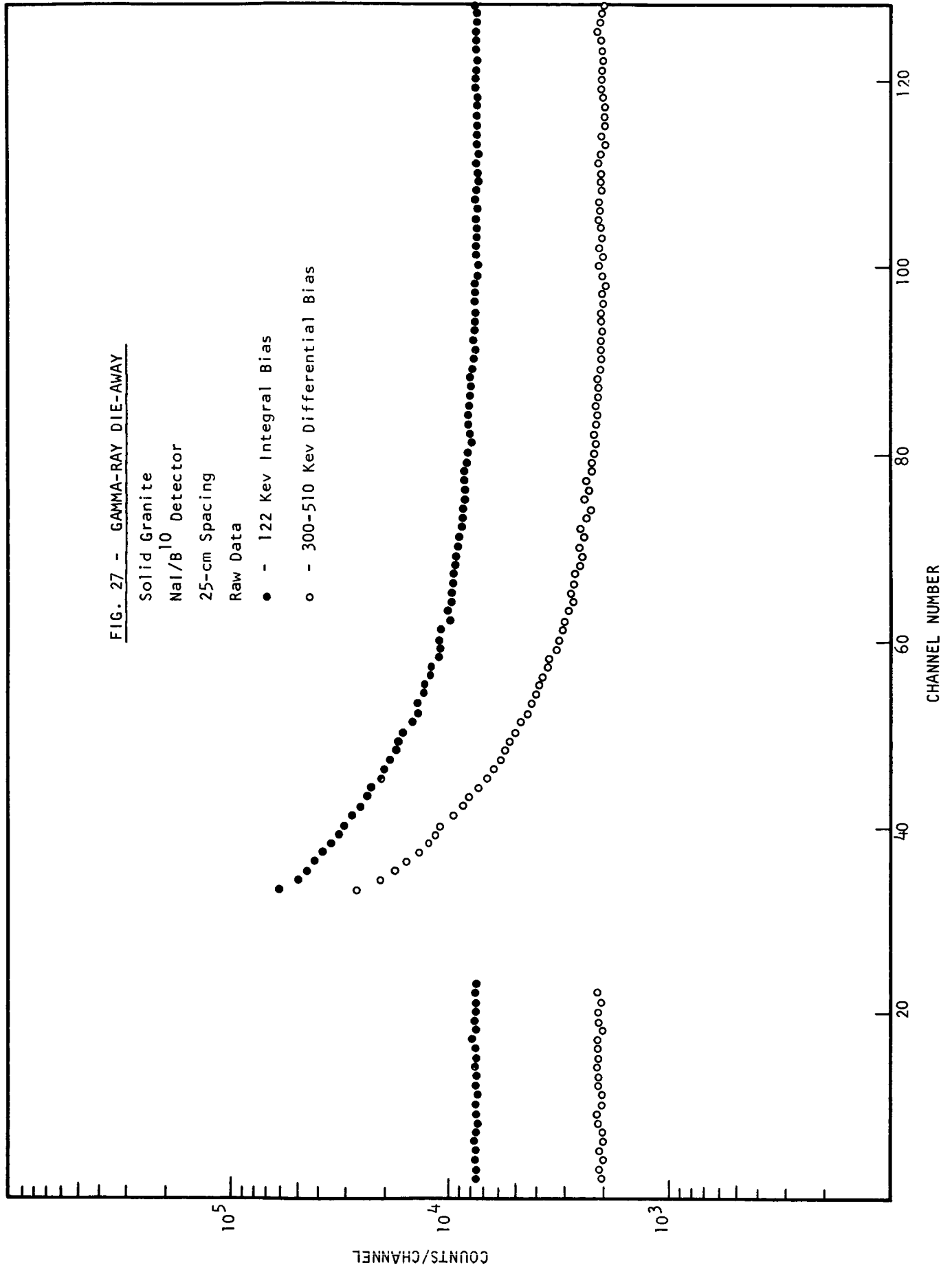




FIG. 28 - GAMMA-RAY DIE-AWAY

Crushed Carbonate

$\text{NaI/B}^{10}$  Detector

25-cm Spacing

Raw Data

• - 122 Kev Integral Bias

o - 300-510 Kev Differential Bias

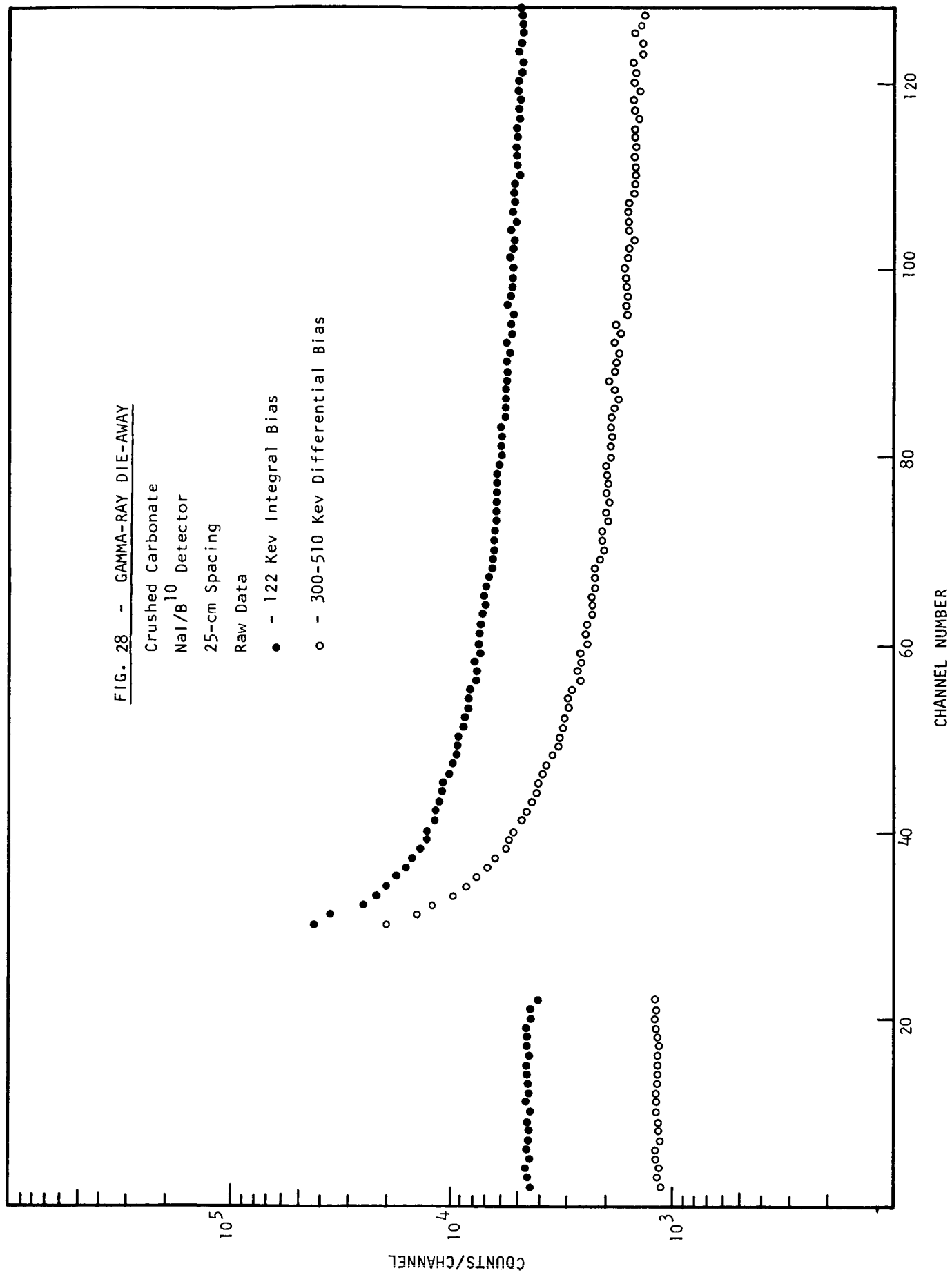


FIG. 29 - GAMMA RAY DIE-AWAY

ON ALL MODELS

NaI/B<sup>10</sup> Detector  
25-cm Spacing  
Corrected Data  
122 Kev Bias

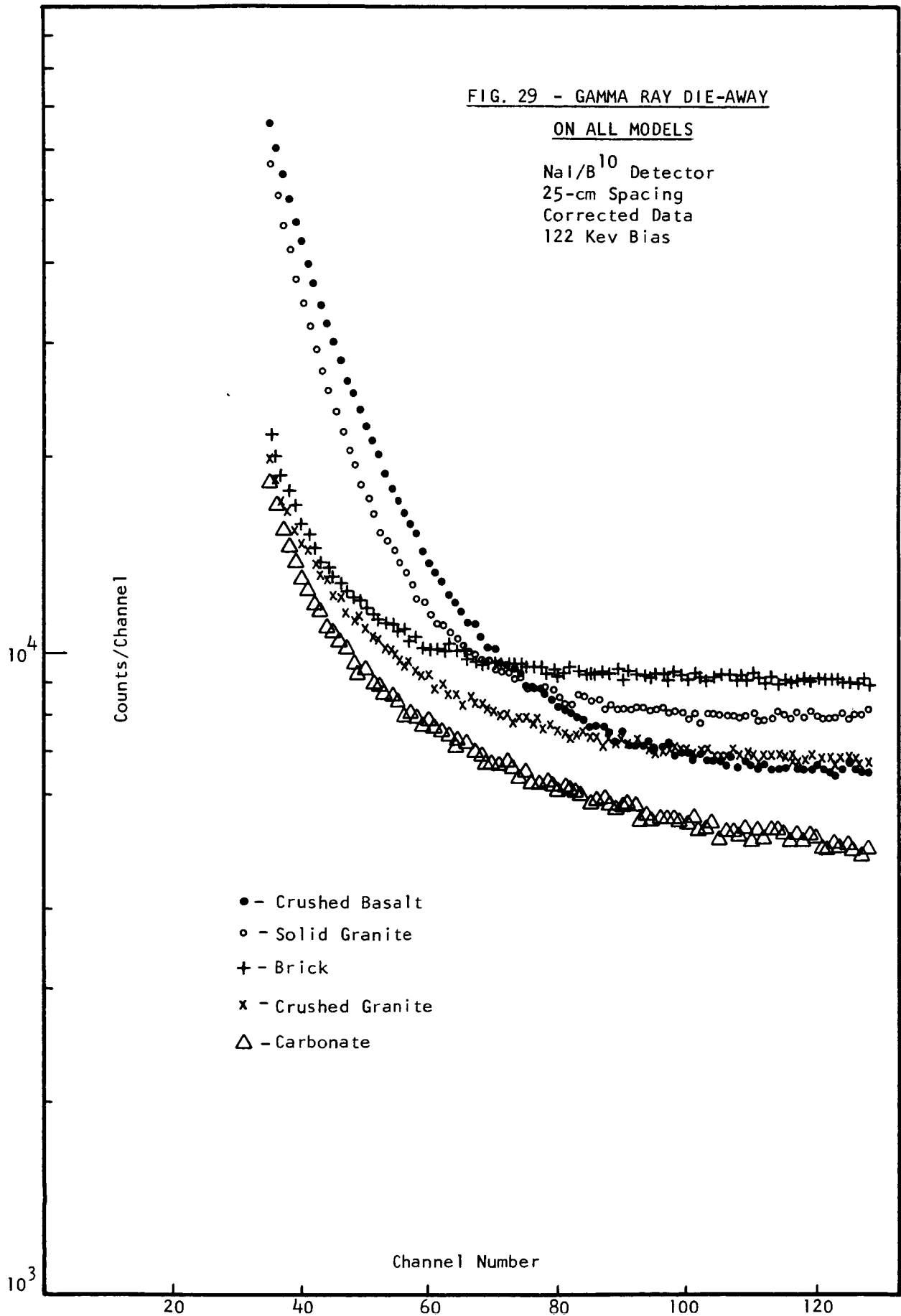


FIG. 30 - EXAMPLES OF ANALYZED GAMMA RAY DIE-AWAY CURVES

WITH BACKGROUND INCLUDED

NaI/B<sup>10</sup> Detector  
122 Kev Bias  
25-cm Spacing

• Granite (p = 2.63)

○ Carbonate (p = 1.31)

Counts/Channel

10<sup>4</sup>

Channel Number

10<sup>3</sup>

20

40

60

80

100

120

FIG. 31 - BACKGROUND CORRECTED GAMMA-RAY DIE-AWAY CURVES

NaI/B<sup>10</sup> Detector  
122 Kev Bias  
25-cm Spacing

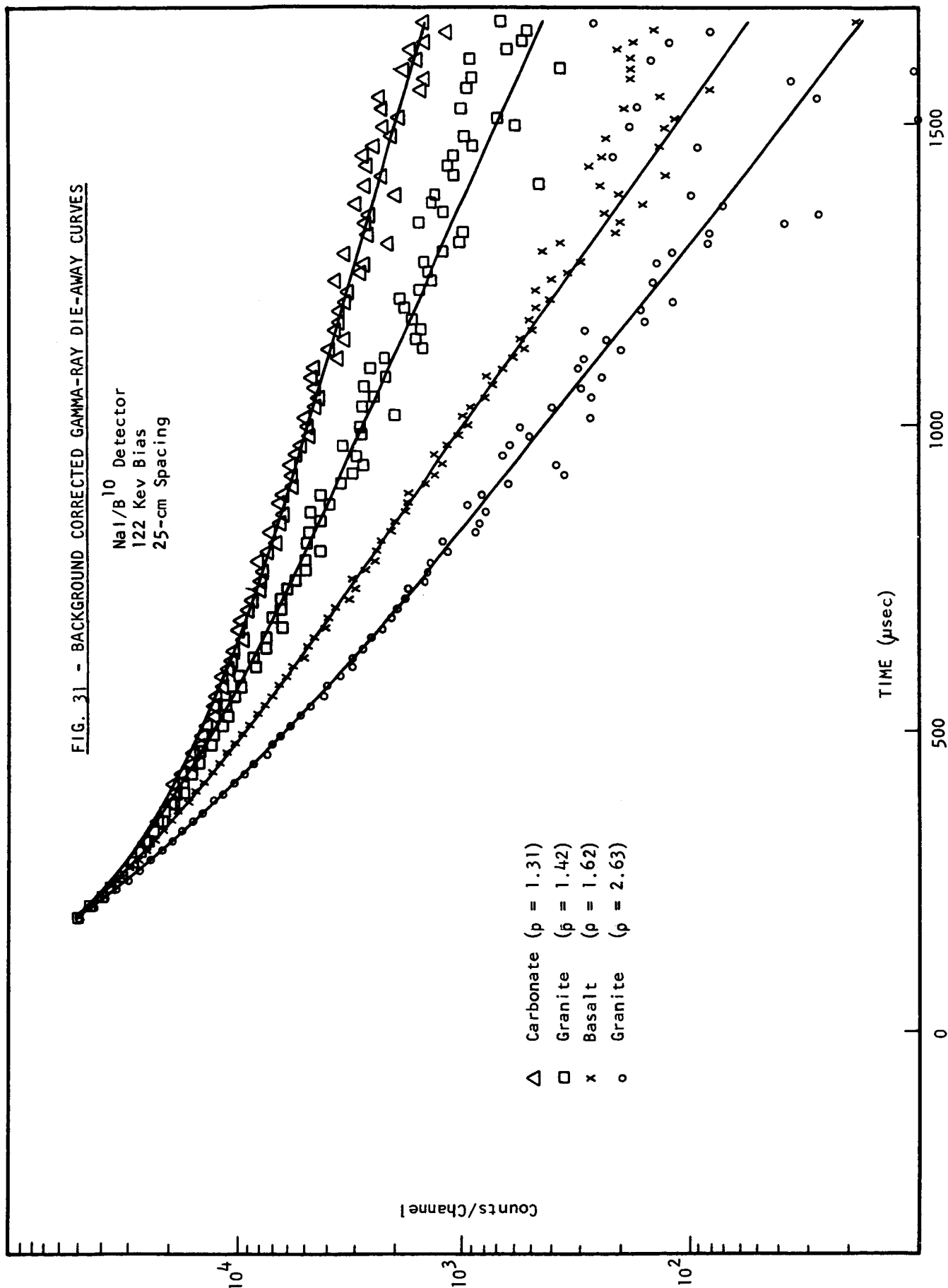


FIG. 32 - CALIBRATION CURVE FOR  
NaI DIE-AWAY MEASUREMENTS  
122-Kev Bias

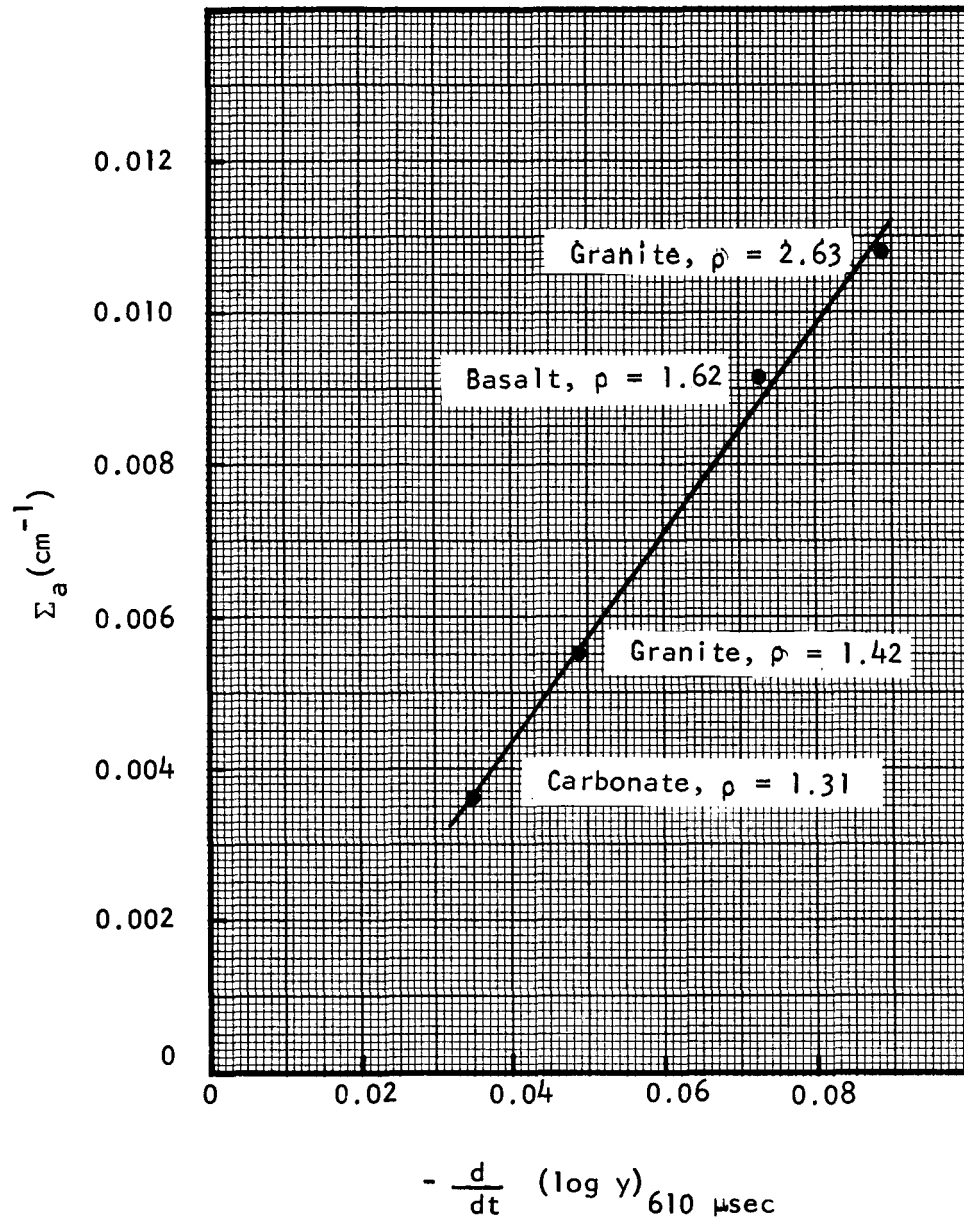


FIG. 33 - EPITHERMAL NEUTRON DIE-AWAY CURVES

He<sup>3</sup>/Cd Detector  
25-cm Spacing  
10-μsec Burst

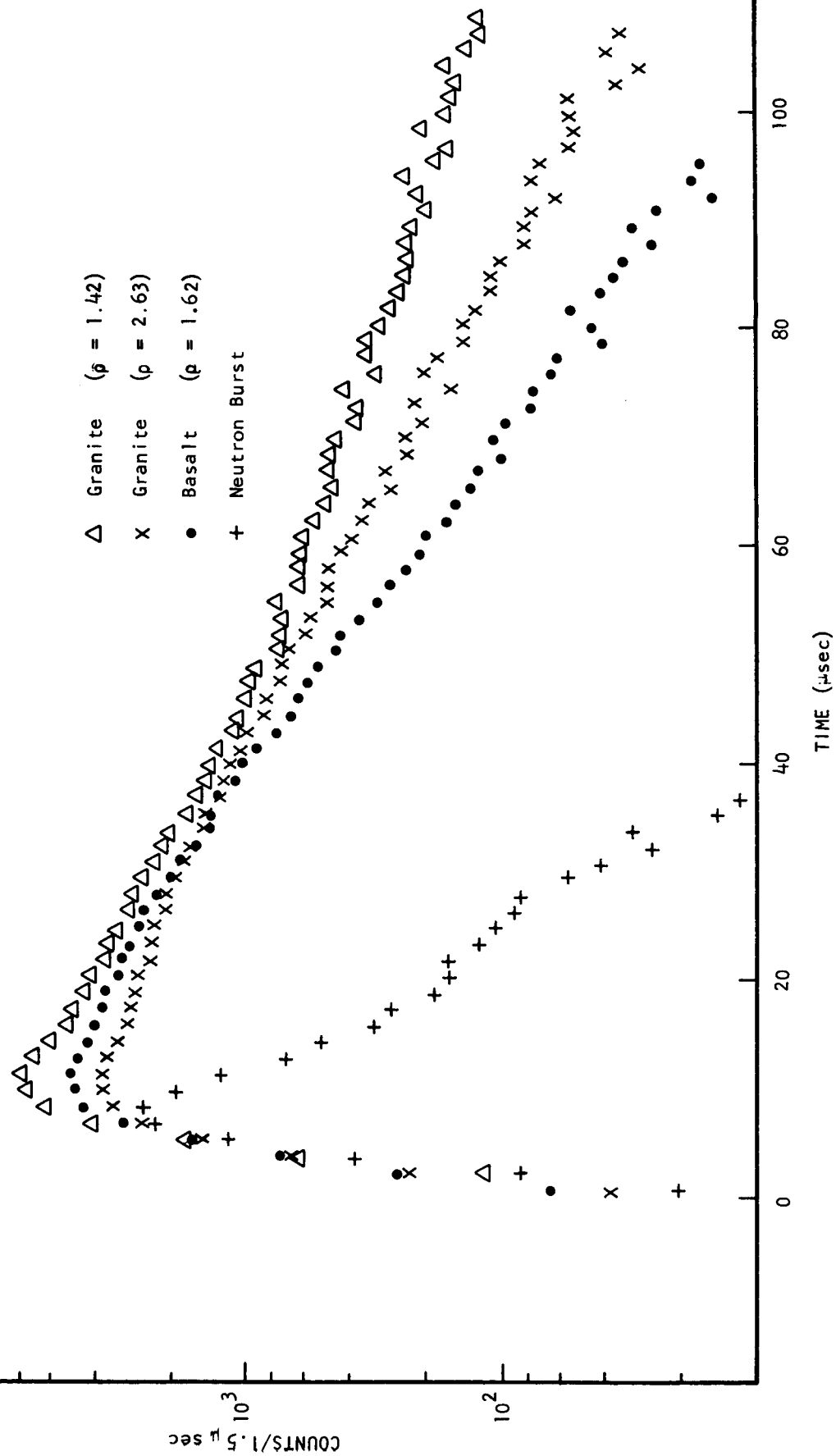


FIG.34 - EPITHERMAL CAPTURE  
GAMMA-RAY DIE-AWAY CURVES

$\text{NaI/B}^{10}$  Detector  
122-Kev Bias  
25-cm Spacing  
0.5  $\mu\text{sec/Channel}$

- Granite ( $\bar{p} = 2.63$ )
- x Granite ( $p = 1.42$ )

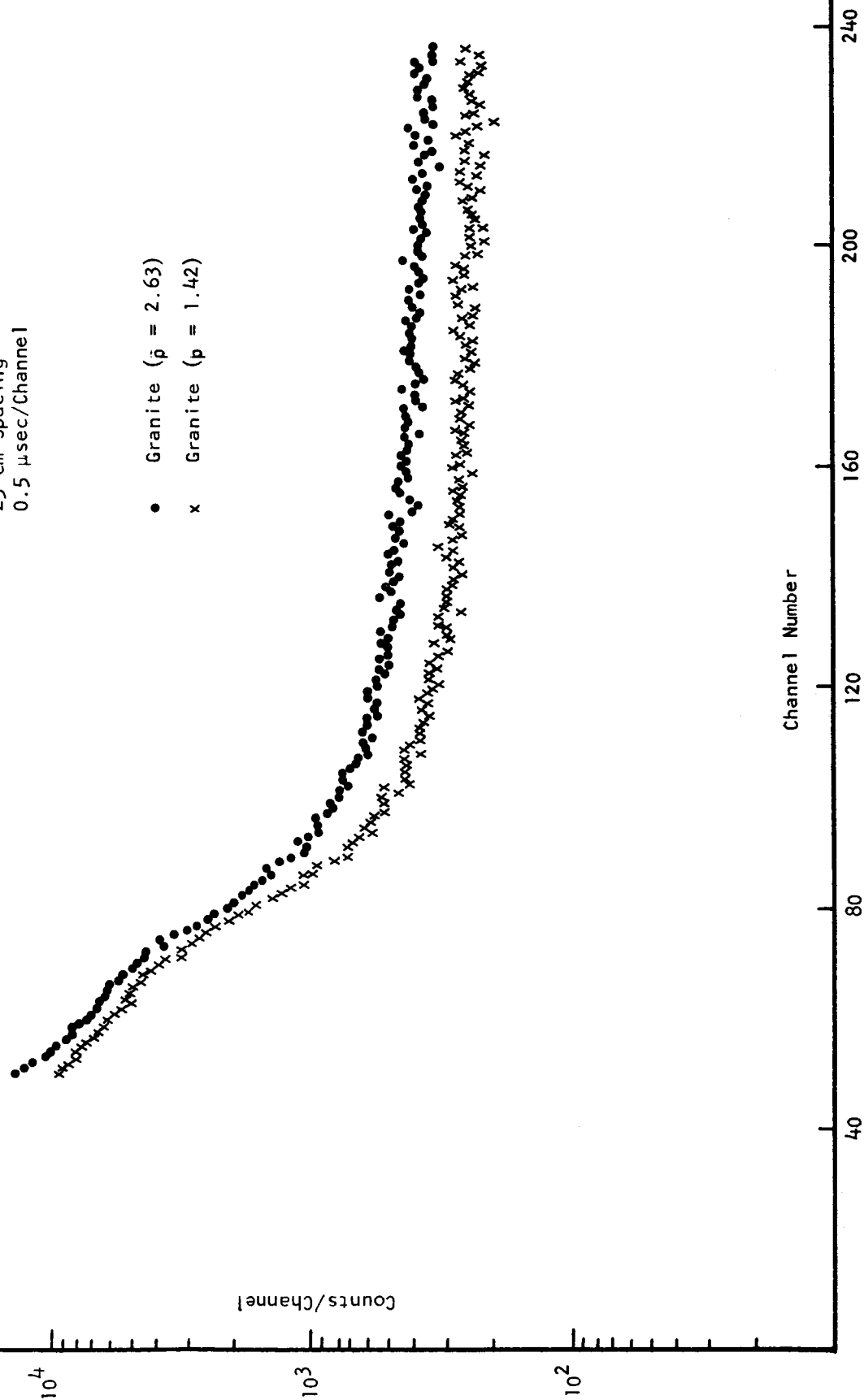


FIG.35 - THERMAL NEUTRON DIE-AWAY SHOWING  
EFFECT OF CONTAINMENT BY WOODEN TRAY

$\text{He}^3$  Detector  
25-cm Spacing

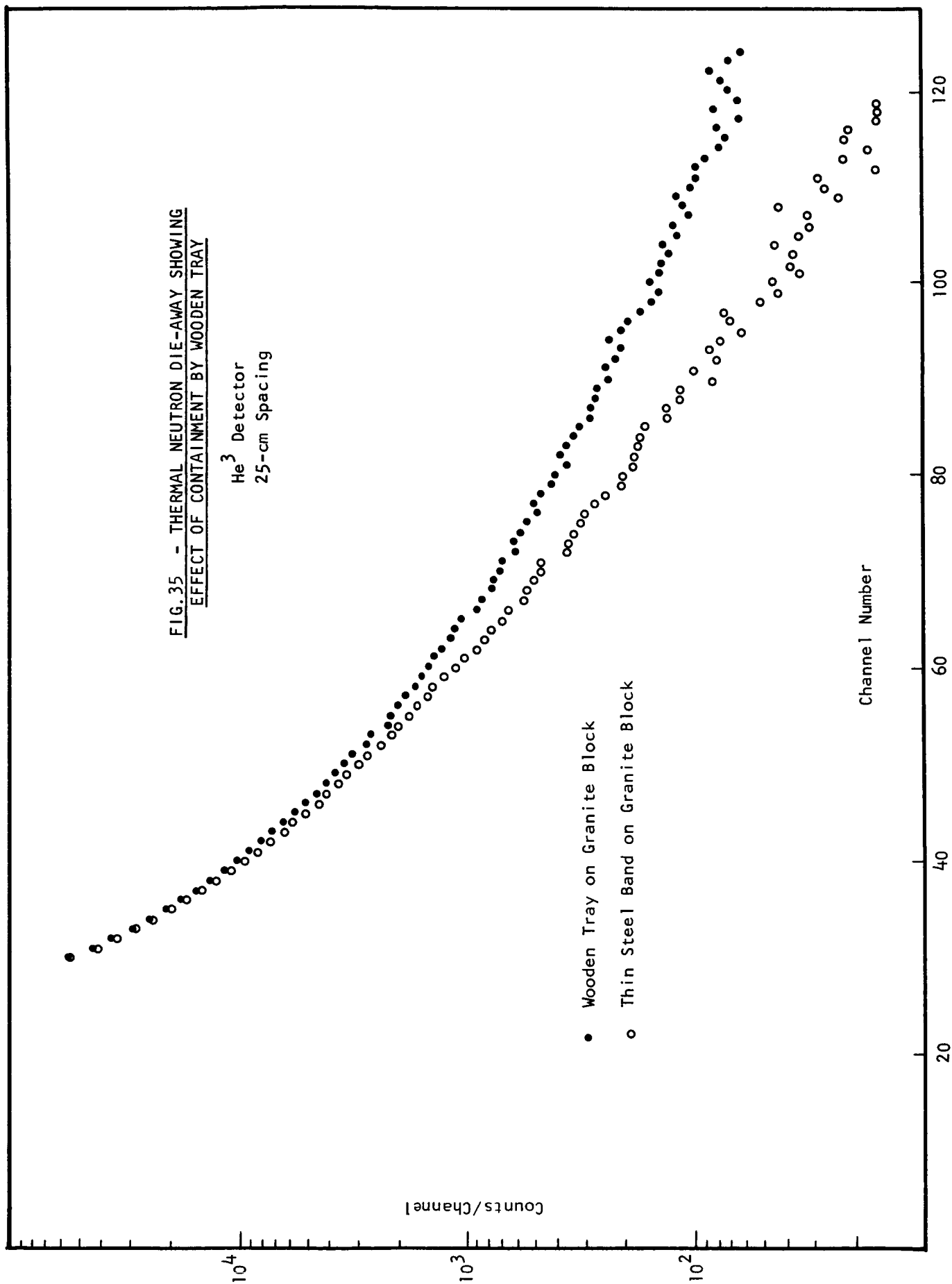
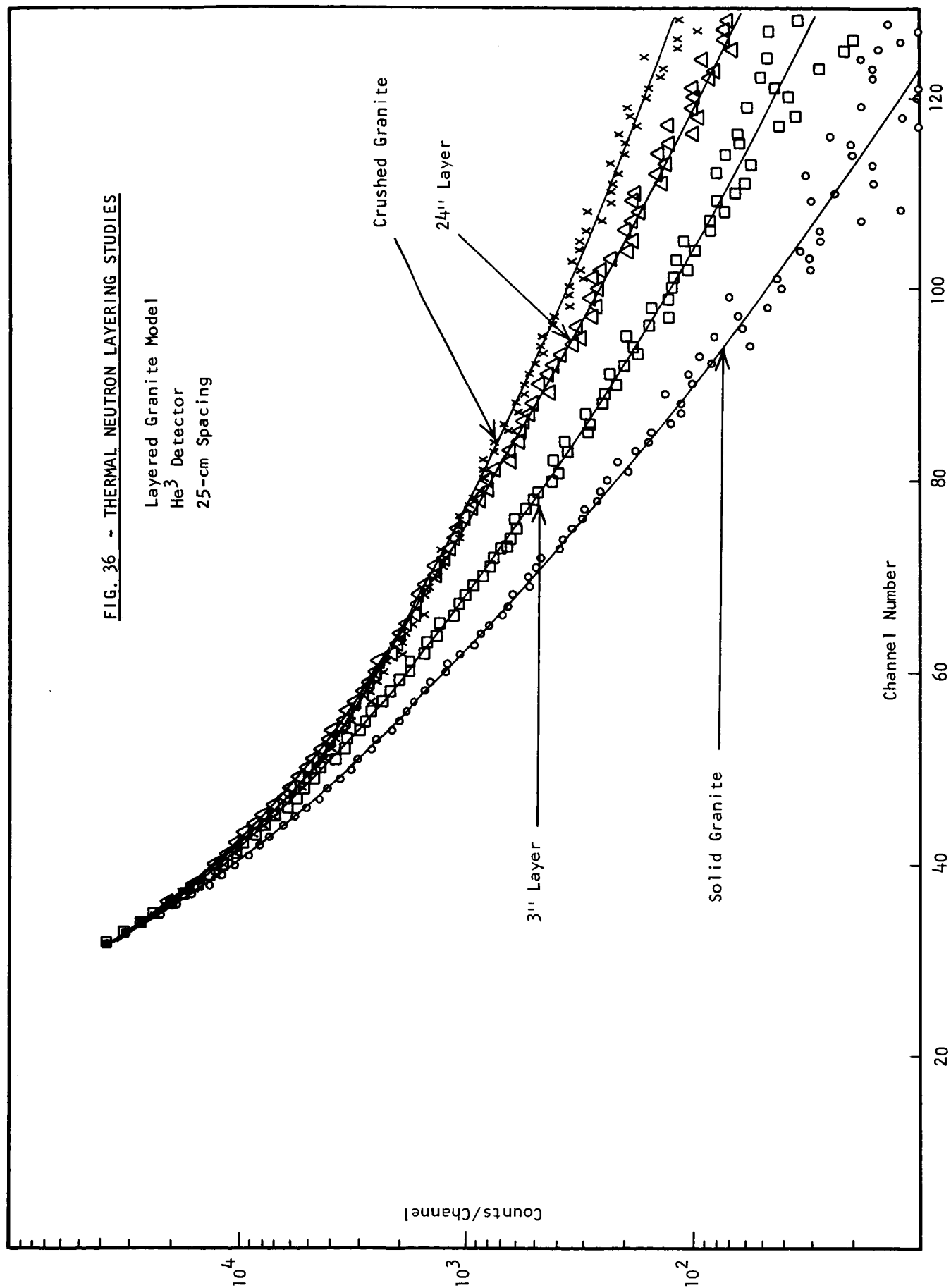




FIG. 36 - THERMAL NEUTRON LAYERING STUDIES

Layered Granite Model  
He<sup>3</sup> Detector  
25-cm Spacing



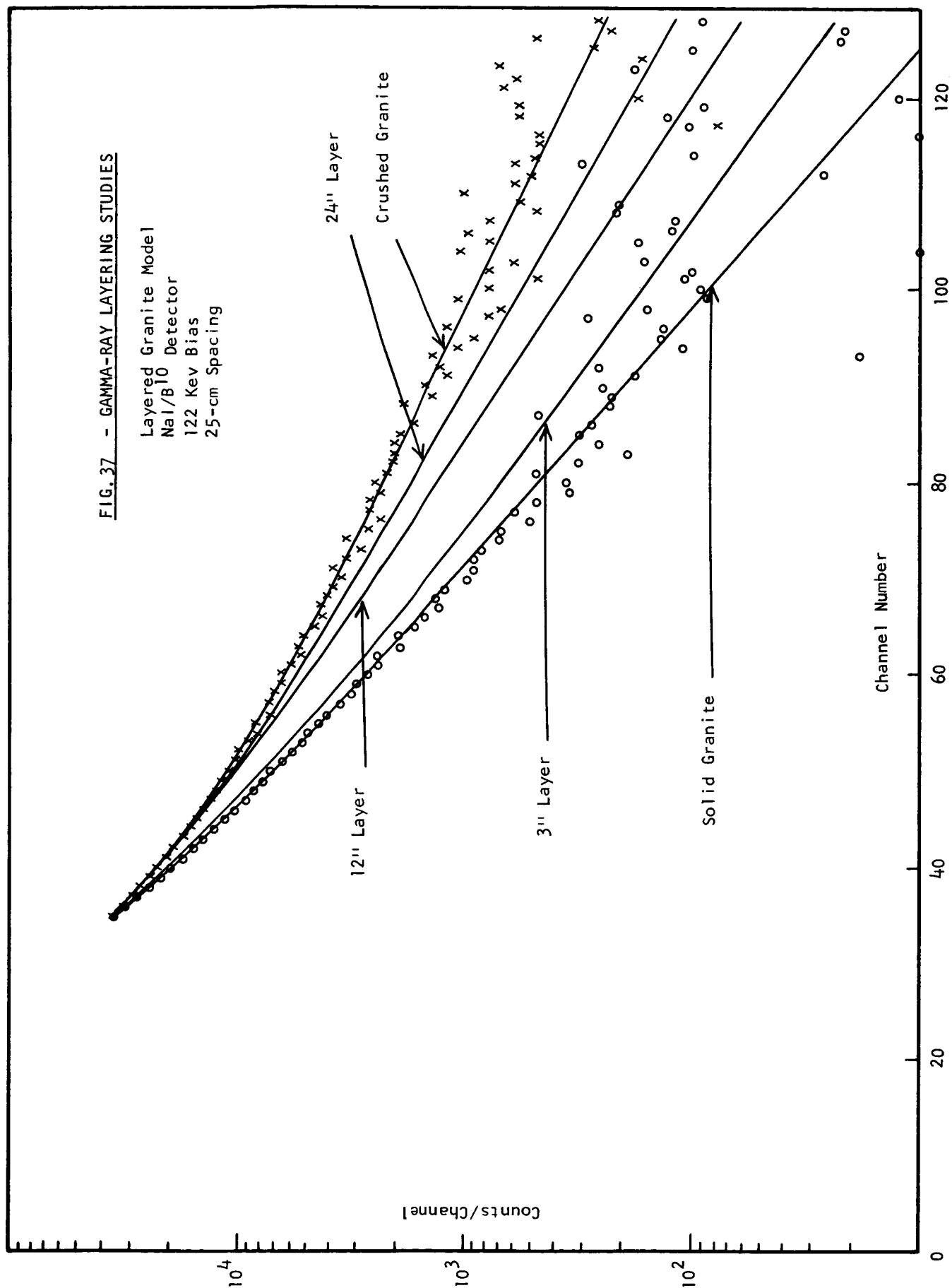


FIG. 38 - EFFECT OF SURFACE IRREGULARITY ON  
THERMAL NEUTRON DIE-AWAY

Crushed Granite  
He<sup>3</sup> Detector  
25-cm Spacing

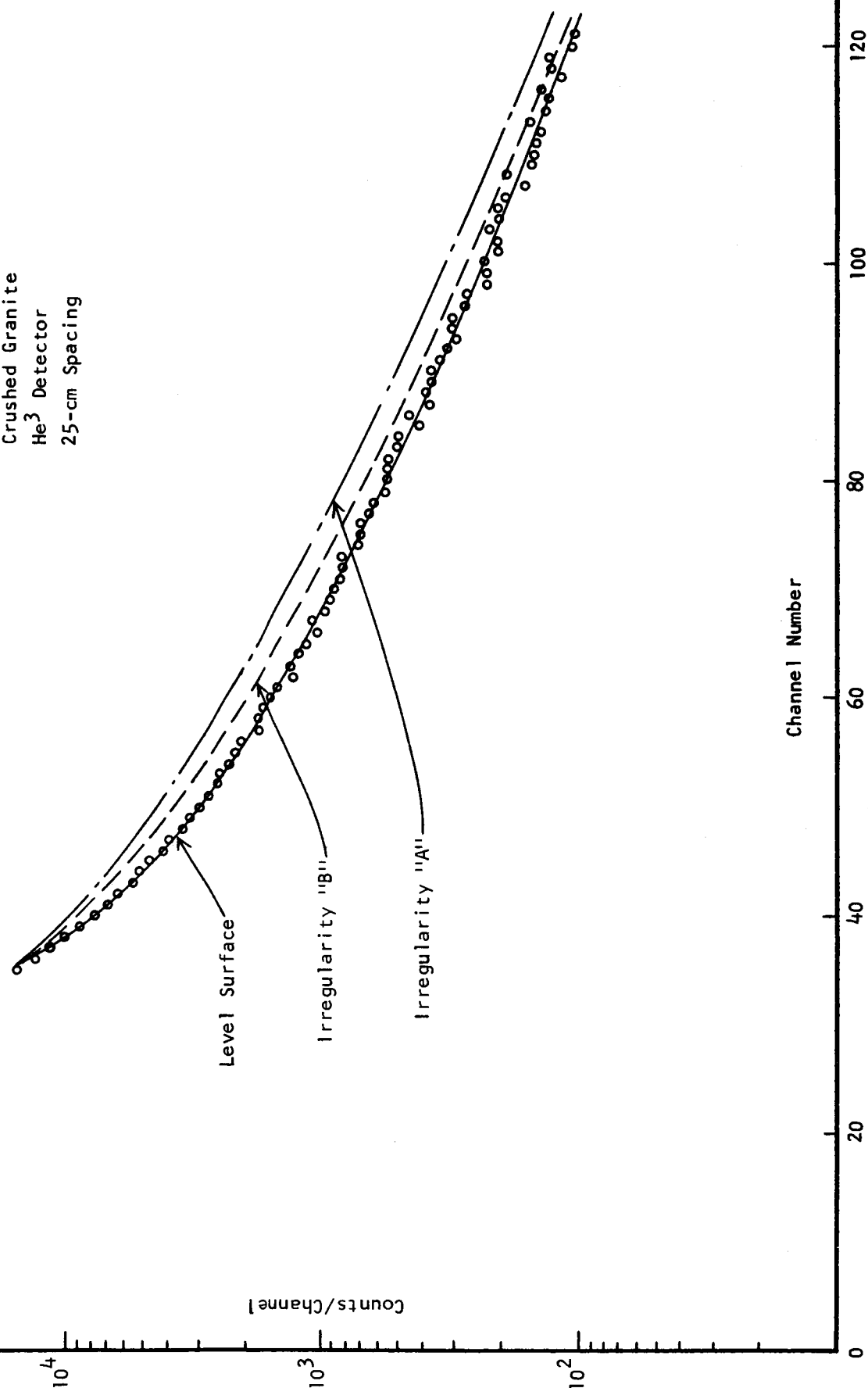
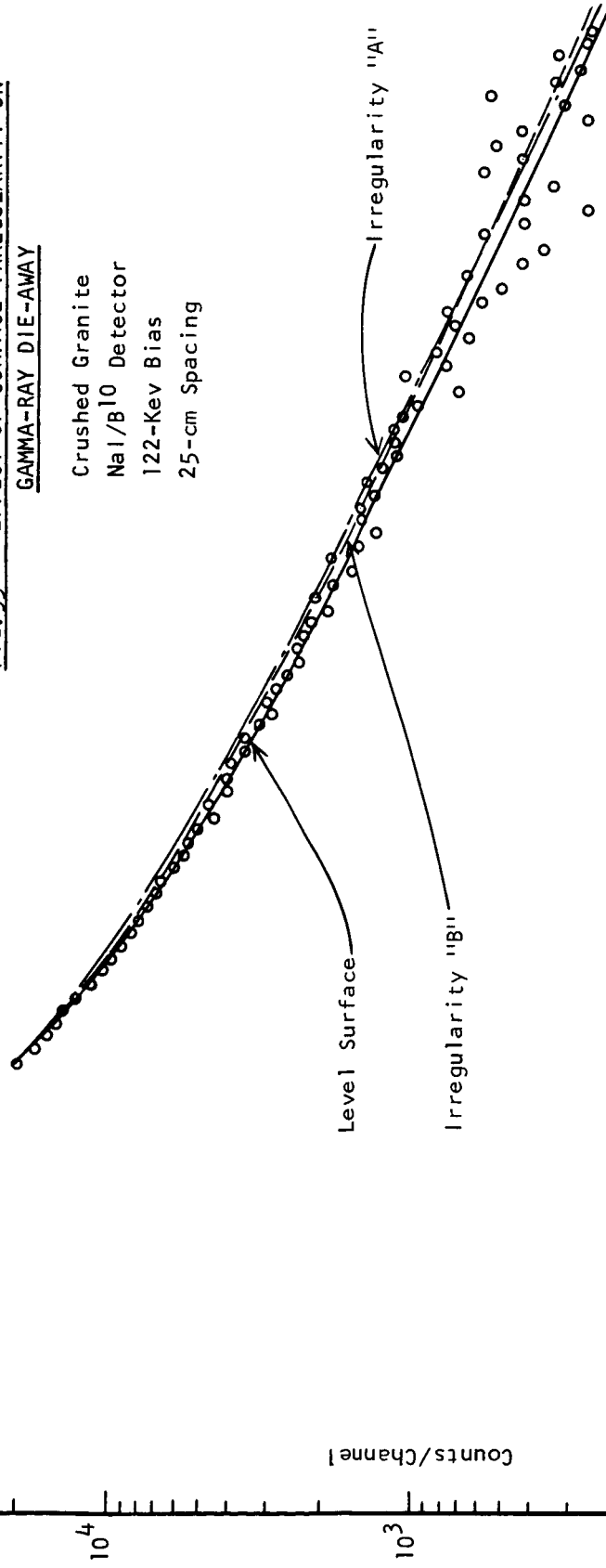
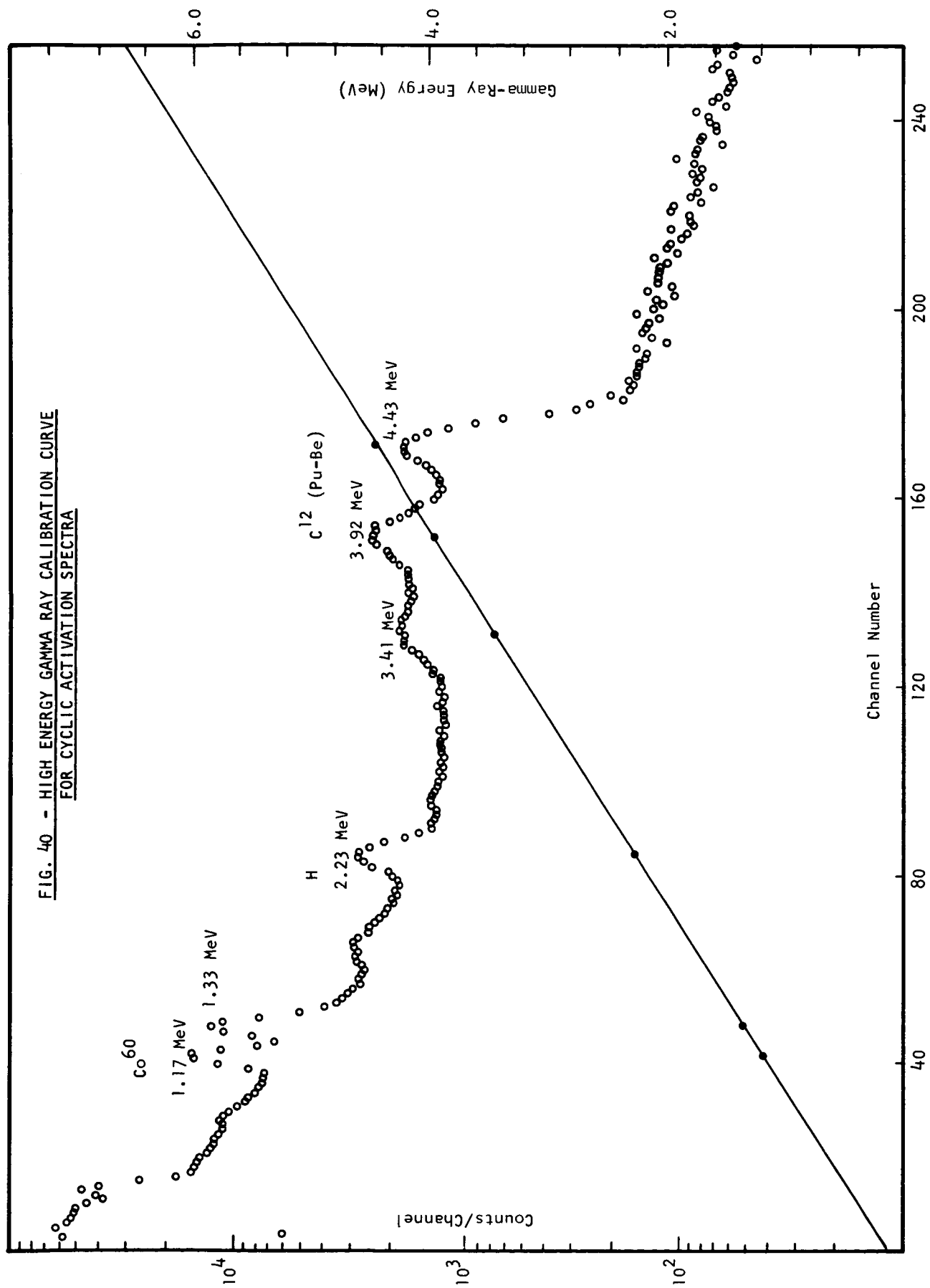


FIG. 39 - EFFECT OF SURFACE IRREGULARITY ON  
GAMMA-RAY DIE-AWAY

Crushed Granite  
NaI/B<sup>10</sup> Detector  
122-Kev Bias  
25-cm Spacing



Channel Number



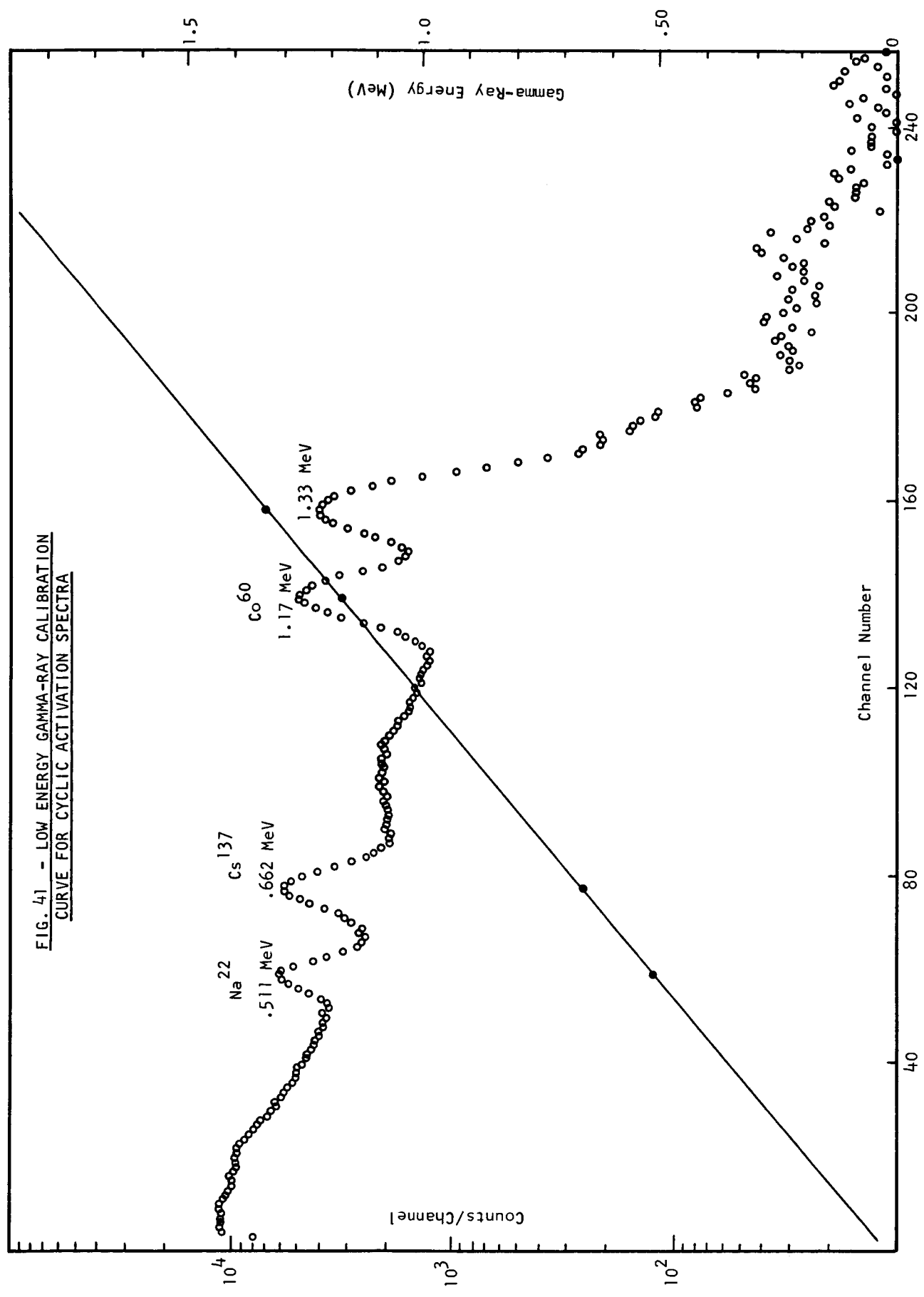


FIG. 41 - LOW ENERGY GAMMA-RAY CALIBRATION  
CURVE FOR CYCLIC ACTIVATION SPECTRA

FIG. 42 - CYCLIC ACTIVATION GAMMA RAYS FROM BASALT

High Energy  
 100  $\mu$ sec Burst  
 140  $\mu$ sec PM Gate  
 2000  $\mu$ sec Delay  
 2500  $\mu$ sec Counting Gate

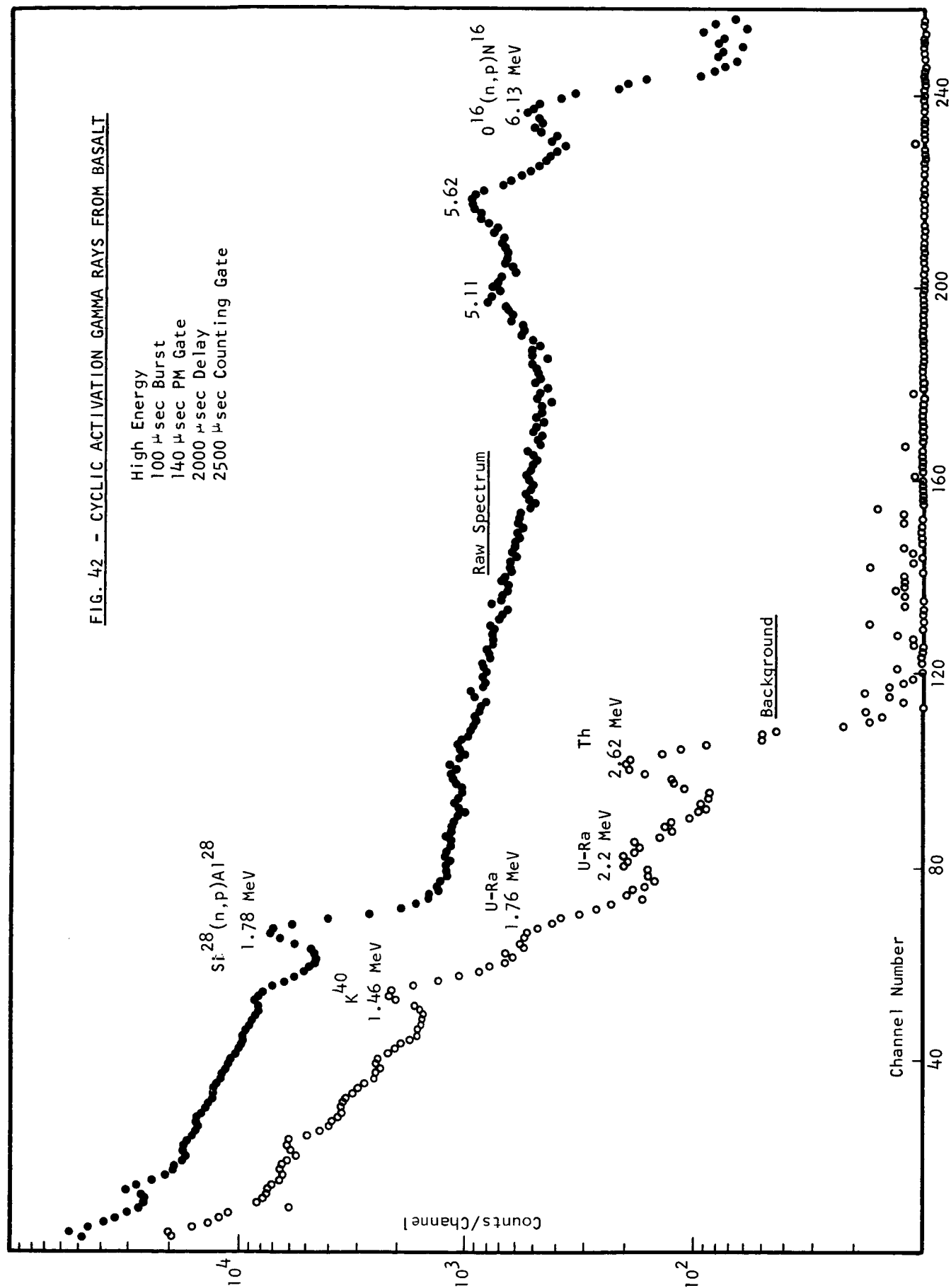


FIG. 43 - CYCLIC ACTIVATION GAMMA RAYS FROM GRANITE

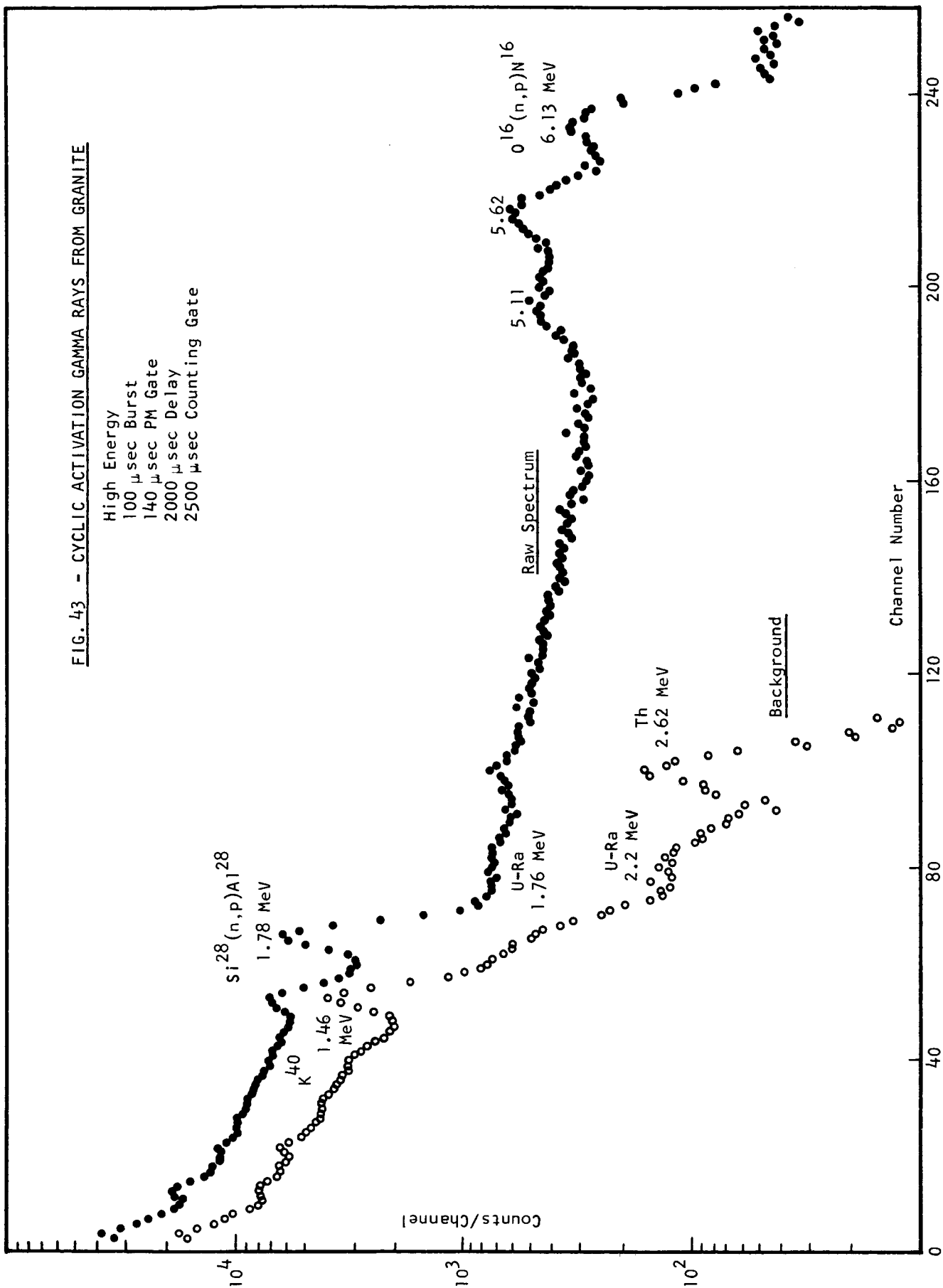




FIG. 44 - CYCLIC ACTIVATION GAMMA RAYS FROM BASALT

Low Energy  
 100  $\mu$ sec Burst  
 140  $\mu$ sec PM Gate  
 2000  $\mu$ sec Delay  
 2500  $\mu$ sec Counting Gate

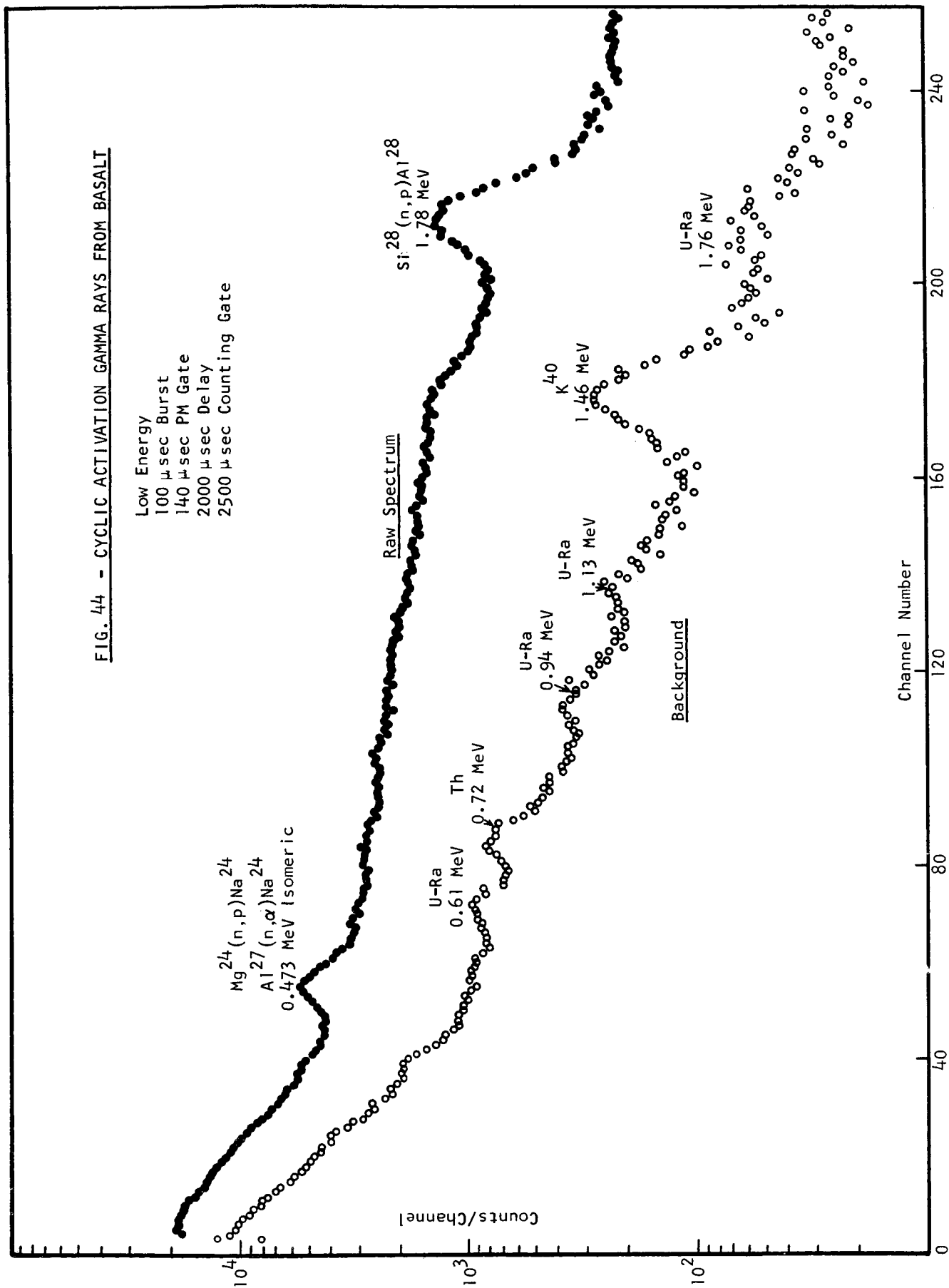


FIG. 45 - CYCLIC ACTIVATION GAMMA RAYS FROM GRANITE

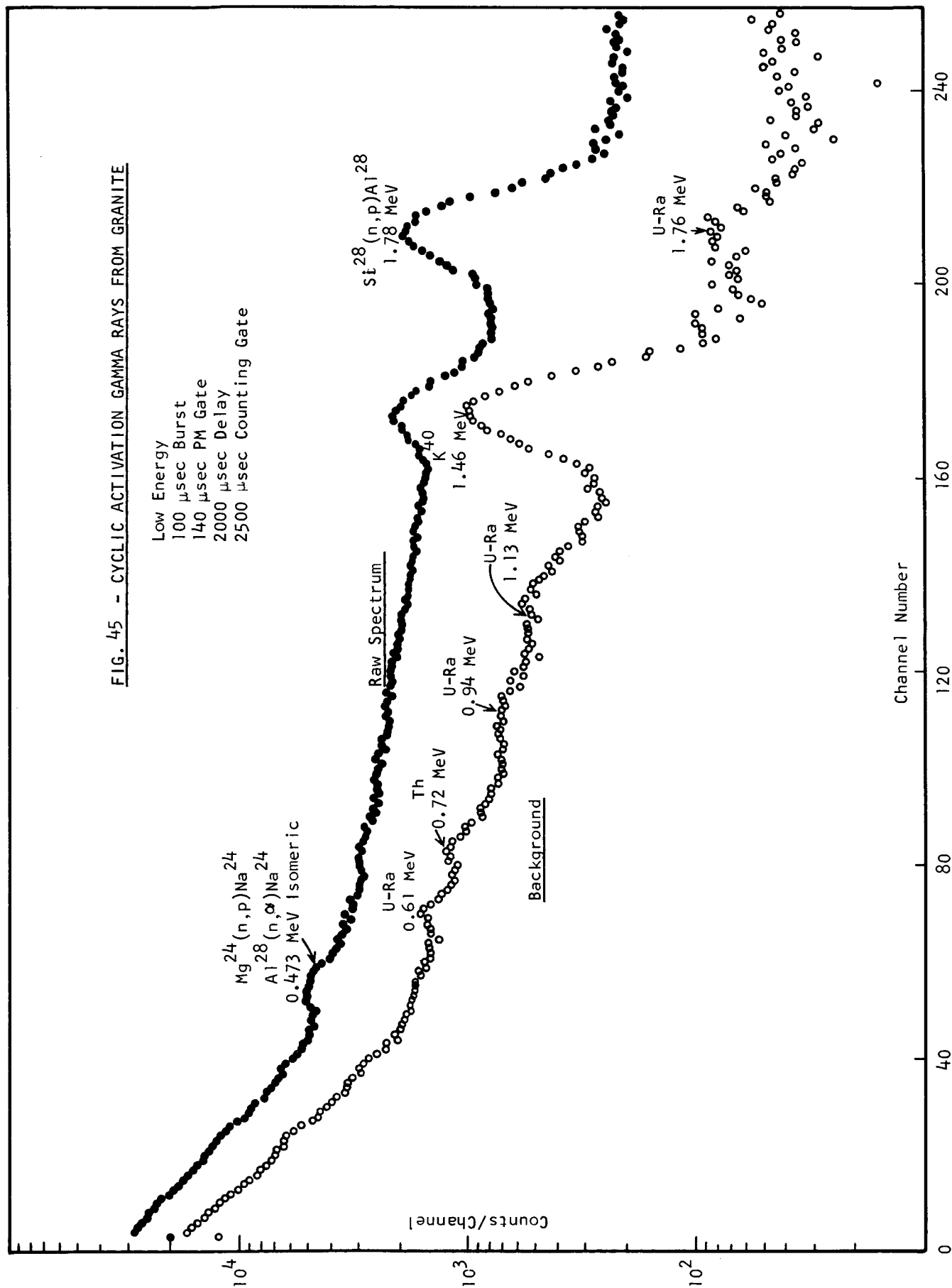


FIG. 46 - BACKGROUND SUBTRACTED CYCLIC  
ACTIVATION GAMMA RAYS

Low Energy  
100  $\mu$  sec Burst  
140  $\mu$  sec PM Gate  
2000  $\mu$  sec Delay  
2500  $\mu$  sec Counting Gate

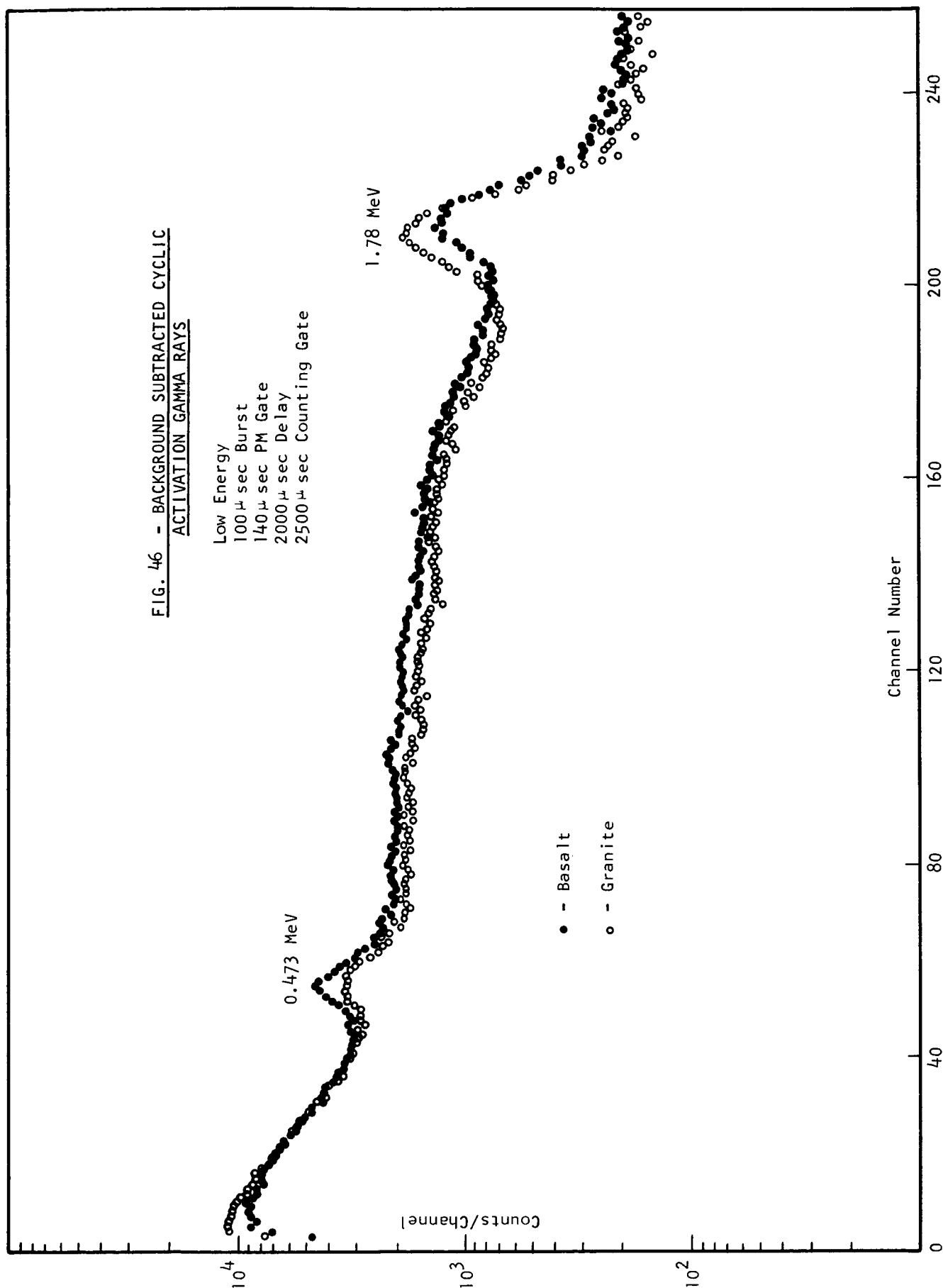


FIG. 47 - ILLUSTRATION OF DISTORTION IN  
UNGATED GAMMA-RAY CURVES

Solid Granite Model  
NaI/B<sup>10</sup> Detector  
122 Kev Bias  
25 cm Spacing  
Raw Data

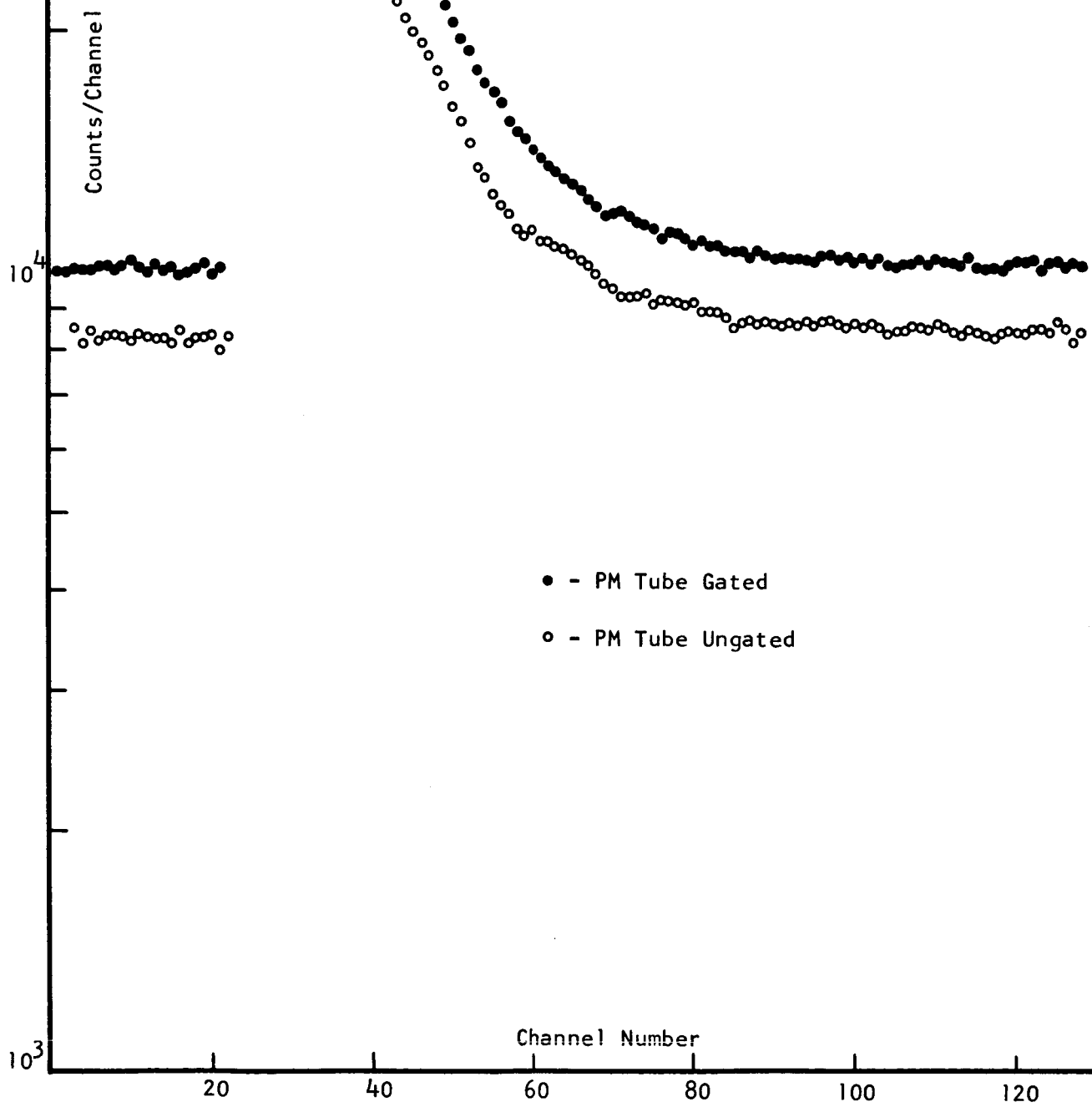
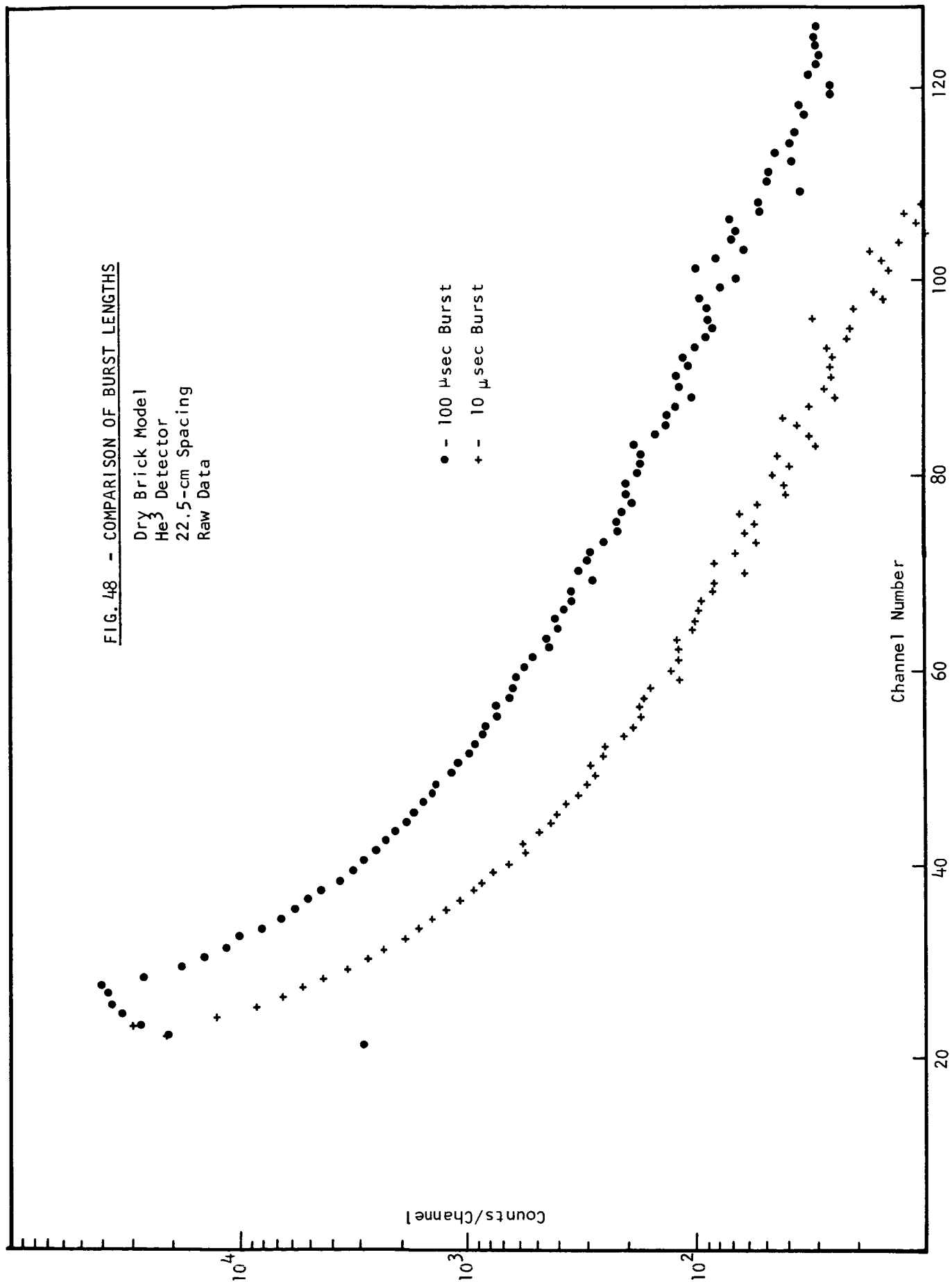


FIG. 48 - COMPARISON OF BURST LENGTHS

Dry Brick Model  
He<sup>3</sup> Detector  
22.5-cm Spacing  
Raw Data

• - 100  $\mu$ sec Burst  
+ - 10  $\mu$ sec Burst



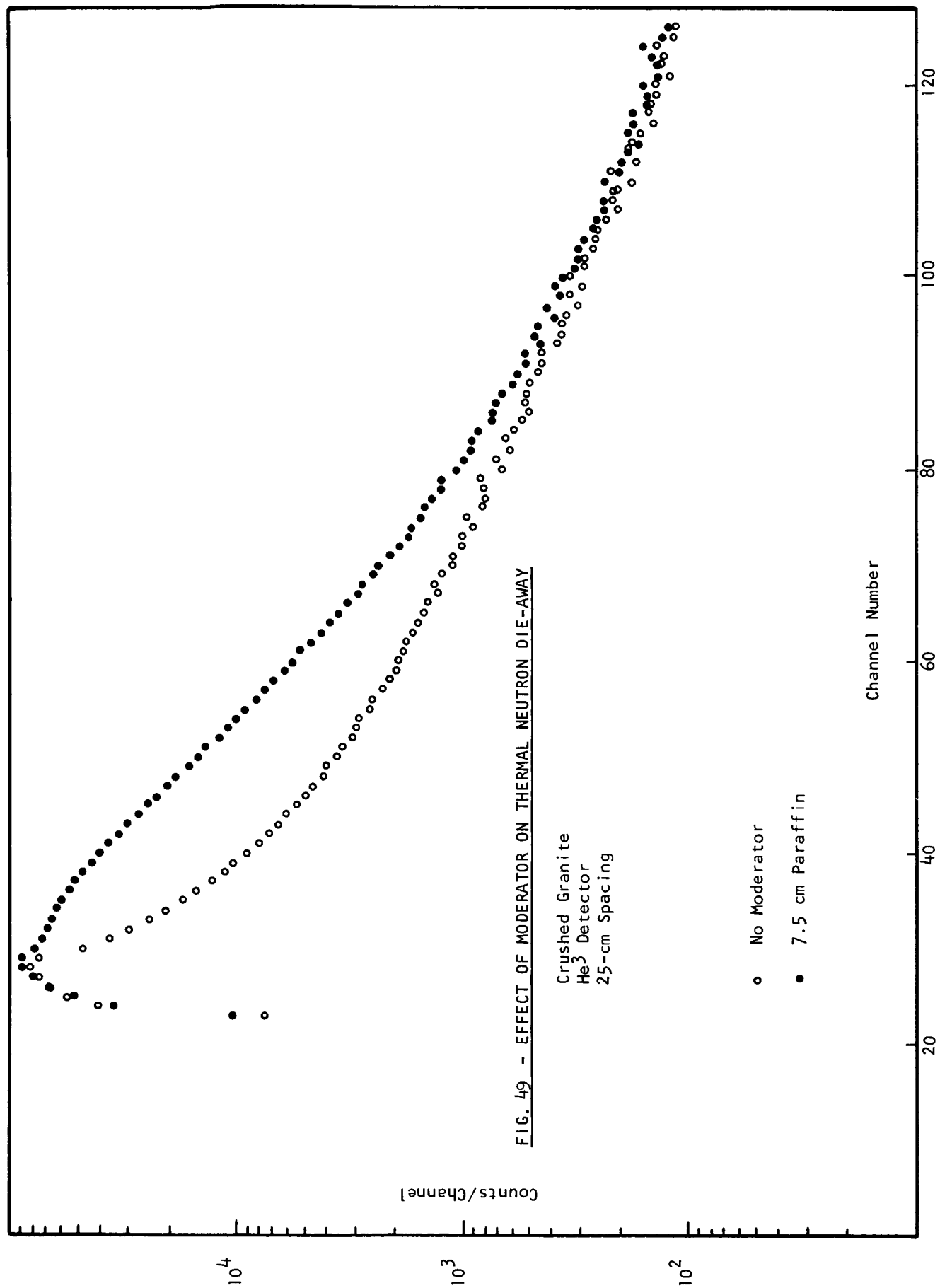


FIG. 49 - EFFECT OF MODERATOR ON THERMAL NEUTRON DIE-AWAY

